Faculdade de Engenharia de Ilha Solteira (FEIS)

Departamento de Física e Química (DFQ)

Programa de Pós-Graduação em Ciência dos Materiais (PPGCM)

Ligações moleculares em semimetais de Dirac-Weyl e grafeno bicamada torcido

William Nobuhiro Mizobata

Doutorado

28 de fevereiro de 2023

Ilha Solteira, São Paulo, Brasil

UNIVERSIDADE ESTADUAL PAULISTA

Faculdade de Engenharia de Ilha Solteira

Departamento de Física e Química

Pós-Graduação em Ciência dos Materiais

Ligações moleculares em semimetais de Dirac-Weyl e grafeno bicamada torcido

William Nobuhiro Mizobata

Orientador: Prof. Dr. Antonio Carlos Ferreira Seridonio

Tese apresentada ao Programa de Pós-Graduação em Ciência dos Materiais, Departamento de Física e Química, Universidade Estadual Paulista – UNESP, Faculdade de Engenharia de Ilha Solteira – SP, como parte dos requisitos para obtenção do título de Doutor em Ciência dos Materiais. Área de concentração: Física da Matéria Condensada.

Ilha Solteira - SP

Fevereiro/2023

FICHA CATALOGRÁFICA
Desenvolvido pelo Serviço Técnico de Biblioteca e Documentação

M685l

Mizobata, William Nobuhiro.
Ligações moleculares em semimetais de Dirac-Weyl e grafeno bicamada torcido / William Nobuhiro Mizobata. -- Ilha Solteira: [s.n.], 2023
112 f. : il.

Tese (doutorado) - Universidade Estadual Paulista. Faculdade de Engenharia de Ilha Solteira. Área de conhecimento: Física da Matéria Condensada, 2023

Orientador: Antonio Carlos Ferreira Seridonio
Inclui bibliografia

1. Semimetal de Dirac-Weyl. 2. Grafeno bicamada torcido. 3. Estado atômico frustrado. 4. Orbitais moleculares.

Raiane da Silva Santos
Supervisora Técnica de Seção
Seção Técnica de Referência, Atendimento ao usuário e Documentação
Diretoria Técnica de Biblioteca e Documentação
CRB/8 - 9999

UNIVERSIDADE ESTADUAL PAULISTA

Câmpus de Ilha Solteira

CERTIFICADO DE APROVAÇÃO

TÍTULO DA TESE: Ligações moleculares em semimetais de Dirac-Weyl e grafeno bicamada torcido

AUTOR: WILLIAM NOBUHIRO MIZOBATA
ORIENTADOR: ANTONIO CARLOS FERREIRA SERIDONIO

Aprovado como parte das exigências para obtenção do Título de Doutor em Ciência dos Materiais, área: Física da Matéria Condensada pela Comissão Examinadora:

ACF Seridonio

Prof. Dr. ANTONIO CARLOS FERREIRA SERIDONIO (Participaçao Presencial)
Departamento de Física e Química / Faculdade de Engenharia de Ilha Solteira - UNESP

Prof. Dr. EUDES BORGES DE ARAUJO (Participaçao Presencial)
Departamento de Física e Química / Faculdade de Engenharia de Ilha Solteira - UNESP

Prof. Dr. FERNANDO ROGERIO DE PAULA (Participaçao Presencial)
Departamento de Física e Química / Faculdade de Engenharia de Ilha Solteira - UNESP

Prof. Dr. LUIS GREGORIO GODOY DE VASCONCELLOS DIAS DA SILVA (Participaçao Virtual)
Departamento de Física de Materiais e Mecânica / Instituto de Física - Universidade de São Paulo

Prof. Dr. JUAREZ LOPES FERREIRA DA SILVA (Participaçao Virtual)
Departamento de Físico-Química / Instituto de Química de São Carlos - Universidade de São Paulo

Ilha Solteira, 28 de fevereiro de 2023

*Aos meus pais, **Sônia** e **Rubens**, que sempre me apoiaram.*

*À minha filha **Helena**, pelo amor e carinho que me motiva todos os dias.*

*À **Thais Tachibana**, por mudar minha vida para melhor.*

It's my life

It's now or never

But I ain't gonna live forever

I just want to live while I'm alive

Essa é a minha vida

É agora ou nunca

Mas eu não vou viver para sempre

Eu só quero viver enquanto estou vivo

[It's my life - Bon Jovi (2000)]

AGRADECIMENTOS

Deixo aqui meus agradecimentos a todos que fizeram parte da jornada para o desenvolvimento desta pesquisa, especialmente para:

• Agradeço ao meu orientador Professor Antonio Carlos Ferreira Seridonio.

• À minha mãe Sônia, meu pai Rubens e minhas irmãs Vanessa e Andressa por acreditarem em mim.

• À minha filha Helena, motivo e razão de buscar ser alguém melhor.

• Ao meu amigo José Eduardo Cardozo Sanches (Theta Points), que considero meu melhor amigo, que sempre me apoiou e ajudou em toda minha trajetória acadêmica. Tenho uma enorme dívida com ele e espero retribuir um dia como gratidão por tudo o que ele fez. Com certeza esta Tese não teria sido concluída sem ele.

• Aos meus amigos e colegas de trabalho, Luciano e Yuri por transformarem o doutorado em uma experiência única e agradável. Também aos meus colegas Luana e Willian pelo apoio durante o doutorado.

• Aos meus amigos Irmãozinho Hirai, Acerola e Gaybriel Hirai por alegrarem minha vida.

• Um agradecimento especial às minhas amigas Mayanna e Carla que contribuíram para moldar, formar e transformar os meus valores para me tornar a pessoa que sou hoje. É impossível expressar a minha completa admiração por essas mulheres, sendo assim, apenas direi "Amo vocês!".

• Também, às minhas amigas Kawana e Maria com quem tive o prazer de conhecer e aprender mais sobre a vida.

• À Thais Cristina Namie Tachibana por me motivar e dar um propósito para seguir minha vida e buscar meus sonhos.

• O presente trabalho foi realizado com apoio da Coordenação de Aperfeiçoamento de Pessoal de Nível Superior - Brasil (CAPES) - Código de Financiamento 001.

Muito Obrigado!

William Nobuhiro Mizobata

Orientador
Antonio C. F. Seridonio

Autor
William N. Mizobata

Ligações moleculares em semimetais de Dirac-Weyl e grafeno bicamada torcido

Resumo

Estudamos teoricamente os estados moleculares de impurezas acopladas à semimetais do tipo Dirac-Weyl e grafeno bicamada torcido. No primeiro caso estudado, consideramos duas impurezas enterradas em um semimetal de Weyl com quebra de simetria de inversão (metal de Weyl). Verificamos uma mudança no padrão dos orbitais moleculares ligante e antiligante, com a emergência de um estado molecular atomicamente frustrado [Physical Review B 102, 075120 (2020)]. No segundo caso, investigamos estados atomicamente frustrados em moléculas diatômicas hospedadas no grafeno bicamada torcido. Encontramos um modo de energia zero nas densidades espectrais dos átomos do dímero ao se quebrar a simetria de inversão na condição do primeiro ângulo mágico. Verificamos que esse modo também é de uma molécula atomicamente frustrada [2D Materials 8, 045038 (2021), Reportagem FAPESP - Torção de bicamada de grafeno gera um novo tipo de ligação molecular (2022)]. Particularmente, esse modo zero é revelado robusto mediante a essa quebra de simetria, como resultado da *twistrônica* do sistema.

Palavras-chaves: Semimetal de Dirac-Weyl, grafeno bicamada torcido, estado atômico frustrado, orbitais moleculares.

Advisor
Antonio C. F. Seridonio

Author
William N. Mizobata

Molecular bonds in Dirac-Weyl semimetals and twisted bilayer graphene

Abstract

We theoretically study the molecular states of impurities coupled to semimetals such as the Dirac-Weyl and twisted bilayer graphene systems. In the first case studied, we consider two impurities buried in a Weyl semimetal with inversion symmetry breaking (Weyl metal). We find a change in the pattern of the bonding and antibonding molecular orbitals, with the emergence of an atomically frustrated molecular state [Physical Review B 102, 075120 (2020)]. In the second case, we investigate the atomically frustrated states in diatomic molecules hosted by a twisted bilayer graphene setup. We find a zero energy mode in the spectral densities of the dimer's atoms just by breaking the inversion symmetry within the first magic angle condition. We also verify that such a mode belongs to an atomically frustrated molecule [2D Materials 8, 045038 (2021), Reportagem FAPESP - Torção de bicamada de grafeno gera um novo tipo de ligação molecular (2022)]. Particularly, this zero mode is revealed robust under this symmetry breaking, as a result of the system *twistronics*.

Keywords: Dirac-Weyl semimetal, twisted billayer graphene, atomic frustrated states, molecular orbital.

Nomenclatura

ARPES Angle-resolved photoemission spectroscopy - Espectroscopia de fotoemissão por ângulo resolvido

EOM Equation of motion - Equação do movimento

IS Inversion symmetry - Simetria de inversão

SIAM Single impurity Anderson model - modelo de Anderson de uma impureza

STM Scanning Tunneling Microscope - Microscópio de varredura por tunelamento

TBG Twister Bilayer Graphene - Grafeno Bicamada Torcido

TIAM Two impurity Anderson model - Modelo de Anderson de duas impurezas

TRS Time reversal symmetry - Simetria de reversão temporal

Lista de Figuras

Sumário

Capítulo 1

Introdução

Em 1928, o físico teórico britânico Paul Adrien Maurice Dirac, propôs uma equação na tentativa de linearizar a equação de Schrödinger, conhecida como equação de Dirac [1, 2]. Tal equação foi capaz de unir a relatividade especial com a mecânica quântica por descrever elétrons relativísticos, ao contrário da equação de Schrödinger. Tais elétrons relativísticos contém uma relação de dispersão linear que é função do módulo do momento, isto é,

$$E(\mathbf{k}) \;=\; C\,|\mathbf{k}|\,, \tag{1.1}$$

sendo C uma constante geral que depende das características do sistema em estudo.

Na física da matéria condensada, este fenômeno pode ser observado em certos materiais que possuem uma relação de dispersão que satisfaz a equação de Dirac, como por exemplo: grafeno, semimetal de Dirac (DSM), semimetal de Weyl (WSM), grafeno bicamada torcido e entre outros.

1.1 Semimetal de Dirac-Weyl

Em 2004 foi sintetizado a primeira folha de grafeno que, devido às suas propriedades físicas que surgem por conta da sua dimensionalidade e estrutura cristalina, se tornou um objeto de estudo muito importante para a física da matéria condensada [3]. O grafeno é um material bidimensional composto por átomos de carbono formando células hexagonais, exibindo uma relação de dispersão linear em sua estrutura de bandas, formando cones de Dirac localizados nos can-

tos da zona de Brillouin [4, 5, 6], como apresenta a Fig. 1.1.

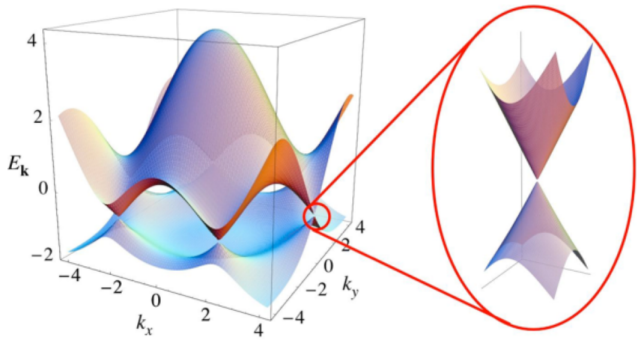

Figura 1.1: Estrutura de bandas do grafeno. Relação de dispersão entre energia $E_{\mathbf{k}}$ e os vetores de onda k_x e k_y. Na região do ponto de Dirac, a estrutura de bandas inferior (valência) e superior (condução) exibe um *gap* pontual conhecido como *pseudogap* (adaptado da Ref. [6]).

Posteriormente, estudos sobre o semimetal de Dirac começou a ganhar destaque por ser um material tridimensional possuindo uma relação de dispersão linear nas três direções no espaço dos momentos [7, 8]. Entre as bandas de valência e de condução desse material, há um *gap* pontual na região do nível de Fermi conhecido como *pseudogap*, contendo pontos de Dirac que, em torno desses pontos, há uma dispersão de quasepartículas dos férmions de Dirac relativísticos com massa efetiva zero [9, 10, 11]. Alguns materiais foram identificados experimentalmente como semimetais de Dirac, sendo esses Cd_3As_2 [12], Na_3Bi [13] e $(Bi_{1-x}In_x)_2Se_3$ [14]. O Halmiltoniano que descreve a relação de dispersão do Dirac é

$$H_\chi(\mathbf{k}) \;=\; v_F \chi \mathbf{k}\cdot\boldsymbol{\sigma}, \tag{1.2}$$

em que $\mathbf{k} = (k_x,\ k_y,\ k_z)$ é o vetor de onda, $\boldsymbol{\sigma} = (\sigma_x,\ \sigma_y,\ \sigma_z)$ são as matrizes de Pauli, v_F é a velocidade de Fermi e $\chi = \pm 1$ é a quiralidade. A quiralidade é definida pela projeção do vetor de *spin* $\mathbf{s}$ no momento linear $\mathbf{p}$ da partícula, isto é,

$$\chi \;=\; \frac{\mathbf{p}\cdot\mathbf{s}}{|\mathbf{p}|\,|\mathbf{s}|}. \tag{1.3}$$

Para esse caso, essa quantidade gera uma estrutura de bandas para $\chi = 1$

e outra para $\chi = -1$. Devido a essa quantidade, é possível verificar uma degenerescência dupla na estrutura de bandas do semimetal de Dirac, ou seja, existem dois cones de Dirac sobrepostos com a mesma energia e no mesmo ponto $\mathbf{k}$. Tal degenerescência é protegida por dois tipos de simetrias: reversão temporal (TRS) e de inversão (IS) [15, 16, 17, 18, 19]. Entretanto, ao quebrar essas simetrias, a degenerescência é perdida tornando-se um semimetal de Weyl [20, 21]. A quebra das simetrias pode gerar uma separação dos cones no espaço dos momentos e(ou) alterar as energias, gerando nós de Weyl com quiralidades definidas. Esses nós de Weyl podem ser vistos como "monopolos magnéticos" no espaço dos momentos (carga quiral e(ou) número de Chern), agindo como emissor e receptor de linhas de campo (curvatura de Berry) [22], como apresentado na Fig. 1.2.

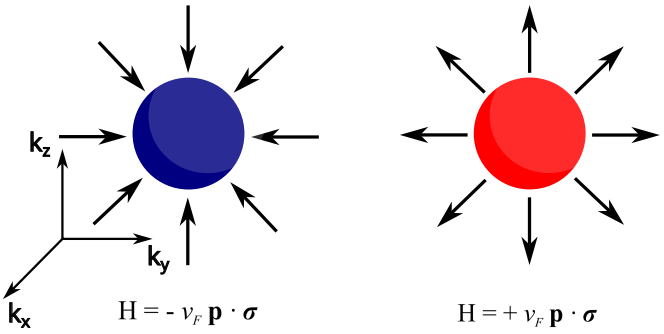

Figura 1.2: Nós de Weyl com quiralidades opostas. As setas representam os vetores de *spin* $\boldsymbol{\sigma}$ que podem ser paralelos ou antiparalelos ao vetor momento $\mathbf{p}$. A quiralidade assume os valores $\chi = \pm 1$.

Esses nós de Weyl são definidos por invariantes topologicos que além de definir a topologia, determina as propriedades exóticas de materiais quanticos topologicos [23]. Esses invariantes quantizados estão enraizados na Fase de Berry γ_m que é adquirida por uma integral de linha no espaço dos momentos das funções de onda de Bloch, definida por

$$\gamma_m = \int_C \mathcal{A}_m(\mathbf{k}) \cdot d\mathbf{k}, \tag{1.4}$$

sendo $\mathcal{A}_m(\mathbf{k})$ chamada de conexão de Berry, definida como

$$\mathcal{A}_m(\mathbf{k}) = i \left\langle m(\mathbf{k}) \left| \frac{\partial}{\partial \mathbf{k}} \right| m(\mathbf{k}) \right\rangle. \tag{1.5}$$

Estendendo a discussão para o invariante topologico relacionado aos nós de Weyl que está associado com o campo da curvatura de Berry definida pelo

rotacional da conexão de Berry, como podemos observar nesta equação

$$\mathbf{\Omega}_m(\mathbf{k}) = \nabla_{\mathbf{k}} \times \mathcal{A}_m(\mathbf{k}), \tag{1.6}$$

descrevendo o comportamento dos férmions de Weyl comoemissor e receptor de campo da curvatura de Berry. Se realizarmos uma integral de superfície do campo da curvatura de Berry envolvendo um nó de Weyl, definido por

$$C_m = \frac{1}{2\pi} \int_S \mathbf{\Omega}_m(\mathbf{k}) \cdot dS, \tag{1.7}$$

resulta em um número inteiro, chamados de número de Chern ou carga quiral, com valores ± 1 representados pela quiralidade.

A conexão entre os nós de Weyl gera a principal assinatura do semimetal conhecida como arcos de Fermi, podendo ser observada experimentalmente por meio da técnica ARPES (do inglês, *Angle-resolved photoemission spectroscopy*) (Fig. 1.3) [24].

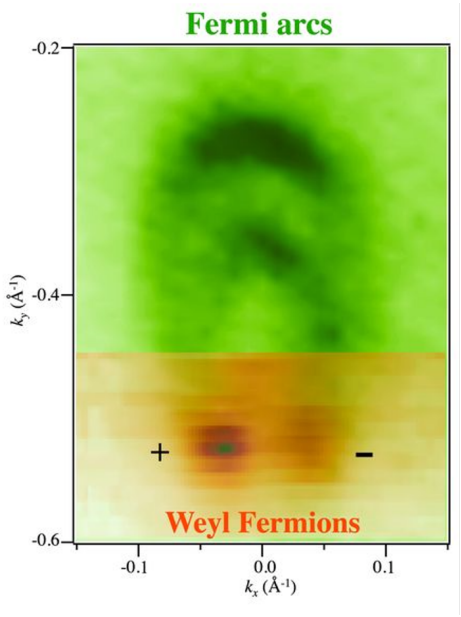

Figura 1.3: Medição obtida por meio da técnica (ARPES) dos arcos de Fermi gerado pelos "monopolos magnéticos" no espaço reciproco (adaptado da Ref. [24]).

Em 2015, o arseneto de tântalo (TaAs) foi o primeiro material identificado como um semimetal de Weyl [25].

O Hamiltoninano que descreve a relação de dispersão do semimetal de Weyl é

$$H_\chi(\mathbf{k}) = \chi\left[\hbar v_F \boldsymbol{\sigma}\cdot(\mathbf{k}-\chi\boldsymbol{Q})+\sigma_0 Q_0\right], \tag{1.8}$$

onde $\boldsymbol{Q}$ é um campo pseudo-magnético responsável pela separação dos cones no espaço $\mathbf{k}$ e Q_0 é responsável pela mudança nas energias dos cones. O campo pseudo-magnético $\boldsymbol{Q}$ pode ser interpretado como um análogo do potencial vetor responsável pelos níveis de Landau, em que os níveis de energia de uma partícula carregada é quantizada sobre a atuação de um campo magnético. A quiralidade, no mesmo contexto, é um análogo à carga da partícula.

Com esse Hamiltoninano, é possível descrever três tipos de semimetais. O regime que preserva as duas simetrias, quando $\boldsymbol{Q}=\mathbf{0}$ e $Q_0=0$, retoma ao Hamiltoniano do Dirac-3D, descrevendo a degenerescência do par de nós de Weyl, resultando em duas bandas de energia sobrepostas (Fig. 1.4(a)). A situação em que temos uma quebra de *IS*, mas que preserva a *TRS*, há uma separação dos nós de Weyl na energia, mas no mesmo ponto $\mathbf{k}$ (Fig. 1.4(b)) [26]. Na outra situação que quebra a *TRS*, mas que preserva a *IS*, temos uma separação das bandas de energia no espaço dos momentos e quiralidades opostas, uma em $-\boldsymbol{Q}$ e a outra em $\boldsymbol{Q}$ (Fig. 1.4(c)) [27]. Com a simetria de inversão preservada, garante que os cones separados tenham a mesma energia.

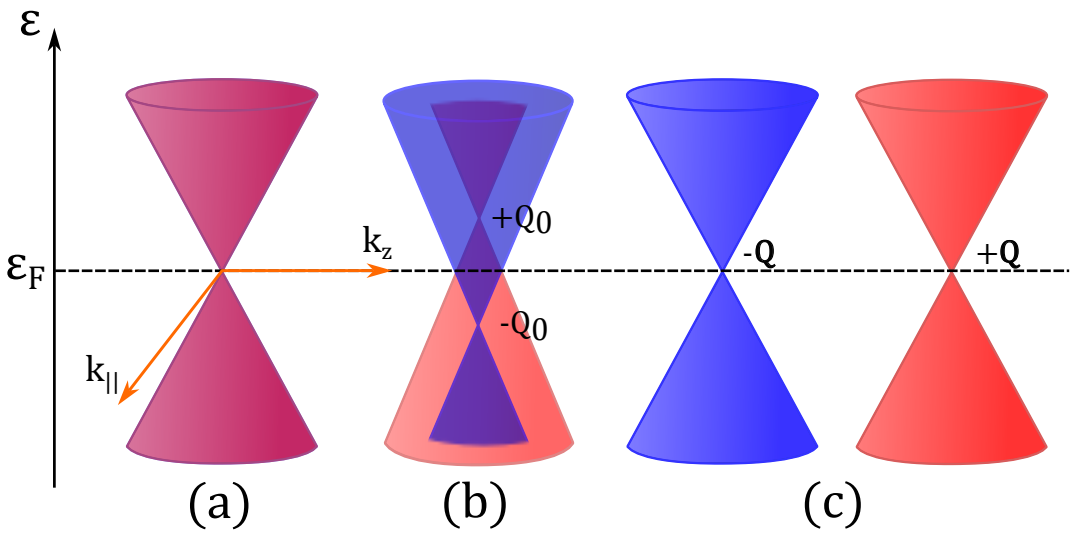

Figura 1.4: Estrutura de bandas: (a) semimetal de Dirac, (b) semimetal de Weyl *noncentrosymmetric* com quebra de IS e TRS preservada, ou metal de Weyl e, (c) Semimetais de Weyl com quebra de TRS e IS preservada. As cores dos cones indicam a quiralidade dos nós de Weyl e o nível de Fermi está localizado em $\varepsilon_F = 0$.

1.2 Grafeno bicamada torcido

O grafeno bicamada torcido (TBG - do inglês Twister Bilayer Graphene) consiste em um empilhamento de dois grafenos [28]. Tal material, leva em conta a ligação entre camadas do tipo Van der Waals. As ligações inter-camadas, diferente das interações intra-camadas que são covalentes, permitem a interação entre duas camadas isoladas possibilitando a criação de materiais heteroestruturados, gerando o surgimento de características únicas para diferentes arranjos [29, 30, 31]. Podem existir em três arranjos distintos: 1) empilhamento AA, onde cada átomo de carbono da camada superior é colocado exatamente acima de seu correspondente na camada inferior (Fig. 1.5(a)); 2) empilhamento AB, ou empilhamento de Bernal, em que os átomos da sub-rede A de uma camada estão alinhados com os átomos da sub-rede B da outra camada (Fig. 1.5(b)); 3) TBG, onde uma camada é rotacionada por algum ângulo θ em relação à outra. Experimentalmente, o empilhamento AA é considerado metaestável, enquanto o empilhamento AB e o TBG são considerados estáveis [28].

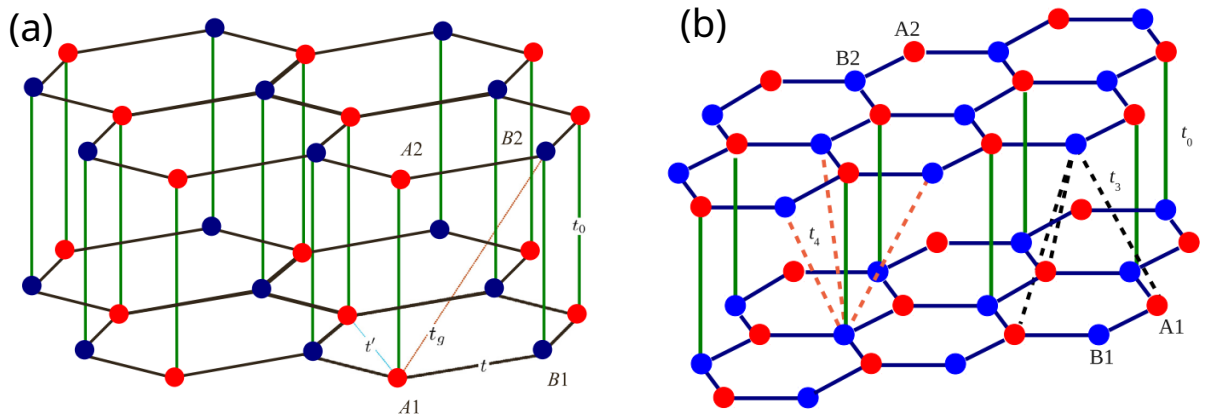

Figura 1.5: (a) Representação do grafeno bicamada com empilhamento AA. Os círculos denotam átomos de carbono nas sub-redes A (vermelho) e B (azul) nas camadas inferior (1) e superior (2). Os termos t referem-se aos saltos entre primeiros e segundos vizinhos e entre as camadas. (b) Representação do empilhamento de Bernal AB (adaptado da Ref. [28]).

O terceiro caso comentado anteriormente, onde existe a possibilidade de manipular o ângulo de torção entre as camadas de grafeno acopladas, vem apresentando propriedades físicas de muito interesse na comunidade científica. Ao realizar uma pequena torção θ entre as camadas, é obtido uma configuração que obedece um padrão de Moiré [32, 33] (ver Fig. 1.6), gerando uma periodicidade em maior escala (super-rede de Moiré).

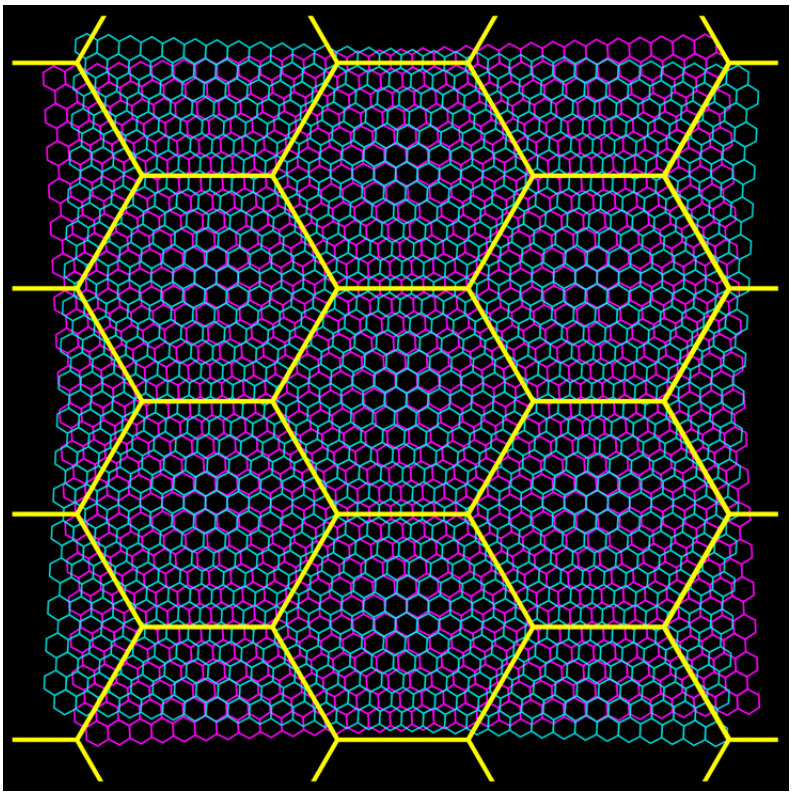

Figura 1.6: Ilustração do grafeno bicamada torcido para um determinado ângulo θ gerando um padrão de Moiré. A torção cria uma super-rede para os elétrons de condução cuja periodicidade é muito maior que o espaçamento entre os átomos de carbono. Para a torção mostrada aqui, os elétrons de condução podem ser tratados como se estivessem se movendo em uma super-rede hexagonal (linhas amarelas) (adaptado da Ref. [34]).

Em pequenos ângulos θ de torção, o TBG apresenta uma preservação dos cones de Dirac encontrados nas camadas isoladas de grafeno no limite de baixas energias, porém com uma velocidade de Fermi renormalizada [35, 36, 37, 38]. Existem valores de ângulos de torção em que a velocidade de Fermi pode chegar a zero, conhecidos como "ângulos mágicos" [39, 40, 41]. A estrutura de bandas para esses valores de ângulos mágicos são conhecidas como bandas chatas (ver Fig. 1.7(c)), devido ao achatamento dos cones de Dirac. Isso resulta em um estado isolante conhecido como isolante de Mott, gerado pelas interações dos elétrons localizados na rede de Moiré [42, 43]. Tal estado, já observado experimentalmente (Fig. 1.7(a-b)), ocorre devido à diminuição da hibridização entre as redes no ângulo mágico, suprimindo a energia cinética dos elétrons. Com a rotação, as zonas de Brillouin das monocamadas geram uma mini-zona de Brillouin a partir do deslocamento dos cones de Dirac das monocamadas de

grafeno (Fig. 1.7(d)).

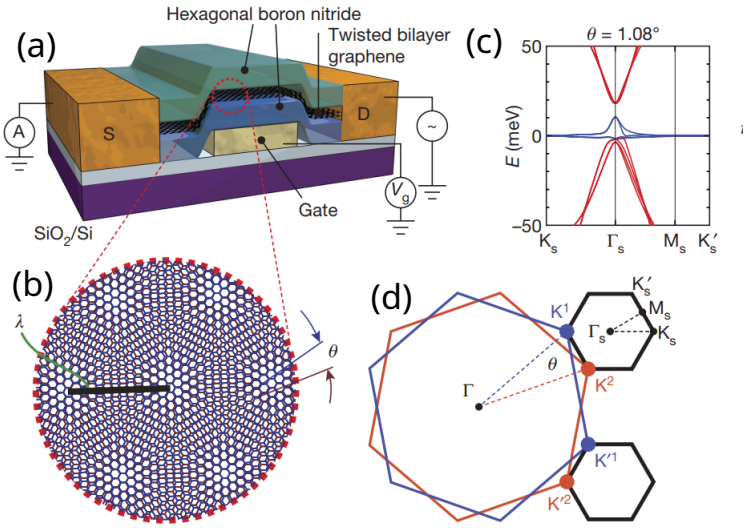

Figura 1.7: (a) Representação do aparato experimental para o estudo do TBG. Foi criada uma estrutura em que o TBG foi encapsulado por camadas hexagonais de nitreto de boro sobre um substrato SiO_2/Si. (b) Representação da rede de Moiré gerada a partir da rotação em θ das camadas de grafeno. (c) Estrutura de banda chata para velocidade de Fermi zero no ângulo mágico $\theta = 1.08º$ (linha azul). (d) Mini-zona de Brillouin, gerada a partir da diferença dos cones de Dirac pela rotação da rede (adaptado da Ref. [32]).

Após essa breve introdução, podemos definir o Hamiltoniano do TBG como

$$H_{TBG} = \hbar\tilde{v}_F\boldsymbol{\sigma}_\xi \cdot \boldsymbol{k} + \xi\sigma_0 V, \tag{1.9}$$

onde $\xi = \pm$ são os índices de vale, $\sigma_\xi = (\xi\sigma_x, \sigma_y)$ são as matrizes de Pauli, V representa a aplicação de uma tensão externa entre as duas camadas e $\tilde{v}_F$ é a velocidade de Fermi renormalizada devido à rotação entre as camadas [35] dada por

$$\tilde{v}_F = \frac{v_F\left(\hbar^2 v_F^2 G^2 - 3w_{AB}^2\right)}{3w_{AA}^2 + 3w_{AB}^2 + \hbar^2 v_F^2 G^2}, \tag{1.10}$$

em que $G = \frac{8\pi\sin\frac{\theta}{2}}{3a}$ é a distância no espaço dos momentos entre os pontos de Dirac em função do ângulo de torção θ entre as monocamadas de grafeno, a é

o parâmetro de rede da monocamada de grafeno, w_{AB} e w_{AA} são os termos de *hopping* dos sítios AB e AA entre as camadas de grafeno, V é a tensão externa aplicada no sistema que define a divisão de energia entre os nós de Dirac (Fig. 1.8(c)), semelhante ao caso do metal de Weyl. O Hamiltoniano na forma matricial é

$$\begin{aligned} H_{TBG} &= \hbar\tilde{v}_F(\xi\sigma_x, \sigma_y)\cdot\boldsymbol{k} + \xi\sigma_0 V \\ &= \begin{pmatrix} \xi V & \hbar\tilde{v}_F(\xi k_x - ik_y) \\ \hbar\tilde{v}_F(\xi k_x + ik_y) & \xi V \end{pmatrix}. \end{aligned} \tag{1.11}$$

A adição de um potencial V pode alterar diretamente a estrutura de bandas do sistema, como no caso do metal de Weyl [26]. No caso do grafeno com duas camadas sem torção com empacotamento AA há uma sobreposição das bandas de energia, fechando o *gap* e gerando um sistema com comportamento metálico. A estrutura de banda se torna similar ao metal de Weyl com quebra de simetria de inversão, ou seja, com as bandas deslocadas na energia, porém, com mesmo momento (Fig. 1.8(a)). Por outro lado, ao realizar uma torção entre as camadas de grafeno, os cones de Dirac são separados com momentos diferentes mas com energias iguais, tendo um *gap* pontual localizada na energia zero (Fig. 1.8(b)). Nesse caso, a aplicação de um potencial V resulta em uma quebra da simetria de inversão, deslocando os cones de Dirac no eixo das energias, gerando um sistema metálico (Fig. 1.8(c)).

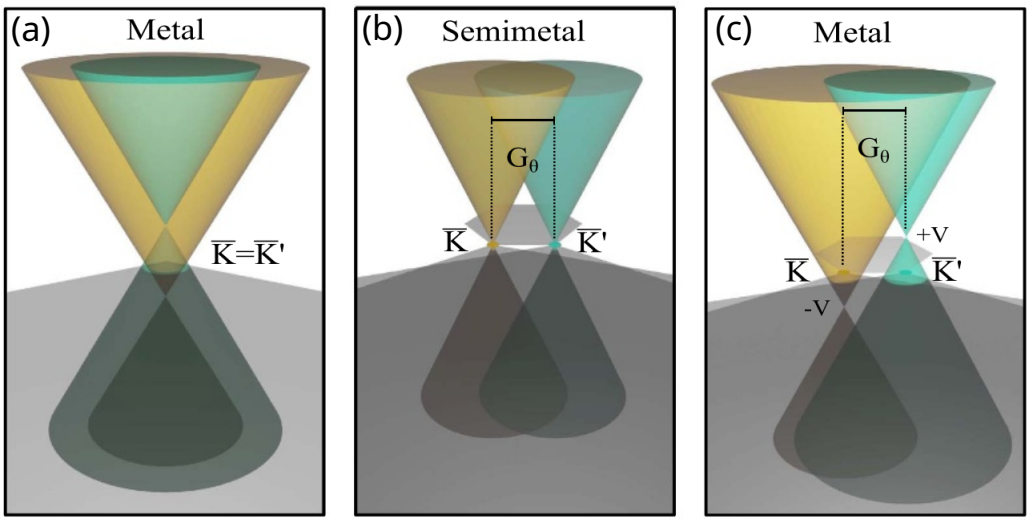

Figura 1.8: Painel (a): Estrutura de bandas para o sistema não torcido no caso do empilhamento AA, com cones de Dirac coincidentes nos cantos de vale $\overline{\mathbf{K}} = \overline{\mathbf{K}'}$, oriundo das zonas de Brillouin superior e inferior das monocamadas, respectivamente. Esses pontos de Dirac aparecem deslocados em energia, devido à simetria de inversão quebrada da fase metálica [28], em analogia aos homólogos metálicos de Weyl [26]. Painel (b): a torção restaura o caráter semimetálico do sistema, mas agora separam os pontos de Dirac em $\overline{\mathbf{K}} \neq \overline{\mathbf{K}'}$ no espaço de momentos por $G_\theta = \frac{8\pi \sin\frac{\theta}{2}}{3a}$, onde a é o parâmetro de rede da monocamada de grafeno. Painel (c): voltagens externas ligadas às monocamadas superior (+V) e inferior (−V) induzem a quebra da simetria de inversão de caráter metálico (adaptado da Ref. [26, 44]).

Portanto, organizamos este trabalho da seguinte forma: No Capítulo 2, abordamos o Hamiltoniano de Anderson que descreve a interação de um hospedeiro com impurezas. Apresentamos o caso de uma e duas impurezas acopladas a um sistema hospedeiro e realizamos uma breve introdução sobre estados moleculares para definir o chamado por nós de estado molecular atomicamente frustrado. No Capítulo 3, introduzimos o formalismo das funções de Green aplicado ao cálculo da equação de movimento dentro da aproximação de Hubbard I [50]. No Capítulo 4, apresentamos os Hamiltonianos de Anderson de Dirac-Weyl e TBG e as principais passagens dos cálculos realizados. No Capítulo 5, discutimos os resultados sobre os sistemas e no Capítulo 6 apresentamos as considerações finais, juntamente com uma lista de artigos produzidos no período.

Capítulo 2

Hamiltoniano de Anderson

Em 1961, o físico estadunidense Philip Warren Anderson propôs um modelo [45] para explicar resultados experimentais em que impurezas com orbitais incompletos d ou f possuem momentos magnéticos bem definidos ao serem dissolvidos em metais simples, como o cobre [46].

Anderson propôs um modelo para descrever a transição de impurezas metálicas em um hospedeiro não magnético, que é capaz de mostrar o comportamento dinâmico das impurezas e, ao mesmo tempo, simples o suficiente para permitir cálculos precisos.

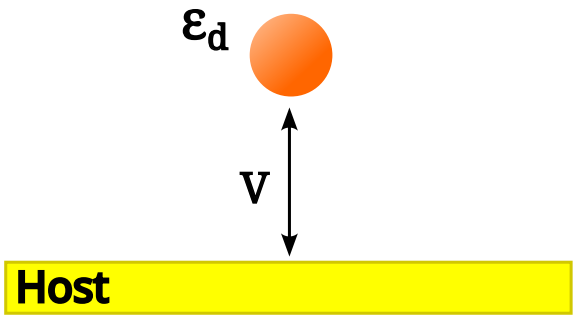

Figura 2.1: Representação do modelo proposto por Anderson de uma impureza adsorvida em um hospedeiro metálico. A intensidade de hibridização é dada pelo parâmetro V entre a impureza (esfera laranja) e o hospedeiro metálico.

2.1 Hamiltoniano de Anderson de uma impureza

No modelo proposto, o metal é representado por elétrons em uma banda com energias $\varepsilon_{\mathbf{k}}$ e números de onda $\mathbf{k}$, enquanto a impureza é representada como um orbital com duas orientações de *spins* $\sigma = \uparrow, \downarrow$ e energia ε_d. A transição de elé-

trons entre os orbitais da impureza e a banda de condução do metal é permitida por um termo de hibridização V. Além disso, Anderson introduziu uma interação de Coulomb repulsiva entre dois elétrons com *spins* opostos para diminuir a probabilidade de ocupação dupla. Esse termo é essencial para a formação de um momento magnético no orbital localizado, pois para ser "magnético" esse orbital deve ser ocupado de forma isolada, com apenas um elétron com um determinado *spin*. Agrupando todos os termos, temos que o Hamiltoniano de Anderson para uma impureza (do inglês Single impurity Anderson model - SIAM) é

$$H_{SIAM} = \sum_{\mathbf{k}\sigma} \varepsilon_k c^\dagger_{\mathbf{k}\sigma} c_{\mathbf{k}\sigma} + \sum_\sigma \varepsilon_d d^\dagger_\sigma d_\sigma + U d^\dagger_\uparrow d_\uparrow d^\dagger_\downarrow d_\downarrow + V \sum_{\mathbf{k}\sigma} \left(c^\dagger_{\mathbf{k}\sigma} d_\sigma + d^\dagger_\sigma c_{\mathbf{k}\sigma} \right), \quad (2.1)$$

onde $c^\dagger_{\mathbf{k}\sigma}(c_{\mathbf{k}\sigma})$ cria (destrói) elétrons de condução com momento $\mathbf{k}$ e *spin* σ, $d^\dagger_\sigma(d_\sigma)$ cria (destrói) elétrons localizados na impureza com *spin* σ. No modelo proposto, $\varepsilon_d = -\frac{U}{2}$ leva à simetria de partícula-buraco e o modelo fica conhecido como Anderson simétrico. Essa simetria pode ser observada na Fig. 2.2, em que uma impureza acoplada em um hospedeiro gera dois picos iguais conhecidos como picos de Hubbard na LDOS em função da energia.

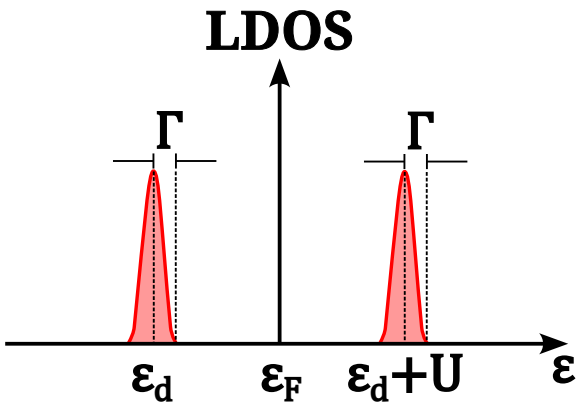

Figura 2.2: Figura esquemática da densidade de estados das impurezas para o modelo de Anderson de uma impureza acoplada a um metal.

Denotamos o Γ como o parâmetro de Anderson, responsável pela semi-largura dos picos de Hubbard. De acordo com a regra de ouro de Fermi [48], o valor de Γ é inversamente proporcional ao tempo de vida do elétron, como podemos ver na seguinte expressão

$$\tau = \frac{\hbar}{2\pi \left|V\right|^2 \rho_0} = \frac{\hbar}{2\Gamma}, \tag{2.2}$$

em que τ é o tempo de vida do elétron num dado nível energético, V é o termo de hibridização e ρ_0 é a densidade de estados do hospedeiro.

2.2 Hamiltoniano de Anderson de duas impurezas

Para o caso em que duas impurezas interagem via um hospedeiro e através de um tunelamento t, o Hamiltoniano de duas impurezas (do inglês Two impurity Anderson model - TIAM) pode ser descrito de maneira semelhante ao caso de uma impureza (SIAM) definido na Eq. (2.1) com o acréscimo de um índice j que contabiliza duas impurezas e o termo de *hopping*, responsável pelo acoplamento entre elas, sendo assim, temos

$$\begin{aligned} H_{TIAM} &= \sum_{\mathbf{k}\sigma} \varepsilon_k c^\dagger_{\mathbf{k}\sigma} c_{\mathbf{k}\sigma} + \sum_{j\sigma} \varepsilon_{jd} d^\dagger_{j\sigma} d_{j\sigma} + \sum_j U_j d^\dagger_{j\uparrow} d_{j\uparrow} d^\dagger_{j\downarrow} d_{j\downarrow} \\ &+ \left(-t \sum_{j\sigma} d^\dagger_{j\sigma} d_{\bar{j}\sigma} \right) + V \sum_{\mathbf{k}j\sigma} \left(c^\dagger_{\mathbf{k}\sigma} d_{j\sigma} + d^\dagger_{j\sigma} c_{\mathbf{k}\sigma} \right), \end{aligned} \tag{2.3}$$

sendo $j = 1, 2$ o índice das impurezas inseridas no sistema e $\bar{j} \neq j$, ou seja, para $j = 1, 2$ temos $\bar{j} = 2, 1$. No termo de tunelamento, temos que $d^\dagger_{j\sigma}$ é o operador de criação em uma dada impureza j, $d_{\bar{j}\sigma}$ o operador de aniquilação na impureza adjacente e t é o termo que representa a amplitude de acoplamento entre as impurezas.

A adição do termo de *hopping* caracterizando a interação entre as impurezas, traz alterações significativas na densidade de estados do sistema. Sendo assim, os picos de Hubbard apresentam um desdobramento caracterizando um estado molecular, como apresentado na Fig 2.3.

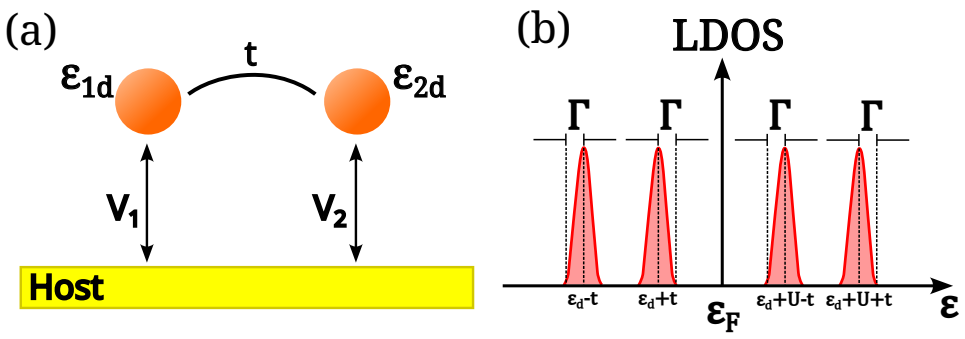

Figura 2.3: (a) Representação do modelo de Anderson de duas impurezas acoplados em um hospedeiro. (b) Representação das densidades de estados das impurezas.

2.3 Orbitais moleculares e o estado molecular atomicamente frustrado

Neste trabalho, será investigado o efeito da inclusão de impurezas em um sistema e como elas podem afetar o comportamento dos elétrons. Essas impurezas podem estar conectadas entre si formando estados moleculares ou permanecerem isoladas em seus estados atômicos. Normalmente, a ligação entre as impurezas é estabelecida por um termo de acoplamento direto entre as mesmas, entretanto esse termo não será necessário neste trabalho (basta fazer $t = 0$ na Eq. (2.3)). Dessa forma, a formação de estados moleculares pode ocorrer de forma menos comum, com a comunicação entre impurezas sendo mediada pelos elétrons do hospedeiro, especificamente em sistemas compostos por semimetais, como os de Dirac-Weyl e grafeno bicamada torcido.

Ao estabelecer uma conexão entre as impurezas, os orbitais atômicos se combinam para formar uma configuração característica de uma molécula. Esse novo orbital é criado através da superposição das funções de onda dos orbitais atômicos. Matematicamente, essa formação do estado molecular pode ser representada pela combinação linear dos orbitais das impurezas. A solução da função de onda obtida pode ser dada pelo cálculo da equação de Schödinger do tipo $H\psi_{\text{mol}} = E\psi_{\text{mol}}$, onde ψ_{mol} representa a função de onda molecular, ou de uma forma mais clara, através da combinação das funções de onda dos átomos, onde o orbital molecular pode ser representado na forma $\psi_{\text{mol}} = C_A\psi_A + C_B\psi_B$, onde C_A e C_B são constantes e ψ_A e ψ_B são as funções de onda referentes aos dois átomos isolados.

Quando os átomos se combinam para a formação molecular, as funções de onda dos orbitais atômicos se sobrepõem, resultando em novos estados energéticos. Esses estados podem ser classificados como ligante ou antiligante, dependendo da energia associada a eles. O estado ligante é caracterizado por uma interferência construtiva entre as funções de onda, levando a uma redistribuição da densidade eletrônica entre os átomos e uma energia menor do que os estados atômicos isolados. Já o estado antiligante é caracterizado por uma interferência destrutiva entre as funções de onda, resultando em repulsão dos orbitais atômicos e uma energia maior do que os estados atômicos isolados.

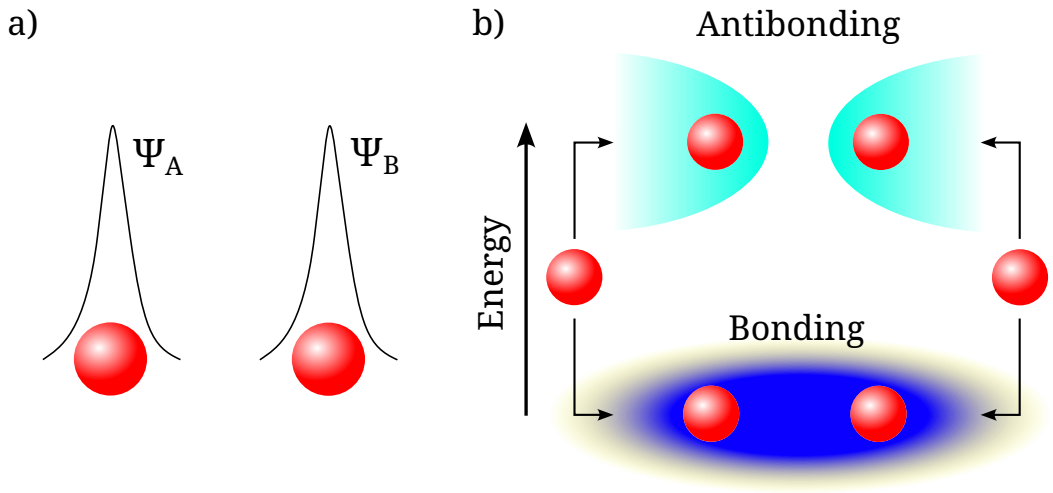

Figura 2.4: (a) Representação das funções de onda dos átomos isolados. (b) Representação de uma molécula formada por dois átomos, resultando em orbitais moleculares ligante e antiligante.

Neste trabalho, analisamos os estados atômicos e a formação de moléculas através da observação dos gráficos de densidades de estados. Essa análise é realizada através dos picos de Hubbard, que são obtidos a partir dos cálculos das funções de Green das impurezas. Essa informação será detalhada no próximo capítulo.

Ao analisar os estados moleculares e atômicos formados por impurezas, é possível observar que as características apresentadas podem esconder a verdadeira natureza da interação entre as mesmas. É possível identificar um estado molecular chamado de estado atômico frustrado, que surge a partir da quebra da simetria devido à variação de um potencial externo. Nesse caso, a assinatura que antes indicava localmente a interação entre as impurezas passa a se assemelhar

à de átomos isolados, mas a troca de informação entre as impurezas ainda é mantida.

Capítulo 3

Formalismo das funções de Green

Como citado anteriormente, os resultados analisados são extraídos via funções de Green, sendo possível, com tal formalismo, calcular a densidade de estados do sistema. A densidade de estados ρ_{LDOS} pode ser definida pela parte imaginária da função de Green retardada do hospedeiro perturbado,

$$\rho_{LDOS}\left(\mathbf{R}\right) = -\frac{1}{\pi}\mathrm{Im}\left[\sum_{\chi}\tilde{\mathcal{G}}_{\chi}^{R}\left(\varepsilon,\mathbf{R}\right)\right]. \tag{3.1}$$

3.1 Funções de Green

As funções de Green são ferramentas fundamentais utilizadas para analisar sistemas quânticos, especialmente aqueles com interações entre as partículas. Elas permitem a obtenção de informações valiosas, como a densidade de estados [47], através de sua relação com as funções de correlação. Neste trabalho, as funções de Green retardada e avançada [48] serão utilizadas para descrever a dispersão de elétrons em nosso sistema, devido a sua capacidade de lidar com problemas de muitos corpos na mecânica quântica.

$$\mathcal{G}^{R}\left(\mathbf{r},t;\mathbf{r}',t'\right) = -i\theta\left(t-t'\right)\left\langle\left[\psi\left(\mathbf{r},t\right),\psi^{\dagger}\left(\mathbf{r}',t'\right)\right]_{+}\right\rangle, \tag{3.2}$$

$$\mathcal{G}^{A}\left(\mathbf{r},t;\mathbf{r}',t'\right) = i\theta\left(t'-t\right)\left\langle\left[\psi\left(\mathbf{r},t\right),\psi^{\dagger}\left(\mathbf{r}',t'\right)\right]_{+}\right\rangle, \tag{3.3}$$

onde $\theta\left(t-t'\right)$ é uma função degrau, $\left[...\right]_{+}$ é a relação de anticomutação e $\left\langle ...\right\rangle$ representa uma média térmica. Tal média térmica é expressa por

$$\left\langle \left[\psi\left(\mathbf{r},t\right),\psi^{\dagger}\left(\mathbf{r}',t'\right)\right]_{+}\right\rangle =\frac{1}{Z}T_{r}\left\{ e^{-\beta H}\left[\psi\left(\mathbf{r},t\right),\psi^{\dagger}\left(\mathbf{r}',t'\right)\right]_{+}\right\} , \tag{3.4}$$

em que $Z = T_r\left\{e^{-\beta H}\right\}$ é a função de partição, T_r representa o traço, $\beta = \frac{1}{k_B T}$ e H é o Hamiltoniano do sistema. Definindo um estado $|n\rangle$ que é um autoestado do Hamiltoniano $\left(H|n\rangle = E|n\rangle\right)$ temos a expressão final das funções de Green retardada e avançada

$$\mathcal{G}^{R}\left(\mathbf{r},t;\mathbf{r}',t'\right)=-i\theta\left(t-t'\right)\sum_{n}\frac{1}{Z}e^{-\beta E_{n}}\langle n\left|\left[\psi\left(\mathbf{r},t\right),\psi^{\dagger}\left(\mathbf{r}',t'\right)\right]_{+}\right|n\rangle, \tag{3.5}$$

$$\mathcal{G}^{A}\left(\mathbf{r},t;\mathbf{r}',t'\right)=i\theta\left(t'-t\right)\sum_{n}\frac{1}{Z}e^{-\beta E_{n}}\langle n\left|\left[\psi\left(\mathbf{r},t\right),\psi^{\dagger}\left(\mathbf{r}',t'\right)\right]_{+}\right|n\rangle, \tag{3.6}$$

que satisfazem a seguinte relação

$$\mathcal{G}^{R}\left(\mathbf{r},t;\mathbf{r}',t'\right)=\left[\mathcal{G}^{A}\left(\mathbf{r},t;\mathbf{r}',t'\right)\right]^{\dagger}. \tag{3.7}$$

Podemos notar que a diferença entre a função de Green retardada e a avançada, é que a primeira é modulada pela função degrau $\theta\left(t-t'\right)$ em que $t < t'$, $\mathcal{G}^{R}\left(\mathbf{r},t;\mathbf{r}',t'\right)=0$, enquanto a segunda, para $t > t'$, $\mathcal{G}^{A}\left(\mathbf{r},t;\mathbf{r}',t'\right)=0$. As funções de Green são definidas no domínio do tempo, porém, de acordo com a Eq. (3.1), a LDOS é proporcional a parte imaginária de uma função de Green no domínio das energias. Contudo, isso pode ser obtido através da transformada de Fourier e o método da equação do movimento. (EOM: equation of motion).

3.2 Equação do movimento (EOM)

Para explicar o método da equação do movimento, utilizaremos uma definição simplificada da função de Green na representação de Heisenberg,

$$\mathcal{G}_{\mathcal{AB}}^{R}\left(t,0\right)=-\frac{i}{\hbar}\theta\left(t-0\right)\left\langle \left[\hat{A}\left(t\right),\hat{B}^{\dagger}\left(0\right)\right]_{+}\right\rangle , \tag{3.8}$$

onde $\hat{A}$ e $\hat{B}$ são operadores fermiônicos e a dependência espacial foi omitida e $t' = 0$. Realizando a transformada de Fourier e levando para o espaço das energias, a função de Green pode ser reescrita por

$$-\frac{i}{\hbar}\left(\varepsilon+i\eta\right)\tilde{\mathcal{G}}^{R}_{\mathcal{AB}}\left(\varepsilon\right)=\int_{-\infty}^{\infty}dt\frac{\partial}{\partial t}\left\{-\frac{i}{\hbar}\theta\left(t-0\right)\left\langle\left[\hat{A}\left(t\right),\hat{B}^{\dagger}\left(0\right)\right]_{+}\right\rangle\right\}e^{\frac{i}{\hbar}(\varepsilon+i\eta)t}, \tag{3.9}$$

sendo que

$$\tilde{\mathcal{G}}^{R}_{\mathcal{AB}}\left(\varepsilon\right)=\int_{-\infty}^{\infty}dt\mathcal{G}^{R}_{\mathcal{AB}}\left(t,0\right)e^{\frac{i}{\hbar}(\varepsilon+i\eta)t}, \tag{3.10}$$

e

$$-\frac{i}{\hbar}\left(\varepsilon+i\eta\right)\tilde{\mathcal{G}}^{R}_{\mathcal{AB}}\left(\varepsilon\right)=\int_{-\infty}^{\infty}dt\frac{\partial}{\partial t}\mathcal{G}^{R}_{\mathcal{AB}}\left(t,0\right)e^{\frac{i}{\hbar}(\varepsilon+i\eta)t}, \tag{3.11}$$

e $\eta\rightarrow0^{+}$ um infinitesimal positivo para que a expressão seja convergente nos limites. Realizando a derivada temporal, temos

$$\begin{aligned}-\frac{i}{\hbar}\left(\varepsilon+i\eta\right)\tilde{\mathcal{G}}^{R}_{\mathcal{AB}}\left(\varepsilon\right) &= -\frac{i}{\hbar}\int_{-\infty}^{\infty}dt\frac{\partial}{\partial t}\theta\left(t-0\right)\left\{\left\langle\left[\hat{A}\left(t\right),\hat{B}^{\dagger}\left(0\right)\right]_{+}\right\rangle\right\}e^{\frac{i}{\hbar}(\varepsilon+i\eta)t}\\ &+ \left(-\frac{i}{\hbar}\right)\int_{-\infty}^{\infty}dt\left\{\theta\left(t-0\right)\left\langle\left[\frac{\partial}{\partial t}\hat{A}\left(t\right),\hat{B}^{\dagger}\left(0\right)\right]_{+}\right\rangle\right\}e^{\frac{i}{\hbar}(\varepsilon+i\eta)t},\end{aligned} \tag{3.12}$$

onde a derivada temporal da função degrau resulta em uma delta de Dirac $\delta\left(t-0\right)$. Enquanto a derivada temporal do operador de aniquilação, pela equação de Heisenberg, é definido por $\frac{\partial\hat{A}(t)}{\partial t}=-\frac{i}{\hbar}\left[\hat{A},H\right]$. Portanto

$$\begin{aligned}-\frac{i}{\hbar}\left(\varepsilon+i\eta\right)\tilde{\mathcal{G}}^{R}_{\mathcal{AB}}\left(\varepsilon\right) &= -\frac{i}{\hbar}\int_{-\infty}^{\infty}dt\delta\left(t-0\right)\left\{\left\langle\left[\hat{A}\left(t\right),\hat{B}^{\dagger}\left(0\right)\right]_{+}\right\rangle\right\}e^{\frac{i}{\hbar}(\varepsilon+i\eta)t}\\ &+ \left(-\frac{i}{\hbar}\right)\int_{-\infty}^{\infty}dt\left\{\theta\left(t-0\right)\left\langle\left[-\frac{i}{\hbar}\left[\hat{A},H\right],\hat{B}^{\dagger}\left(0\right)\right]_{+}\right\rangle\right\}e^{\frac{i}{\hbar}(\varepsilon+i\eta)t}.\end{aligned} \tag{3.13}$$

Resolvendo a integral do primeiro termo, obtemos que

$$\begin{aligned}(\varepsilon+i\eta)\,\tilde{\mathcal{G}}^{R}_{\mathcal{AB}}(\varepsilon) &= \left\langle\left[\hat{A}(0),\hat{B}^{\dagger}(0)\right]_{+}\right\rangle \\ &+ \int_{-\infty}^{\infty}dt\left\{-\frac{i}{\hbar}\theta(t-0)\left\langle\left[\left[\hat{A},H\right],\hat{B}^{\dagger}(0)\right]_{+}\right\rangle\right\}e^{\frac{i}{\hbar}(\varepsilon+i\eta)t} \\ &= \left\langle\left[\hat{A}(0),\hat{B}^{\dagger}(0)\right]_{+}\right\rangle \\ &+ \int_{-\infty}^{\infty}dt\mathcal{G}^{R}_{\left[\hat{A},H\right]\mathcal{B}}(t)\,e^{\frac{i}{\hbar}(\varepsilon+i\eta)t}. \end{aligned} \tag{3.14}$$

Pela definição da equação Eq. (3.8) e Eq. (3.10), temos que o segundo termo é uma nova função de Green $\tilde{\mathcal{G}}^{R}_{\left[\hat{A},H\right]\mathcal{B}}(\varepsilon)$. Portanto

$$(\varepsilon+i\eta)\,\tilde{\mathcal{G}}^{R}_{\mathcal{AB}}(\varepsilon) = \left\langle\left[\hat{A},\hat{B}^{\dagger}\right]_{+}\right\rangle + \tilde{\mathcal{G}}^{R}_{\left[\hat{A},H\right]\mathcal{B}}(\varepsilon). \tag{3.15}$$

A ideia básica deste método é gerar uma série de equações diferenciais acopladas. Como apresentado, o cálculo de $\tilde{\mathcal{G}}^{R}_{\mathcal{AB}}$ gerou uma nova função $\tilde{\mathcal{G}}^{R}_{\left[H,\hat{A}\right]\mathcal{B}}$. O cálculo terminaria apenas quando um conjunto de n equações e n funções de Green é obtido. No entanto, em alguns casos, essa série de equações é infinita, e é necessário recorrer a argumentos físicos para restringir o conjunto de equações de forma adequada, como por exemplo, a aproximação de Hubbard I [50].

3.3 Aproximação de Hubbard I

Considerando um sistema interagente no qual dois elétrons de *spins* opostos não podem ocupar o mesmo estado e, portanto, um deles sendo repelido para um estado $\varepsilon = \varepsilon_d + U$ devido à repulsão de Coulomb, pode-se verificar a presença de funções de Green de alta ordem, como por exemplo $\tilde{\mathcal{G}}_{d_{j\sigma}n_{jd\bar{\sigma}}d_{l\sigma}}$. Após a aplicação do método da EOM na mesma, obtemos a seguinte equação

$$\begin{aligned}(\varepsilon-\varepsilon_{j\sigma}-U_j+i\eta)\,\tilde{\mathcal{G}}_{d_{j\sigma}n_{jd\bar{\sigma}}d_{l\sigma}}(\varepsilon) &= 1-\sum_{\mathbf{k}}V_{j\mathbf{k}}\tilde{\mathcal{G}}_{c^{\dagger}_{\mathbf{k}\bar{\sigma}}d_{j\bar{\sigma}}d_{j\sigma}d_{l\sigma}}(\varepsilon) \\ &+ \sum_{\mathbf{k}}V_{j\mathbf{k}}\tilde{\mathcal{G}}_{d^{\dagger}_{j\bar{\sigma}}c_{\mathbf{k}\bar{\sigma}}d_{j\sigma}d_{l\sigma}}(\varepsilon)+\sum_{\mathbf{k}}V_{j\mathbf{k}}\tilde{\mathcal{G}}_{c_{\mathbf{k}\sigma}d^{\dagger}_{j\bar{\sigma}}d_{j\bar{\sigma}}d_{l\sigma}}(\varepsilon). \end{aligned} \tag{3.16}$$

O cálculo da função de Green de alta ordem originou outras funções de

Green de alta ordem. Ao calcular essas novas funções de Green, surgirão outras funções de Green novas, e assim sucessivamente. Como essa série de equações é infinita, é preciso aplicar um método de aproximação para resolver o conjunto de funções de Green. Neste trabalho, utilizamos o método de aproximação de Hubbard I [50], truncando essas funções de Green através do uso de campo médio, o que pode ser resumido pela seguinte expressão:

$$\tilde{\mathcal{G}}_{\mathcal{ABCD}} = \langle \mathcal{AB} \rangle \tilde{\mathcal{G}}_{\mathcal{CD}}, \tag{3.17}$$

com $\langle \mathcal{AB} \rangle = \langle \mathcal{B}^\dagger \mathcal{A}^\dagger \rangle$. Em certas condições de temperatura, é possível o surgimento do efeito Kondo para $T \ll T_K$, em que T é a temperatura do sistema e T_K a temperatura de Kondo. O efeito Kondo ocorre quando há um acoplamento do tipo antiferromagnético entre os *spins* localizados na impureza e os elétrons de condução próximos ao nível de Fermi do meio hospedeiro. Então, os elétrons de condução formam uma nuvem para blindar o momento magnético localizado na impureza. Consequentemente, observa-se na densidade de estados um pico centrado no nível de Fermi, denominado pico de Kondo. Para o caso dos semimetais de Dirac-Weyl e TBG, não há problema em utilizar a aproximação de Hubbard I mesmo com $T \ll T_K$ devido ao *pseudogap* nas bandas de energia localizado no nível de Fermi em $\varepsilon_F = 0$. Entretanto, é possível estudar o efeito Kondo em um caso de quebra de simetria de inversão e simetria de reversão temporal preservada, pois o nível de Fermi apresenta-se como um nível com um número finito de estados. Porém, mesmo nessa situação, optamos em analisar fora do regime Kondo, isto é, fazemos um cálculo em $T = 0$K e na aproximação de Hubbard I, mas assumindo que $T \gg T_K$ e que a distribuição de Fermi-Dirac pode ser aproximada por uma função degrau, de onde justificamos as hipóteses anteriores.

Aplicando o método descrito pela Eq. (3.17) na Eq. (3.16), temos que:

$$V_{j\mathbf{k}} \tilde{\mathcal{G}}_{c^\dagger_{\mathbf{k}\bar{\sigma}} d_{j\bar{\sigma}} d_{j\sigma} d_{l\sigma}}(\varepsilon) = \langle V^*_{j\mathbf{k}} c^\dagger_{\mathbf{k}\bar{\sigma}} d_{j\bar{\sigma}} \rangle \tilde{\mathcal{G}}_{d_{j\sigma} d_{l\sigma}}(\varepsilon) \tag{3.18}$$

e

$$V_{j\mathbf{k}} \tilde{\mathcal{G}}_{d^\dagger_{j\bar{\sigma}} c_{\mathbf{k}\bar{\sigma}} d_{j\sigma} d_{l\sigma}}(\varepsilon) = \langle V_{j\mathbf{k}} d^\dagger_{j\bar{\sigma}} c_{\mathbf{k}\bar{\sigma}} \rangle \tilde{\mathcal{G}}_{d_{j\sigma} d_{l\sigma}}(\varepsilon). \tag{3.19}$$

Como resultado, a Eq. (3.16) é

$$(\varepsilon - \varepsilon_{j\sigma} - U_j + i\eta) \tilde{\mathcal{G}}_{d_{j\sigma} n_{jd\bar{\sigma}} d_{l\sigma}}(\varepsilon) = 1 + \sum_{\mathbf{k}} V_{j\mathbf{k}} \tilde{\mathcal{G}}_{c_{\mathbf{k}\sigma} d^\dagger_{j\bar{\sigma}} d_{j\bar{\sigma}} d_{l\sigma}}(\varepsilon), \tag{3.20}$$

restando apenas a função de Green $\tilde{\mathcal{G}}_{c_{\mathbf{k}\sigma} d^{\dagger}_{j\bar{\sigma}} d_{j\bar{\sigma}} d_{l\sigma}}(\varepsilon)$ para ser calculada.

Capítulo 4

Hamiltonianos de Dirac-Weyl

Neste capítulo apresentamos dois sistemas estudados durante o doutorado, sendo eles: metal de Weyl. Consideramos um metal de Weyl com um par de impurezas enterradas e separadas por uma distância $\mathbf{R}_{12}$, como apresentado na Fig. 4.1. Sendo assim, estudamos o comportamento da interação entre as impurezas modulado pela quebra de simetria de inversão Q_0. Para investigar esse efeito, calculamos localmente a densidades de estados a partir das funções de Green do hospedeiro.

Portanto, neste capítulo serão apresentados, o Hamiltoniano dos sistemas, os cálculos das funções de Green via método da equação de movimento e os cálculos das funções de Green das impurezas, onde utilizamos a aproximação de Hubbard I.

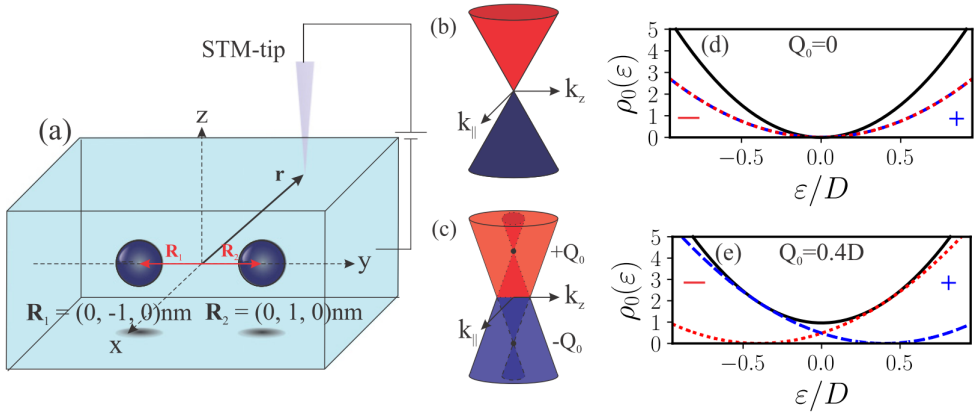

Figura 4.1: (a) Representação do sistema considerado, constituído por um par de impurezas enterradas em um metal de Weyl. As posições das impurezas são caracterizadas pelos vetores $\mathbf{R}_{1,2}$. Os estados moleculares da impureza podem ser sondados na superfície do hospedeiro por uma ponta STM (STM - Scanning Tunneling Microscope), cuja localização é descrita pelo vetor $\mathbf{r}$. (b) Representação da dispersão de um semimetal de Dirac. O *pseudogap* é formado em torno do ponto de Dirac, com densidade de estados (DOS) $\rho(\varepsilon) = 0$. (c) Representação da dispersão do metal de Weyl. Devido à quebra da simetria de inversão, os nós de Weyl são deslocados verticalmente um em relação ao outro. O *pseudogap* é fechado devido ao levantamento da degenerescência dos nós de Weyl. (d) DOS $\rho(\varepsilon)$ de um semimetal de Dirac. (e) DOS $\rho(\varepsilon)$ de um metal de Weyl. Os sinais de mais e menos identificam a DOS resolvida em quiralidades opostas.

4.1 Hamiltoniano do sistema

O Hamiltoniano efetivo que descreve os elétrons livres em um semimetal de Weyl

$$H_0 = \sum_{\mathbf{k}\chi} \psi^\dagger_\chi(\mathbf{k}) h_\chi(\mathbf{k}) \psi_\chi(\mathbf{k}), \tag{4.1}$$

sendo o Hamiltoniano que descreve um par de nós de Weyl de quiralidade oposta

$$h_\chi(\mathbf{k}) = \chi\left[\hbar v_F \boldsymbol{\sigma}\cdot(\mathbf{k} - \chi\boldsymbol{Q}) + \sigma_0 Q_0\right], \tag{4.2}$$

onde $\chi = \pm 1$ refere-se à quiralidade dos nós de Weyl, v_F é a velocidade de Fermi, $\boldsymbol{\sigma} = \{\sigma_x, \sigma_y, \sigma_z\}$ são as matrizes de Pauli, $\mathbf{k}$ é o vetor de onda, $\boldsymbol{Q}$ é o análogo ao potencial vetor responsável pela quebra de simetria de reversão temporal e Q_0 é responsável pelo mudança na energia dos cones devido a quebra de simetria de inversão. Os termos

$$\psi_{\chi}(\mathbf{k}) = \begin{pmatrix} c_{\mathbf{k}\chi\uparrow} \\ c_{\mathbf{k}\chi\downarrow} \end{pmatrix}, \qquad \psi^{\dagger}_{\chi}(\mathbf{k}) = \begin{pmatrix} c^{\dagger}_{\mathbf{k}\chi\uparrow} & c^{\dagger}_{\mathbf{k}\chi\downarrow} \end{pmatrix} \tag{4.3}$$

são *spinores* com operadores fermiônicos de criação e destruição de elétrons em estados quânticos rotulados pelo vetor de onda $\mathbf{k}$, *spin* σ e quiralidade χ. As matrizes de Pauli são

$$\sigma_x = \begin{pmatrix} 0 & 1 \\ 1 & 0 \end{pmatrix}, \quad \sigma_y = \begin{pmatrix} 0 & -i \\ i & 0 \end{pmatrix}, \quad \sigma_z = \begin{pmatrix} 1 & 0 \\ 0 & -1 \end{pmatrix}. \tag{4.4}$$

Para realizar cálculos futuros, realizamos as trocas de variáveis

$$\mathbf{p} = (\mathbf{k} - \chi \boldsymbol{Q}) \tag{4.5}$$

e

$$\mathbf{a} = (\mathbf{q} - \chi \boldsymbol{Q}). \tag{4.6}$$

Assim, o Hamiltoniano pode ser expresso como

$$h_{\chi}(\mathbf{p}) = \chi \left[\hbar v_F \boldsymbol{\sigma} \cdot \mathbf{p} + \sigma_0 Q_0 \right]. \tag{4.7}$$

Aplicando os *spinores* acima no Hamiltoniano, temos

$$\begin{aligned} H_0 &= \sum_{\mathbf{p}\chi} \chi \Big\{ (v_F p_z + Q_0)\, c^{\dagger}_{\mathbf{p}\chi\uparrow} c_{\mathbf{p}\chi\uparrow} + v_F p_- c^{\dagger}_{\mathbf{p}\chi\uparrow} c_{\mathbf{p}\chi\downarrow} \\ &+ v_F p_+ c^{\dagger}_{\mathbf{p}\chi\downarrow} c_{\mathbf{p}\chi\uparrow} + (-v_F p_z + Q_0)\, c^{\dagger}_{\mathbf{p}\chi\downarrow} c_{\mathbf{p}\chi\downarrow} \Big\}, \end{aligned} \tag{4.8}$$

onde $\hbar = 1$ e $p_{\pm} = (p_x \pm i p_y)$ com $p_+ p_- = p_x^2 + p_y^2$.

Adicionando o termo que descreve as impurezas $j = 1, 2$ (modelo de Anderson)

$$H_{imp} = \sum_{j\sigma} \varepsilon_{j\sigma} d^{\dagger}_{j\sigma} d_{j\sigma} + \sum_{j} U_j d^{\dagger}_{j\uparrow} d_{j\uparrow} d^{\dagger}_{j\downarrow} d_{j\downarrow}, \tag{4.9}$$

e o termo de hibridização

$$H_{hyb} = \sum_{j\mathbf{p}\sigma\chi} V_{j\mathbf{p}}(d^{\dagger}_{j\sigma}c_{\mathbf{p}\chi\sigma} + \text{H.c.}), \tag{4.10}$$

no qual $V_{j\mathbf{p}} = \frac{v_0}{\sqrt{\mathcal{N}}}e^{i(\mathbf{p}+\chi\boldsymbol{Q})\cdot\mathbf{R}_j}$. Sendo assim, temos um novo Hamiltoniano

$$\begin{aligned} H &= H_0 + H_{imp} + H_{hyb} \\ &= \sum_{\mathbf{p}\chi} \chi \Big\{ (v_F p_z + Q_0)\, c^{\dagger}_{\mathbf{p}\chi\uparrow} c_{\mathbf{p}\chi\uparrow} + v_F p_- c^{\dagger}_{\mathbf{p}\chi\uparrow} c_{\mathbf{p}\chi\downarrow} \\ &+ v_F p_+ c^{\dagger}_{\mathbf{p}\chi\downarrow} c_{\mathbf{p}\chi\uparrow} + (-v_F p_z + Q_0)\, c^{\dagger}_{\mathbf{p}\chi\downarrow} c_{\mathbf{p}\chi\downarrow} \Big\} \\ &+ \sum_{j\sigma} \varepsilon_{j\sigma} d^{\dagger}_{j\sigma} d_{j\sigma} + \sum_{j\mathbf{p}\sigma\chi} V_{j\mathbf{p}}(d^{\dagger}_{j\sigma}c_{\mathbf{p}\chi\sigma} + \text{H.c.}) + \sum_j U_j d^{\dagger}_{j\uparrow} d_{j\uparrow} d^{\dagger}_{j\downarrow} d_{j\downarrow}. \end{aligned} \tag{4.11}$$

Tendo como objetivo calcular a densidade local de estados (LDOS), por definição temos que

$$\rho_{LDOS}(\varepsilon) = -\frac{1}{\pi}\text{Im}\left[\tilde{\mathcal{G}}(\varepsilon)\right], \tag{4.12}$$

no qual, por hora, omitimos a dependência em $\mathbf{R}_m$. Tendo como ponto de partida a função de Green

$$\mathcal{G}(t) = -\frac{i}{\hbar}\theta(t)\, Z^{-1} \sum_n e^{-\beta E_n} \left\langle n \left| \left[\psi(\mathbf{R}_m, t), \psi^{\dagger}(\mathbf{R}_m, 0)\right]_+ \right| n \right\rangle, \tag{4.13}$$

onde

$$\psi(\mathbf{R}_m, t) = \frac{1}{\sqrt{\mathcal{N}}} \sum_{\mathbf{p}\chi} e^{-i\mathbf{p}\cdot\mathbf{R}_m} \begin{pmatrix} c_{\mathbf{p}\chi\uparrow}(t) \\ c_{\mathbf{p}\chi\downarrow}(t) \end{pmatrix} \tag{4.14}$$

e

$$\psi^{\dagger}(\mathbf{R}_m, t) = \frac{1}{\sqrt{\mathcal{N}}} \sum_{\mathbf{a}\chi} e^{i\mathbf{a}\cdot\mathbf{R}_m} \begin{pmatrix} c^{\dagger}_{\mathbf{a}\chi'\uparrow}(t) & c^{\dagger}_{\mathbf{a}\chi'\downarrow}(t) \end{pmatrix} \tag{4.15}$$

representam os operadores de campo fermiônicos. Portanto, podemos escrever nossa função de Green como

$$\mathcal{G}(t) = \frac{1}{\mathcal{N}} \sum_{\mathbf{pa}} \sum_{\chi\chi'} e^{-i(\mathbf{p}-\mathbf{a})\cdot\mathbf{R}_m} \begin{pmatrix} \mathcal{G}_{c_{\mathbf{p}\chi\uparrow} c_{\mathbf{a}\chi'\uparrow}}(t) & \mathcal{G}_{c_{\mathbf{p}\chi\uparrow} c_{\mathbf{a}\chi'\downarrow}}(t) \\ \mathcal{G}_{c_{\mathbf{p}\chi\downarrow} c_{\mathbf{a}\chi'\uparrow}}(t) & \mathcal{G}_{c_{\mathbf{p}\chi\downarrow} c_{\mathbf{a}\chi'\downarrow}}(t) \end{pmatrix}. \tag{4.16}$$

Definindo em termos da energia e considerando apenas a diagonal prin-

cipal, definimos

$$\tilde{\mathcal{G}}\left(\varepsilon\right)=\frac{1}{\mathcal{N}}\sum_{\mathbf{pa}}\sum_{\sigma\chi\chi'}e^{-i(\mathbf{p}-\mathbf{a})\cdot\mathbf{R}_m}\tilde{\mathcal{G}}_{c_{\mathbf{p}\chi\sigma}c_{\mathbf{a}\chi'\sigma}}\left(\varepsilon\right). \tag{4.17}$$

4.2 Densidade local de estado (LDOS)

Para encontrar a LDOS, é preciso calcular a função de Green

$$\mathcal{G}_{c_{\mathbf{p}\chi\sigma}c_{\mathbf{a}\chi'\sigma'}}\left(t\right)=-\frac{i}{\hbar}\theta\left(t\right)Z^{-1}\sum_{n}e^{-\beta E_n}\left\langle n\left|\left[c_{\mathbf{p}\chi\sigma}\left(t\right),c^{\dagger}_{\mathbf{a}\chi'\sigma'}\left(0\right)\right]_{+}\right|n\right\rangle. \tag{4.18}$$

Para calcular essa função de Green, é preciso evocar o método da equação de movimento (EOM), apresentado na seção 3.2. Sendo assim, temos

$$\begin{aligned}\frac{\partial}{\partial t}\mathcal{G}_{c_{\mathbf{p}\chi\sigma}c_{\mathbf{a}\chi'\sigma'}}\left(t\right) &= -\frac{i}{\hbar}\delta\left(t\right)Z^{-1}\sum_{n}e^{-\beta E_n}\left\langle n\left|\left[c_{\mathbf{p}\chi\sigma}\left(t\right),c^{\dagger}_{\mathbf{a}\chi'\sigma'}\left(0\right)\right]_{+}\right|n\right\rangle\\ &+ \left(-\frac{i}{\hbar}\right)v_F\chi\left(p_+\delta_{\sigma\downarrow}+\left(p_z+Q_0\right)\delta_{\sigma\uparrow}\right)\mathcal{G}_{c_{\mathbf{p}\chi\uparrow}c_{\mathbf{a}\chi'\sigma'}}\left(t\right)\\ &+ \left(-\frac{i}{\hbar}\right)v_F\chi\left(p_-\delta_{\sigma\uparrow}+\left(-p_z+Q_0\right)\delta_{\sigma\downarrow}\right)\mathcal{G}_{c_{\mathbf{p}\chi\downarrow}c_{\mathbf{a}\chi'\sigma'}}\left(t\right)\\ &+ \left(-\frac{i}{\hbar}\right)\sum_{j}V_{j\mathbf{p}}\mathcal{G}_{d_{j\sigma}c_{\mathbf{a}\chi'\sigma'}}\left(t\right).\end{aligned} \tag{4.19}$$

Realizando a transformada de Fourier, temos

$$\begin{aligned}\left(\varepsilon+i\eta\right)\tilde{\mathcal{G}}_{c_{\mathbf{p}\chi\sigma}c_{\mathbf{a}\chi'\sigma'}}\left(\varepsilon\right) &= \delta_{\mathbf{pa}}\delta_{\chi\chi'}\delta_{\sigma\sigma'}+v_F\chi\left(v_Fp_+\delta_{\sigma\downarrow}+\left(v_Fp_z+Q_0\right)\delta_{\sigma\uparrow}\right)\tilde{\mathcal{G}}_{c_{\mathbf{p}\chi\uparrow}c_{\mathbf{a}\chi'\sigma'}}\left(\varepsilon\right)\\ &+ \chi\left(v_Fp_-\delta_{\sigma\uparrow}+\left(-v_Fp_z+Q_0\right)\delta_{\sigma\downarrow}\right)\tilde{\mathcal{G}}_{c_{\mathbf{p}\chi\downarrow}c_{\mathbf{a}\chi'\sigma'}}\left(\varepsilon\right)\\ &+ \sum_{j}V_{j\mathbf{p}}\tilde{\mathcal{G}}_{d_{j\sigma}c_{\mathbf{a}\chi'\sigma'}}\left(\varepsilon\right).\end{aligned} \tag{4.20}$$

Utilizando a Eq. (4.20), podemos escrever quatro funções de Green para $\sigma=\uparrow,\downarrow$ e $\sigma'=\uparrow,\downarrow$

$$\tilde{\mathcal{G}}_{c_{\mathbf{p}\chi\uparrow}c_{\mathbf{a}\chi'\uparrow}}(\varepsilon) = \frac{\delta_{\mathbf{pa}}\delta_{\chi\chi'}}{\tilde{\varepsilon}_\chi - v_F\chi p_z} + \frac{v_F\chi p_-}{\tilde{\varepsilon}_\chi - v_F\chi p_z}\tilde{\mathcal{G}}_{c_{\mathbf{p}\chi\downarrow}c_{\mathbf{a}\chi'\uparrow}}(\varepsilon) + \sum_j \frac{V_{j\mathbf{p}}}{\tilde{\varepsilon}_\chi - v_F\chi p_z}\tilde{\mathcal{G}}_{d_{j\uparrow}c_{\mathbf{a}\chi'\uparrow}}(\varepsilon), \tag{4.21}$$

$$\tilde{\mathcal{G}}_{c_{\mathbf{p}\chi\downarrow}c_{\mathbf{a}\chi'\uparrow}}(\varepsilon) = \frac{v_F\chi p_+}{\tilde{\varepsilon}_\chi + v_F\chi p_z}\tilde{\mathcal{G}}_{c_{\mathbf{p}\chi\uparrow}c_{\mathbf{a}\chi'\uparrow}}(\varepsilon) + \sum_j \frac{V_{j\mathbf{p}}}{\tilde{\varepsilon}_\chi + v_F\chi p_z}\tilde{\mathcal{G}}_{d_{j\downarrow}c_{\mathbf{a}\chi'\uparrow}}(\varepsilon), \tag{4.22}$$

$$\tilde{\mathcal{G}}_{c_{\mathbf{p}\chi\downarrow}c_{\mathbf{a}\chi'\downarrow}}(\varepsilon) = \frac{\delta_{\mathbf{pa}}\delta_{\chi\chi'}}{\tilde{\varepsilon}_\chi + v_F\chi p_z} + \frac{v_F\chi p_+}{\tilde{\varepsilon}_\chi + v_F\chi p_z}\tilde{\mathcal{G}}_{c_{\mathbf{p}\chi\uparrow}c_{\mathbf{a}\chi'\downarrow}}(\varepsilon) + \sum_j \frac{V_{j\mathbf{p}}}{\tilde{\varepsilon}_\chi + v_F\chi p_z}\tilde{\mathcal{G}}_{d_{j\downarrow}c_{\mathbf{a}\chi'\downarrow}}(\varepsilon), \tag{4.23}$$

$$\tilde{\mathcal{G}}_{c_{\mathbf{p}\chi\uparrow}c_{\mathbf{a}\chi'\downarrow}}(\varepsilon) = \frac{v_F\chi p_-}{\tilde{\varepsilon}_\chi - v_F\chi p_z}\tilde{\mathcal{G}}_{c_{\mathbf{p}\chi\downarrow}c_{\mathbf{a}\chi'\downarrow}}(\varepsilon) + \sum_j \frac{V_{j\mathbf{p}}}{\tilde{\varepsilon}_\chi - v_F\chi p_z}\tilde{\mathcal{G}}_{d_{j\uparrow}c_{\mathbf{a}\chi'\downarrow}}(\varepsilon), \tag{4.24}$$

onde nós consideramos $\tilde{\varepsilon}_\chi = \varepsilon + i\eta - \chi Q_0$. Combinando as Eq. (4.21), (4.22), (4.23) e (4.24), temos

$$\tilde{\mathcal{G}}_{c_{\mathbf{p}\chi\uparrow}c_{\mathbf{a}\chi'\uparrow}}(\varepsilon) = \frac{\delta_{\mathbf{pa}}\delta_{\chi\chi'}\left(\tilde{\varepsilon}_\chi + v_F\chi p_z\right)}{\tilde{\varepsilon}_\chi^2 - \left(v_F p\right)^2} + \sum_j \frac{V_{j\mathbf{p}}\left(\tilde{\varepsilon}_\chi + v_F\chi p_z\right)}{\tilde{\varepsilon}_\chi^2 - \left(v_F p\right)^2}\tilde{\mathcal{G}}_{d_{j\uparrow}c_{\mathbf{a}\chi'\uparrow}}(\varepsilon) + \frac{v_F\chi p_- \sum_j V_{j\mathbf{p}}}{\tilde{\varepsilon}_\chi^2 - \left(v_F p\right)^2}\tilde{\mathcal{G}}_{d_{j\downarrow}c_{\mathbf{a}\chi'\uparrow}}(\varepsilon), \tag{4.25}$$

$$\tilde{\mathcal{G}}_{c_{\mathbf{p}\chi\downarrow}c_{\mathbf{a}\chi'\downarrow}}(\varepsilon) = \frac{\delta_{\mathbf{pa}}\delta_{\chi\chi'}\left(\tilde{\varepsilon}_\chi - v_F\chi p_z\right)}{\tilde{\varepsilon}_\chi^2 - \left(v_F p\right)^2} + \sum_j \frac{V_{j\mathbf{p}}\left(\tilde{\varepsilon}_\chi - v_F\chi p_z\right)}{\tilde{\varepsilon}_\chi^2 - \left(v_F p\right)^2}\tilde{\mathcal{G}}_{d_{j\downarrow}c_{\mathbf{a}\chi'\downarrow}}(\varepsilon) + \frac{v_F\chi p_+ \sum_j V_{j\mathbf{p}}}{\tilde{\varepsilon}_\chi^2 - \left(v_F p\right)^2}\tilde{\mathcal{G}}_{d_{j\uparrow}c_{\mathbf{a}\chi'\downarrow}}(\varepsilon), \tag{4.26}$$

Agora, precisamos calcular $\tilde{\mathcal{G}}_{d_{j\sigma}c_{\mathbf{a}\chi'\sigma'}}(\varepsilon)$. Para este caso, utilizamos a função de Green avançada

$$\mathcal{F}_{d_{j\sigma}c_{\mathbf{a}\chi'\sigma'}}(t)=\frac{i}{\hbar}\theta(-t)Z^{-1}\sum_{n}e^{-\beta E_n}\left\langle n\mid\left[d_{j\sigma}^{\dagger}(0),c_{\mathbf{a}\chi'\sigma'}(t)\right]_{+}\mid n\right\rangle . \tag{4.27}$$

Aplicando a EOM e a transformada de Fourier, temos que

$$\begin{aligned}(\varepsilon-i\eta)\,\tilde{\mathcal{F}}_{d_{j\sigma}c_{\mathbf{a}\chi'\sigma'}}(\varepsilon) &= \chi'\left(v_F a_+\delta_{\sigma'\downarrow}+\left(v_F a_z+Q_0\right)\delta_{\sigma'\uparrow}\right)\tilde{\mathcal{F}}_{d_{j\sigma}c_{\mathbf{a}\chi'\uparrow}}(\varepsilon)\\ &+ \chi'\left(v_F a_-\delta_{\sigma'\uparrow}+\left(-v_F a_z+Q_0\right)\delta_{\sigma'\downarrow}\right)\tilde{\mathcal{F}}_{d_{j\sigma}c_{\mathbf{a}\chi'\downarrow}}(\varepsilon)\\ &+ \sum_{l}V_{l\mathbf{a}}\tilde{\mathcal{F}}_{d_{j\sigma}d_{l\sigma'}}(\varepsilon).\end{aligned} \tag{4.28}$$

Aplicando a propriedade $\tilde{\mathcal{G}}_{d_{j\sigma}c_{\mathbf{a}\chi'\sigma'}}(\varepsilon)=\left[\tilde{\mathcal{F}}_{d_{j\sigma}c_{\mathbf{a}\chi'\sigma'}}(\varepsilon)\right]^{\dagger}$, temos a correspondente função de Green retardada

$$\begin{aligned}(\varepsilon+i\eta)\,\tilde{\mathcal{G}}_{d_{j\sigma}c_{\mathbf{a}\chi'\sigma'}}(\varepsilon) &= \chi'\left(v_F a_-\delta_{\sigma'\downarrow}+\left(v_F a_z+Q_0\right)\delta_{\sigma'\uparrow}\right)\tilde{\mathcal{G}}_{d_{j\sigma}c_{\mathbf{a}\chi'\uparrow}}(\varepsilon)\\ &+ \chi'\left(v_F q_+\delta_{\sigma'\uparrow}+\left(-v_F a_z+Q_0\right)\delta_{\sigma'\downarrow}\right)\tilde{\mathcal{G}}_{d_{j\sigma}c_{\mathbf{a}\chi'\downarrow}}(\varepsilon)\\ &+ \sum_{l}V_{l\mathbf{a}}^{*}\tilde{\mathcal{G}}_{d_{j\sigma}d_{l\sigma'}}(\varepsilon).\end{aligned} \tag{4.29}$$

Para $\sigma'=\uparrow,\downarrow$, temos

$$\tilde{\mathcal{G}}_{d_{j\sigma}c_{\mathbf{a}\chi'\uparrow}}(\varepsilon)=\frac{v_F\chi' a_+}{\tilde{\varepsilon}_{\chi'}-v_F\chi' a_z}\tilde{\mathcal{G}}_{d_{j\sigma}c_{\mathbf{a}\chi'\downarrow}}(\varepsilon)+\sum_{l}\frac{V_{l\mathbf{a}}^{*}}{\tilde{\varepsilon}_{\chi'}-v_F\chi' a_z}\tilde{\mathcal{G}}_{d_{j\sigma}d_{l\uparrow}}(\varepsilon), \tag{4.30}$$

e

$$\tilde{\mathcal{G}}_{d_{j\sigma}c_{\mathbf{a}\chi'\downarrow}}(\varepsilon)=\frac{v_F\chi' a_-}{\tilde{\varepsilon}_{\chi'}+v_F\chi' a_z}\tilde{\mathcal{G}}_{d_{j\sigma}c_{\mathbf{a}\chi'\uparrow}}(\varepsilon)+\sum_{l}\frac{V_{l\mathbf{a}}^{*}}{\tilde{\varepsilon}_{\chi'}+v_F\chi' a_z}\tilde{\mathcal{G}}_{d_{j\sigma}d_{l\downarrow}}(\varepsilon). \tag{4.31}$$

Combinando as Eq. (4.30) e Eq. (4.31), temos

$$\tilde{\mathcal{G}}_{d_{j\sigma}c_{\mathbf{a}\chi'\uparrow}}(\varepsilon)=\sum_{l}\frac{\left(\tilde{\varepsilon}_{\chi'}+v_F\chi' a_z\right)V_{l\mathbf{a}}^{*}}{\tilde{\varepsilon}_{\chi'}^{2}-\left(v_F a\right)^{2}}\tilde{\mathcal{G}}_{d_{j\sigma}d_{l\uparrow}}(\varepsilon)+\frac{\sum_{l}v_F\chi' a_+V_{l\mathbf{a}}^{*}}{\tilde{\varepsilon}_{\chi'}^{2}-\left(v_F a\right)^{2}}\tilde{\mathcal{G}}_{d_{j\sigma}d_{l\downarrow}}(\varepsilon), \tag{4.32}$$

$$\tilde{\mathcal{G}}_{d_{j\sigma}c_{\mathbf{a}\chi'\downarrow}}(\varepsilon)=\sum_{l}\frac{\left(\tilde{\varepsilon}_{\chi'}-v_F\chi' a_z\right)V_{l\mathbf{a}}^{*}}{\tilde{\varepsilon}_{\chi'}^{2}-\left(v_F a\right)^{2}}\tilde{\mathcal{G}}_{d_{j\sigma}d_{l\downarrow}}(\varepsilon)+\frac{\sum_l v_F\chi' a_{-}V_{l\mathbf{a}}^{*}}{\tilde{\varepsilon}_{\chi'}^{2}-\left(v_F a\right)^{2}}\tilde{\mathcal{G}}_{d_{j\sigma}d_{l\uparrow}}(\varepsilon). \tag{4.33}$$

Substituindo $\sigma=\uparrow,\downarrow$, obtemos quatro funções de Green

$$\tilde{\mathcal{G}}_{d_{j\uparrow}c_{\mathbf{a}\chi'\uparrow}}(\varepsilon)=\sum_{l}\frac{\left(\tilde{\varepsilon}_{\chi'}+v_F\chi' a_z\right)V_{l\mathbf{a}}^{*}}{\tilde{\varepsilon}_{\chi'}^{2}-\left(v_F a\right)^{2}}\tilde{\mathcal{G}}_{d_{j\uparrow}d_{l\uparrow}}(\varepsilon)+\frac{\sum_l v_F\chi' a_{+}V_{l\mathbf{a}}^{*}}{\tilde{\varepsilon}_{\chi'}^{2}-\left(v_F a\right)^{2}}\tilde{\mathcal{G}}_{d_{j\uparrow}d_{l\downarrow}}(\varepsilon), \tag{4.34}$$

$$\tilde{\mathcal{G}}_{d_{j\downarrow}c_{\mathbf{a}\chi'\uparrow}}(\varepsilon)=\sum_{l}\frac{\left(\tilde{\varepsilon}_{\chi'}+v_F\chi' a_z\right)V_{l\mathbf{a}}^{*}}{\tilde{\varepsilon}_{\chi'}^{2}-\left(v_F a\right)^{2}}\tilde{\mathcal{G}}_{d_{j\downarrow}d_{l\uparrow}}(\varepsilon)+\frac{\sum_l v_F\chi' a_{+}V_{l\mathbf{a}}^{*}}{\tilde{\varepsilon}_{\chi'}^{2}-\left(v_F a\right)^{2}}\tilde{\mathcal{G}}_{d_{j\downarrow}d_{l\downarrow}}(\varepsilon), \tag{4.35}$$

$$\tilde{\mathcal{G}}_{d_{j\uparrow}c_{\mathbf{a}\chi'\downarrow}}(\varepsilon)=\sum_{l}\frac{\left(\tilde{\varepsilon}_{\chi'}-v_F\chi' a_z\right)V_{l\mathbf{a}}^{*}}{\tilde{\varepsilon}_{\chi'}^{2}-\left(v_F a\right)^{2}}\tilde{\mathcal{G}}_{d_{j\uparrow}d_{l\downarrow}}(\varepsilon)+\frac{\sum_l v_F\chi' a_{-}V_{l\mathbf{a}}^{*}}{\tilde{\varepsilon}_{\chi'}^{2}-\left(v_F a\right)^{2}}\tilde{\mathcal{G}}_{d_{j\uparrow}d_{l\uparrow}}(\varepsilon), \tag{4.36}$$

$$\tilde{\mathcal{G}}_{d_{j\downarrow}c_{\mathbf{a}\chi'\downarrow}}(\varepsilon)=\sum_{l}\frac{\left(\tilde{\varepsilon}_{\chi'}-v_F\chi' a_z\right)V_{l\mathbf{a}}^{*}}{\tilde{\varepsilon}_{\chi'}^{2}-\left(v_F a\right)^{2}}\tilde{\mathcal{G}}_{d_{j\downarrow}d_{l\downarrow}}(\varepsilon)+\frac{\sum_l v_F\chi' a_{-}V_{l\mathbf{a}}^{*}}{\tilde{\varepsilon}_{\chi'}^{2}-\left(v_F a\right)^{2}}\tilde{\mathcal{G}}_{d_{j\downarrow}d_{l\uparrow}}(\varepsilon). \tag{4.37}$$

Agora, vamos calcular a função de Green $\mathcal{G}_{c_{\mathbf{p}\chi\sigma}d_{l\sigma'}}(t)$, utilizando a função de Green retardada

$$\mathcal{G}_{c_{\mathbf{p}\chi\sigma}d_{l\sigma'}}(t)=-\frac{i}{\hbar}\theta(t)\,Z^{-1}\sum_{n}e^{-\beta E_n}\left\langle n\left|\left[c_{\mathbf{p}\chi\sigma}(t),d_{l\sigma'}^{\dagger}(0)\right]_{+}\right|n\right\rangle. \tag{4.38}$$

Aplicando a EOM e a transformada de Fourier, temos

$$\begin{aligned}\left(\varepsilon+i\eta\right)\tilde{\mathcal{G}}_{c_{\mathbf{p}\chi\sigma}d_{l\sigma'}}(\varepsilon) &= \chi\left(v_F p_{+}\delta_{\sigma\downarrow}+\left(v_F p_z+Q_0\right)\delta_{\sigma\uparrow}\right)\tilde{\mathcal{G}}_{c_{\mathbf{p}\chi\uparrow}d_{l\sigma'}}(\varepsilon)\\ &+ \chi\left(v_F p_{-}\delta_{\sigma\uparrow}+\left(-v_F p_z+Q_0\right)\delta_{\sigma\downarrow}\right)\tilde{\mathcal{G}}_{c_{\mathbf{p}\chi\downarrow}d_{l\sigma'}}(\varepsilon)\\ &+ \sum_{j}V_{j\mathbf{p}}\tilde{\mathcal{G}}_{d_{j\sigma}d_{l\sigma'}}(\varepsilon).\end{aligned} \tag{4.39}$$

Substituindo $\sigma=\uparrow,\downarrow$, temos

$$\tilde{\mathcal{G}}_{c_{\mathbf{p}\chi\uparrow}d_{l\sigma'}}(\varepsilon)=\frac{v_F\chi p_{-}}{\tilde{\varepsilon}_{\chi}-v_F\chi p_z}\tilde{\mathcal{G}}_{c_{\mathbf{p}\chi\downarrow}d_{l\sigma'}}(\varepsilon)+\sum_{j}\frac{V_{j\mathbf{p}}}{\tilde{\varepsilon}_{\chi}-v_F\chi p_z}\tilde{\mathcal{G}}_{d_{j\uparrow}d_{l\sigma'}}(\varepsilon), \tag{4.40}$$

$$\tilde{\mathcal{G}}_{c_{\mathbf{p}\chi\downarrow}d_{l\sigma'}}(\varepsilon)=\frac{v_F\chi p_+}{\tilde{\varepsilon}_\chi+v_F\chi p_z}\tilde{\mathcal{G}}_{c_{\mathbf{p}\chi\uparrow}d_{l\sigma'}}(\varepsilon)+\sum_j\frac{V_{j\mathbf{p}}}{\tilde{\varepsilon}_\chi+v_F\chi p_z}\tilde{\mathcal{G}}_{d_{j\downarrow}d_{l\sigma'}}(\varepsilon)\,. \tag{4.41}$$

Combinando as Eq. (4.40) e Eq. (4.41), temos

$$\tilde{\mathcal{G}}_{c_{\mathbf{p}\chi\uparrow}d_{l\sigma'}}(\varepsilon)=\sum_j\frac{(\tilde{\varepsilon}_\chi+v_F\chi p_z)\,V_{j\mathbf{p}}}{\tilde{\varepsilon}_\chi^2-(v_Fp)^2}\tilde{\mathcal{G}}_{d_{j\uparrow}d_{l\sigma'}}(\varepsilon)+\frac{\sum_j v_F\chi p_-V_{j\mathbf{p}}}{\tilde{\varepsilon}_\chi^2-(v_Fp)^2}\tilde{\mathcal{G}}_{d_{j\downarrow}d_{l\sigma'}}(\varepsilon)\,, \tag{4.42}$$

$$\tilde{\mathcal{G}}_{c_{\mathbf{p}\chi\downarrow}d_{l\sigma'}}(\varepsilon)=\sum_j\frac{(\tilde{\varepsilon}_\chi-v_F\chi p_z)\,V_{j\mathbf{p}}}{\tilde{\varepsilon}_\chi^2-(v_Fp)^2}\tilde{\mathcal{G}}_{d_{j\downarrow}d_{l\sigma'}}(\varepsilon)+\frac{\sum_j v_F\chi p_+V_{j\mathbf{p}}}{\tilde{\varepsilon}_\chi^2-(v_Fp)^2}\tilde{\mathcal{G}}_{d_{j\uparrow}d_{l\sigma'}}(\varepsilon)\,. \tag{4.43}$$

Substituindo $\sigma'=\uparrow,\downarrow$, ganhamos quatro novas funções de Green

$$\tilde{\mathcal{G}}_{c_{\mathbf{p}\chi\uparrow}d_{l\uparrow}}(\varepsilon)=\sum_j\frac{(\tilde{\varepsilon}_\chi+v_F\chi p_z)\,V_{j\mathbf{p}}}{\tilde{\varepsilon}_\chi^2-(v_Fp)^2}\tilde{\mathcal{G}}_{d_{j\uparrow}d_{l\uparrow}}(\varepsilon)+\frac{\sum_j v_F\chi p_-V_{j\mathbf{p}}}{\tilde{\varepsilon}_\chi^2-(v_Fp)^2}\tilde{\mathcal{G}}_{d_{j\downarrow}d_{l\uparrow}}(\varepsilon)\,, \tag{4.44}$$

$$\tilde{\mathcal{G}}_{c_{\mathbf{p}\chi\uparrow}d_{l\downarrow}}(\varepsilon)=\sum_j\frac{(\tilde{\varepsilon}_\chi+v_F\chi p_z)\,V_{j\mathbf{p}}}{\tilde{\varepsilon}_\chi^2-(v_Fp)^2}\tilde{\mathcal{G}}_{d_{j\uparrow}d_{l\downarrow}}(\varepsilon)+\frac{\sum_j v_F\chi p_-V_{j\mathbf{p}}}{\tilde{\varepsilon}_\chi^2-(v_Fp)^2}\tilde{\mathcal{G}}_{d_{j\downarrow}d_{l\downarrow}}(\varepsilon)\,, \tag{4.45}$$

$$\tilde{\mathcal{G}}_{c_{\mathbf{p}\chi\downarrow}d_{l\uparrow}}(\varepsilon)=\sum_j\frac{(\tilde{\varepsilon}_\chi-v_F\chi p_z)\,V_{j\mathbf{p}}}{\tilde{\varepsilon}_\chi^2-(v_Fp)^2}\tilde{\mathcal{G}}_{d_{j\downarrow}d_{l\uparrow}}(\varepsilon)+\frac{\sum_j v_F\chi p_+V_{j\mathbf{p}}}{\tilde{\varepsilon}_\chi^2-(v_Fp)^2}\tilde{\mathcal{G}}_{d_{j\uparrow}d_{l\uparrow}}(\varepsilon)\,, \tag{4.46}$$

$$\tilde{\mathcal{G}}_{c_{\mathbf{p}\chi\downarrow}d_{l\downarrow}}(\varepsilon)=\sum_j\frac{(\tilde{\varepsilon}_\chi-v_F\chi p_z)\,V_{j\mathbf{p}}}{\tilde{\varepsilon}_\chi^2-(v_Fp)^2}\tilde{\mathcal{G}}_{d_{j\downarrow}d_{l\downarrow}}(\varepsilon)+\frac{\sum_j v_F\chi p_+V_{j\mathbf{p}}}{\tilde{\varepsilon}_\chi^2-(v_Fp)^2}\tilde{\mathcal{G}}_{d_{j\uparrow}d_{l\downarrow}}(\varepsilon)\,. \tag{4.47}$$

Porém, utilizaremos apenas os termos diagonais. Com isso, podemos considerar $\sigma=\sigma'$,

$$\tilde{\mathcal{G}}_{c_{\mathbf{p}\chi\sigma}d_{l\sigma}}(\varepsilon)=\sum_j\frac{(\tilde{\varepsilon}_\chi+\sigma v_F\chi p_z)\,V_{j\mathbf{p}}}{\tilde{\varepsilon}_\chi^2-(v_Fp)^2}\tilde{\mathcal{G}}_{d_{j\sigma}d_{l\sigma}}(\varepsilon)+\frac{\sum_j v_F\chi p_{\bar{\sigma}}V_{j\mathbf{p}}}{\tilde{\varepsilon}_\chi^2-(v_Fp)^2}\tilde{\mathcal{G}}_{d_{j\bar{\sigma}}d_{l\sigma}}(\varepsilon)\,, \tag{4.48}$$

onde o termo $\sigma=1,-1$ para *spin* $\sigma=\uparrow,\downarrow$, respectivamente.

Retomando as Eq. (4.25) e (4.26) e combinando com as Eq. (4.34), (4.35),

(4.36) e (4.37) calculadas anteriormente, obtemos

-

$$\begin{aligned}
\tilde{\mathcal{G}}_{c_{\mathbf{p}\chi\uparrow}c_{\mathbf{a}\chi'\uparrow}}(\varepsilon) &= \frac{\delta_{\mathbf{pa}}\delta_{\chi\chi'}\left(\tilde{\varepsilon}_{\chi}+v_F\chi p_z\right)}{\tilde{\varepsilon}_{\chi}^2-\left(v_Fp\right)^2} \\
&+ \sum_{jl}\left[\frac{V_{j\mathbf{p}}\left(\tilde{\varepsilon}_{\chi}+v_F\chi p_z\right)}{\tilde{\varepsilon}_{\chi}^2-\left(v_Fp\right)^2}\right]\left[\frac{\left(\tilde{\varepsilon}_{\chi'}+v_F\chi' a_z\right)V_{l\mathbf{a}}^*}{\tilde{\varepsilon}_{\chi'}^2-\left(v_Fa\right)^2}\right]\tilde{\mathcal{G}}_{d_{j\uparrow}d_{l\uparrow}}(\varepsilon) \\
&+ \sum_{jl}\left[\frac{V_{j\mathbf{p}}\left(\tilde{\varepsilon}_{\chi}+v_F\chi p_z\right)}{\tilde{\varepsilon}_{\chi}^2-\left(v_Fp\right)^2}\right]\left[\frac{v_F\chi' a_+V_{l\mathbf{a}}^*}{\tilde{\varepsilon}_{\chi'}^2-\left(v_Fa\right)^2}\right]\tilde{\mathcal{G}}_{d_{j\uparrow}d_{l\downarrow}}(\varepsilon) \\
&+ \sum_{jl}\left[\frac{V_{j\mathbf{p}}v_F\chi p_-}{\tilde{\varepsilon}_{\chi}^2-\left(v_Fp\right)^2}\right]\left[\frac{\left(\tilde{\varepsilon}_{\chi'}+v_F\chi' a_z\right)V_{l\mathbf{a}}^*}{\tilde{\varepsilon}_{\chi'}^2-\left(v_Fa\right)^2}\right]\tilde{\mathcal{G}}_{d_{j\downarrow}d_{l\uparrow}}(\varepsilon) \\
&+ \sum_{jl}\left[\frac{V_{j\mathbf{p}}v_F\chi p_-}{\tilde{\varepsilon}_{\chi}^2-\left(v_Fp\right)^2}\right]\left[\frac{v_F\chi' a_+V_{l\mathbf{a}}^*}{\tilde{\varepsilon}_{\chi'}^2-\left(v_Fa\right)^2}\right]\tilde{\mathcal{G}}_{d_{j\downarrow}d_{l\downarrow}}(\varepsilon), \qquad (4.49)
\end{aligned}$$

$$\begin{aligned}
\tilde{\mathcal{G}}_{c_{\mathbf{p}\chi\downarrow}c_{\mathbf{a}\chi'\downarrow}}(\varepsilon) &= \frac{\delta_{\mathbf{pa}}\delta_{\chi\chi'}\left(\tilde{\varepsilon}_{\chi}-v_F\chi p_z\right)}{\tilde{\varepsilon}_{\chi}^2-\left(v_Fp\right)^2} \\
&+ \sum_{jl}\left[\frac{V_{j\mathbf{p}}\left(\tilde{\varepsilon}_{\chi}-v_F\chi p_z\right)}{\tilde{\varepsilon}_{\chi}^2-\left(v_Fp\right)^2}\right]\left[\frac{\left(\tilde{\varepsilon}_{\chi'}-v_F\chi' a_z\right)V_{l\mathbf{a}}^*}{\tilde{\varepsilon}_{\chi'}^2-\left(v_Fa\right)^2}\right]\tilde{\mathcal{G}}_{d_{j\downarrow}d_{l\downarrow}}(\varepsilon) \\
&+ \sum_{jl}\left[\frac{V_{j\mathbf{p}}\left(\tilde{\varepsilon}_{\chi}-v_F\chi p_z\right)}{\tilde{\varepsilon}_{\chi}^2-\left(v_Fp\right)^2}\right]\left[\frac{v_F\chi' a_-V_{l\mathbf{a}}^*}{\tilde{\varepsilon}_{\chi'}^2-\left(v_Fa\right)^2}\right]\tilde{\mathcal{G}}_{d_{j\downarrow}d_{l\uparrow}}(\varepsilon) \\
&+ \sum_{jl}\left[\frac{V_{j\mathbf{p}}v_F\chi p_+}{\tilde{\varepsilon}_{\chi}^2-\left(v_Fp\right)^2}\right]\left[\frac{\left(\tilde{\varepsilon}_{\chi'}-v_F\chi' a_z\right)V_{l\mathbf{a}}^*}{\tilde{\varepsilon}_{\chi'}^2-\left(v_Fa\right)^2}\right]\tilde{\mathcal{G}}_{d_{j\uparrow}d_{l\downarrow}}(\varepsilon) \\
&+ \sum_{jl}\left[\frac{V_{j\mathbf{p}}v_F\chi p_+}{\tilde{\varepsilon}_{\chi}^2-\left(v_Fp\right)^2}\right]\left[\frac{v_F\chi' a_-V_{l\mathbf{a}}^*}{\tilde{\varepsilon}_{\chi'}^2-\left(v_Fa\right)^2}\right]\tilde{\mathcal{G}}_{d_{j\uparrow}d_{l\uparrow}}(\varepsilon). \qquad (4.50)
\end{aligned}$$

Retomando a Eq. (4.17), temos

$$
\begin{aligned}
\mathcal{G}(\varepsilon) &= \frac{1}{\mathcal{N}}\sum_{\mathbf{p}\chi} 2\frac{\tilde{\varepsilon}_{\chi}}{\tilde{\varepsilon}_{\chi}^{2}-\left(v_{F}p\right)^{2}} \\
&+ \frac{1}{v_{0}^{2}}\sum_{\chi\chi'}\sum_{jl}\left[\Sigma_{p_{\sigma z}}^{\chi}\left(\mathbf{R}_{mj}\right)\tilde{\mathcal{G}}_{d_{j\uparrow}d_{l\uparrow}}\left(\varepsilon\right)\Sigma_{a_{\sigma z}}^{\chi'}\left(\mathbf{R}_{lm}\right)\right] \\
&+ \frac{1}{v_{0}^{2}}\sum_{\chi\chi'}\sum_{jl}\left[\Sigma_{p_{\sigma}}^{\chi}\left(\mathbf{R}_{mj}\right)\tilde{\mathcal{G}}_{d_{j\uparrow}d_{l\uparrow}}\left(\varepsilon\right)\Sigma_{a_{\bar{\sigma}}}^{\chi'}\left(\mathbf{R}_{lm}\right)\right] \\
&+ \frac{1}{v_{0}^{2}}\sum_{\chi\chi'}\sum_{jl}\left[\Sigma_{p_{\sigma z}}^{\chi}\left(\mathbf{R}_{mj}\right)\tilde{\mathcal{G}}_{d_{j\uparrow}d_{l\downarrow}}\left(\varepsilon\right)\Sigma_{a_{\sigma}}^{\chi'}\left(\mathbf{R}_{lm}\right)\right] \\
&+ \frac{1}{v_{0}^{2}}\sum_{\chi\chi'}\sum_{jl}\left[\Sigma_{p_{\sigma}}^{\chi}\left(\mathbf{R}_{mj}\right)\tilde{\mathcal{G}}_{d_{j\uparrow}d_{l\downarrow}}\left(\varepsilon\right)\Sigma_{a_{\bar{\sigma}z}}^{\chi'}\left(\mathbf{R}_{lm}\right)\right] \\
&+ \frac{1}{v_{0}^{2}}\sum_{\chi\chi'}\sum_{jl}\left[\Sigma_{p_{\sigma}}^{\chi}\left(\mathbf{R}_{mj}\right)\tilde{\mathcal{G}}_{d_{j\downarrow}d_{l\uparrow}}\left(\varepsilon\right)\Sigma_{a_{\bar{\sigma}z}}^{\chi'}\left(\mathbf{R}_{lm}\right)\right] \\
&+ \frac{1}{v_{0}^{2}}\sum_{\chi\chi'}\sum_{jl}\left[\Sigma_{p_{\sigma z}}^{\chi}\left(\mathbf{R}_{mj}\right)\tilde{\mathcal{G}}_{d_{j\downarrow}d_{l\uparrow}}\left(\varepsilon\right)\Sigma_{a_{\sigma}}^{\chi'}\left(\mathbf{R}_{lm}\right)\right] \\
&+ \frac{1}{v_{0}^{2}}\sum_{\chi\chi'}\sum_{jl}\left[\Sigma_{p_{\sigma}}^{\chi}\left(\mathbf{R}_{mj}\right)\tilde{\mathcal{G}}_{d_{j\downarrow}d_{l\downarrow}}\left(\varepsilon\right)\Sigma_{a_{\bar{\sigma}}}^{\chi'}\left(\mathbf{R}_{lm}\right)\right] \\
&+ \frac{1}{v_{0}^{2}}\sum_{\chi\chi'}\sum_{jl}\left[\Sigma_{p_{\sigma z}}^{\chi}\left(\mathbf{R}_{mj}\right)\tilde{\mathcal{G}}_{d_{j\downarrow}d_{l\downarrow}}\left(\varepsilon\right)\Sigma_{a_{\sigma z}}^{\chi'}\left(\mathbf{R}_{lm}\right)\right], \qquad (4.51)
\end{aligned}
$$

em que $\Sigma_{p_{\sigma z}}^{\chi}$, $\Sigma_{p_{\sigma}}^{\chi}$, $\Sigma_{a_{\sigma z}}^{\chi'}$ e $\Sigma_{a_{\sigma}}^{\chi'}$ são as auto-energias definidas como

$$\Sigma_{p_{\sigma z}}^{\chi} = \frac{v_{0}^{2}}{\mathcal{N}}\sum_{\mathbf{p}}\frac{\tilde{\varepsilon}_{\chi}+\sigma v_{F}\chi p_{z}}{\tilde{\varepsilon}_{\chi}^{2}-\left(v_{F}p\right)^{2}}e^{-i\mathbf{p}\cdot\left(\mathbf{R}_{m}-\mathbf{R}_{j}\right)}e^{-i\chi\boldsymbol{Q}\cdot\left(\mathbf{R}_{m}-\mathbf{R}_{j}\right)}, \qquad (4.52)$$

$$\Sigma_{p_{\sigma}}^{\chi} = \frac{v_{0}^{2}}{\mathcal{N}}\sum_{\mathbf{p}}\frac{v_{F}\chi\left(p_{x}+\sigma ip_{y}\right)}{\tilde{\varepsilon}_{\chi}^{2}-\left(v_{F}p\right)^{2}}e^{-i\mathbf{p}\cdot\left(\mathbf{R}_{m}-\mathbf{R}_{j}\right)}e^{-i\chi\boldsymbol{Q}\cdot\left(\mathbf{R}_{m}-\mathbf{R}_{j}\right)}, \qquad (4.53)$$

$$\Sigma_{a_{\sigma z}}^{\chi'} = \frac{v_{0}^{2}}{\mathcal{N}}\sum_{\mathbf{a}}\frac{\tilde{\varepsilon}_{\chi}+\sigma v_{F}\chi' a_{z}}{\tilde{\varepsilon}_{\chi}^{2}-\left(v_{F}a\right)^{2}}e^{-i\mathbf{a}\cdot\left(\mathbf{R}_{l}-\mathbf{R}_{m}\right)}e^{-i\chi\boldsymbol{Q}\cdot\left(\mathbf{R}_{l}-\mathbf{R}_{m}\right)}, \qquad (4.54)$$

$$\Sigma_{a_{\sigma}}^{\chi'} = \frac{v_{0}^{2}}{\mathcal{N}}\sum_{\mathbf{a}}\frac{v_{F}\chi'\left(a_{x}+\sigma ia_{y}\right)}{\tilde{\varepsilon}_{\chi}^{2}-\left(v_{F}a\right)^{2}}e^{-i\mathbf{a}\cdot\left(\mathbf{R}_{l}-\mathbf{R}_{m}\right)}e^{-i\chi\boldsymbol{Q}\cdot\left(\mathbf{R}_{l}-\mathbf{R}_{m}\right)}. \qquad (4.55)$$

Substituindo a Eq. (4.51) em Eq. (4.12), temos

$$
\begin{aligned}
\rho_{LDOS}\left(\varepsilon\right) &= \rho_0 \\
&- \frac{1}{\pi v_0^2}\sum_{\chi\chi'}\sum_{jl}\mathrm{Im}\left[\Sigma^{\chi}_{p_{\sigma z}}\left(\mathbf{R}_{mj}\right)\tilde{\mathcal{G}}_{d_{j\uparrow}d_{l\uparrow}}\left(\varepsilon\right)\Sigma^{\chi'}_{a_{\sigma z}}\left(\mathbf{R}_{lm}\right)\right] \\
&- \frac{1}{\pi v_0^2}\sum_{\chi\chi'}\sum_{jl}\mathrm{Im}\left[\Sigma^{\chi}_{p_{\sigma}}\left(\mathbf{R}_{mj}\right)\tilde{\mathcal{G}}_{d_{j\uparrow}d_{l\uparrow}}\left(\varepsilon\right)\Sigma^{\chi'}_{a_{\bar{\sigma}}}\left(\mathbf{R}_{lm}\right)\right] \\
&- \frac{1}{\pi v_0^2}\sum_{\chi\chi'}\sum_{jl}\mathrm{Im}\left[\Sigma^{\chi}_{p_{\sigma z}}\left(\mathbf{R}_{mj}\right)\tilde{\mathcal{G}}_{d_{j\uparrow}d_{l\downarrow}}\left(\varepsilon\right)\Sigma^{\chi'}_{a_{\sigma}}\left(\mathbf{R}_{lm}\right)\right] \\
&- \frac{1}{\pi v_0^2}\sum_{\chi\chi'}\sum_{jl}\mathrm{Im}\left[\Sigma^{\chi}_{p_{\sigma}}\left(\mathbf{R}_{mj}\right)\tilde{\mathcal{G}}_{d_{j\uparrow}d_{l\downarrow}}\left(\varepsilon\right)\Sigma^{\chi'}_{a_{\bar{\sigma}z}}\left(\mathbf{R}_{lm}\right)\right] \\
&- \frac{1}{\pi v_0^2}\sum_{\chi\chi'}\sum_{jl}\mathrm{Im}\left[\Sigma^{\chi}_{p_{\sigma}}\left(\mathbf{R}_{mj}\right)\tilde{\mathcal{G}}_{d_{j\downarrow}d_{l\uparrow}}\left(\varepsilon\right)\Sigma^{\chi'}_{a_{\bar{\sigma}z}}\left(\mathbf{R}_{lm}\right)\right] \\
&- \frac{1}{\pi v_0^2}\sum_{\chi\chi'}\sum_{jl}\mathrm{Im}\left[\Sigma^{\chi}_{p_{\sigma z}}\left(\mathbf{R}_{mj}\right)\tilde{\mathcal{G}}_{d_{j\downarrow}d_{l\uparrow}}\left(\varepsilon\right)\Sigma^{\chi'}_{a_{\sigma}}\left(\mathbf{R}_{lm}\right)\right] \\
&- \frac{1}{\pi v_0^2}\sum_{\chi\chi'}\sum_{jl}\mathrm{Im}\left[\Sigma^{\chi}_{p_{\sigma}}\left(\mathbf{R}_{mj}\right)\tilde{\mathcal{G}}_{d_{j\downarrow}d_{l\downarrow}}\left(\varepsilon\right)\Sigma^{\chi'}_{a_{\bar{\sigma}}}\left(\mathbf{R}_{lm}\right)\right] \\
&- \frac{1}{\pi v_0^2}\sum_{\chi\chi'}\sum_{jl}\mathrm{Im}\left[\Sigma^{\chi}_{p_{\sigma z}}\left(\mathbf{R}_{mj}\right)\tilde{\mathcal{G}}_{d_{j\downarrow}d_{l\downarrow}}\left(\varepsilon\right)\Sigma^{\chi'}_{a_{\sigma z}}\left(\mathbf{R}_{lm}\right)\right]
\end{aligned}
\tag{4.56}
$$

em que

$$
\rho_0 = \sum_{\chi}\mathrm{Im}\left[\frac{2}{\pi\mathcal{N}}\sum_{\mathbf{p}}\frac{\left(\varepsilon_\chi + i\eta\right)}{\left(\varepsilon_\chi + i\eta\right)^2 - \left(v_F^2 p^2\right)}\right] \tag{4.57}
$$

é a densidade de estados do semimetal de Weyl. Como resultado dos cálculos da Eq. (4.57), temos

$$
\rho_0\left(\varepsilon\right) = \frac{3}{D^3}\varepsilon_\chi^2 \tag{4.58}
$$

onde a energia é definida por $\varepsilon_\chi = \varepsilon - \chi Q_0$. Quando $Q_0 = 0$, a densidade de estados retoma a expressão do Dirac 3D.

4.3 Função de Green das impurezas

Agora é necessário calcular as funções de Green das impurezas. Por definição, tal função de Green é dada por

$$\mathcal{G}_{d_{j\sigma}d_{l\sigma'}}(t) = -\frac{i}{\hbar}\theta(t)\, Z^{-1}\sum_{n} e^{-\beta E_n}\left\langle n\left|\left[d_{j\sigma}(t), d^{\dagger}_{l\sigma'}(0)\right]_{+}\right|n\right\rangle. \tag{4.59}$$

Aplicando a EOM e a transformada de Fourier

$$\begin{aligned}\left(\varepsilon - \varepsilon_{j\sigma} - \left[\Sigma^{\chi}_{p_{\sigma z}}(0) + \Sigma^{\bar{\chi}}_{p_{\sigma z}}(0)\right] + i\eta\right)\tilde{\mathcal{G}}_{d_{j\sigma}d_{l\sigma}}(\varepsilon) &= \delta_{jl} + U_j\tilde{\mathcal{G}}_{d_{j\sigma}n_{jd\bar{\sigma}}d_{l\sigma}}(\varepsilon) \\ &+ \left[\Sigma^{\chi}_{p_{\sigma z}}\left(\mathbf{R}_{j\bar{j}}\right) + \Sigma^{\bar{\chi}}_{p_{\sigma z}}\left(\mathbf{R}_{j\bar{j}}\right)\right]\tilde{\mathcal{G}}_{d_{\bar{j}\sigma}d_{l\sigma}}(\varepsilon).\end{aligned} \tag{4.60}$$

Agora, temos que calcular

$$\mathcal{G}_{d_{j\sigma}n_{jd\bar{\sigma}}d_{l\sigma}}(t) = -\frac{i}{\hbar}\theta(t)\, Z^{-1}\sum_{n} e^{-\beta E_n}\left\langle n\left|\left[d_{j\sigma}n_{jd\bar{\sigma}}, d^{\dagger}_{l\sigma'}(0)\right]_{+}\right|n\right\rangle. \tag{4.61}$$

Aplicando a EOM e a transformada de Fourier, temos

$$\begin{aligned}\left(\varepsilon - \varepsilon_{j\sigma} - U_j + i\eta\right)\tilde{\mathcal{G}}_{d_{j\sigma}n_{jd\bar{\sigma}}d_{l\sigma}}(\varepsilon) &= \delta_{jl} < n_{jd\bar{\sigma}} > - \sum_{\mathbf{p}\chi} V_{j\mathbf{p}}\tilde{\mathcal{G}}_{c^{\dagger}_{\mathbf{p}\chi\bar{\sigma}}d_{j\bar{\sigma}}d_{j\sigma}d_{l\sigma}}(\varepsilon) \\ &+ \sum_{\mathbf{p}\chi} V_{j\mathbf{p}}\tilde{\mathcal{G}}_{d^{\dagger}_{j\bar{\sigma}}c_{\mathbf{p}\chi\bar{\sigma}}d_{j\sigma}d_{l\sigma}}(\varepsilon) + \sum_{\mathbf{p}\chi} V_{j\mathbf{p}}\tilde{\mathcal{G}}_{c_{\mathbf{p}\chi\sigma}d^{\dagger}_{j\bar{\sigma}}d_{j\bar{\sigma}}d_{l\sigma}}(\varepsilon).\end{aligned} \tag{4.62}$$

Nessa equação, utilizaremos a aproximação de Hubbard I apresentada na seção 3.3

$$\tilde{\mathcal{G}}_{d^{\dagger}_{j\bar{\sigma}}c_{\mathbf{p}\chi\bar{\sigma}}d_{j\sigma}d_{l\sigma}}(\varepsilon) = < V_{j\mathbf{p}}d^{\dagger}_{j\bar{\sigma}}c_{\mathbf{p}\chi\bar{\sigma}} > \tilde{\mathcal{G}}_{d_{j\sigma}d_{l\sigma}}(\varepsilon), \tag{4.63}$$

$$\tilde{\mathcal{G}}_{c^{\dagger}_{\mathbf{p}\chi\bar{\sigma}}d_{j\bar{\sigma}}d_{j\sigma}d_{l\sigma}}(\varepsilon) = < V^{*}_{j\mathbf{p}}c^{\dagger}_{\mathbf{p}\chi\bar{\sigma}}d_{j\bar{\sigma}} > \tilde{\mathcal{G}}_{d_{j\sigma}d_{l\sigma}}(\varepsilon), \tag{4.64}$$

portanto,

$$\left(\varepsilon - \varepsilon_{j\sigma} - U_j + i\eta\right)\tilde{\mathcal{G}}_{d_{j\sigma}n_{jd\bar{\sigma}}d_{l\sigma}}(\varepsilon) = \delta_{jl} < n_{jd\bar{\sigma}} > + \sum_{\mathbf{p}\chi} V_{j\mathbf{p}}\tilde{\mathcal{G}}_{c_{\mathbf{p}\chi\sigma}d^{\dagger}_{j\bar{\sigma}}d_{j\bar{\sigma}}d_{l\sigma}}(\varepsilon). \tag{4.65}$$

Agora, vamos calcular

$$\mathcal{G}_{c_{\mathbf{p}\chi\sigma}d^{\dagger}_{j\bar{\sigma}}d_{j\bar{\sigma}}d_{l\sigma'}}(t)=\left(-\frac{i}{\hbar}\right)\theta(t)\,Z^{-1}\sum_{n}e^{-\beta E_n}\left\langle n\left|\left[c_{\mathbf{p}\chi\sigma}d^{\dagger}_{j\bar{\sigma}}d_{j\bar{\sigma}},d^{\dagger}_{l\sigma'}(0)\right]_{+}\right|n\right\rangle, \tag{4.66}$$

que, aplicando a EOM e a transformada de Fourier, resulta em

$$\begin{aligned}\tilde{\mathcal{G}}_{c_{\mathbf{p}\chi\sigma}n_{jd\bar{\sigma}}d_{l\sigma}}(\varepsilon) &= \frac{V_{j\mathbf{p}}v_F\chi p_{\bar{\sigma}}}{\tilde{\varepsilon}^2_{\chi}-(v_Fp)^2}\tilde{\mathcal{G}}_{d_{j\bar{\sigma}}n_{jd\bar{\sigma}}d_{l\sigma}}(\varepsilon)+\frac{V_{j\mathbf{p}}\left(\tilde{\varepsilon}_{\chi}+\sigma v_F\chi p_z\right)}{\tilde{\varepsilon}^2_{\chi}-(v_Fp)^2}\tilde{\mathcal{G}}_{d_{j\sigma}n_{jd\bar{\sigma}}d_{l\sigma}}(\varepsilon)\\ &+ \frac{V_{\bar{j}\mathbf{p}}v_F\chi p_{\bar{\sigma}}}{\tilde{\varepsilon}^2_{\chi}-(v_Fp)^2}\tilde{\mathcal{G}}_{d_{\bar{j}\bar{\sigma}}n_{jd\bar{\sigma}}d_{l\sigma}}(\varepsilon)+\frac{V_{\bar{j}\mathbf{p}}\left(\tilde{\varepsilon}_{\chi}+\sigma v_F\chi p_z\right)\langle n_{jd\bar{\sigma}}\rangle}{\tilde{\varepsilon}^2_{\chi}-(v_Fp)^2}\tilde{\mathcal{G}}_{d_{\bar{j}\sigma}d_{l\sigma}}(\varepsilon)\end{aligned} \tag{4.67}$$

Substituindo a Eq. (4.65) e Eq. (4.67) em Eq. (4.60) e, deixando em termos de $j=1,2$ e $l=1,2$, temos

$$\tilde{\mathcal{G}}_{d_{1\sigma}d_{1\sigma}}(\varepsilon)=\frac{\lambda^{\bar{\sigma}}_1}{\left(\varepsilon-\varepsilon_{1\sigma}-\tilde{\Sigma}^{\chi}_{p_{\sigma z}}(0)-\lambda^{\bar{\sigma}}_1\lambda^{\bar{\sigma}}_2\frac{\tilde{\Sigma}^{\chi}_{p_{\sigma z}}(\mathbf{R}_{12})\tilde{\Sigma}^{\chi}_{a_{\sigma z}}(\mathbf{R}_{21})}{\left(\varepsilon-\varepsilon_{2\sigma}-\tilde{\Sigma}^{\chi}_{p_{\sigma z}}(0)+i\eta\right)}+i\eta\right)}, \tag{4.68}$$

$$\tilde{\mathcal{G}}_{d_{2\sigma}d_{2\sigma}}(\varepsilon)=\frac{\lambda^{\bar{\sigma}}_2}{\left(\varepsilon-\varepsilon_{2\sigma}-\tilde{\Sigma}^{\chi}_{p_{\sigma z}}(0)-\lambda^{\bar{\sigma}}_1\lambda^{\bar{\sigma}}_2\frac{\tilde{\Sigma}^{\chi}_{p_{\sigma z}}(\mathbf{R}_{21})\tilde{\Sigma}^{\chi}_{a_{\sigma z}}(\mathbf{R}_{12})}{\left(\varepsilon-\varepsilon_{1\sigma}-\tilde{\Sigma}^{\chi}_{p_{\sigma z}}(0)+i\eta\right)}+i\eta\right)}, \tag{4.69}$$

$$\tilde{\mathcal{G}}_{d_{1\sigma}d_{2\sigma}}(\varepsilon)=\frac{\lambda^{\bar{\sigma}}_1\tilde{\Sigma}^{\chi}_{p_{\sigma z}}(\mathbf{R}_{12})}{\left(\varepsilon-\varepsilon_{1\sigma}-\tilde{\Sigma}^{\chi}_{p_{\sigma z}}(0)+i\eta\right)}\tilde{\mathcal{G}}_{d_{2\sigma}d_{2\sigma}}(\varepsilon), \tag{4.70}$$

$$\tilde{\mathcal{G}}_{d_{2\sigma}d_{1\sigma}}(\varepsilon)=\frac{\lambda^{\bar{\sigma}}_2\tilde{\Sigma}^{\chi}_{a_{\sigma z}}(\mathbf{R}_{21})}{\left(\varepsilon-\varepsilon_{2\sigma}-\tilde{\Sigma}^{\chi}_{p_{\sigma z}}(0)+i\eta\right)}\tilde{\mathcal{G}}_{d_{1\sigma}d_{1\sigma}}(\varepsilon), \tag{4.71}$$

onde

$$\tilde{\Sigma}^{\chi}_{p_{\sigma z}}(0)=\Sigma^{\chi}_{p_{\sigma z}}(0)+\Sigma^{\bar{\chi}}_{p_{\sigma z}}(0), \tag{4.72}$$

$$\lambda^{\bar{\sigma}}_j=1+U_j\frac{\langle n_{jd\bar{\sigma}}\rangle}{\left(\varepsilon-\varepsilon_{j\sigma}-U_j-\left[\Sigma^{\chi}_{p_{\sigma z}}(0)+\Sigma^{\bar{\chi}}_{p_{\sigma z}}(0)\right]+i\eta\right)}. \tag{4.73}$$

Agora, vamos realizar os cálculos das auto-energias não interagentes que descrevem as formas como as impurezas sentem o sistema em que estão adsorvidas. Temos duas situações para realizar o cálculo: $R\neq 0$ e $R=0$.

4.4 Auto-energia para $\mathbf{R} \neq 0$

Primeiramente, vamos calcular $\Sigma^{\chi}_{p_\sigma}$. Para calcular esta auto-energia, é preciso converter a somatória para coordenadas esféricas,

$$\sum_{\vec{p}} = \frac{\Omega}{(2\pi)^3}\int_0^{\infty}\int_0^{\pi}\int_0^{2\pi} p^2 sin\theta dp d\theta d\phi. \tag{4.74}$$

Sendo assim, temos que

$$\begin{aligned}
\Sigma^{\chi}_{p_\sigma} &= e^{-i\chi \boldsymbol{Q}\cdot\mathbf{R}_{mj}}\frac{v_0^2 v_F \chi\Omega}{\mathcal{N}(2\pi)^3}\int_0^{\infty}\int_0^{\pi}\int_0^{2\pi} p^2 sin\theta dp d\theta d\phi \frac{(p_x+\sigma i p_y)\, e^{-i\mathrm{p}\cdot\mathbf{R}_{mj}}}{\varepsilon_\chi^2-(v_F p)^2} \\
&= e^{-i\chi \boldsymbol{Q}\cdot\mathbf{R}_{mj}}\frac{v_0^2 v_F \chi\Omega}{\mathcal{N}(2\pi)^3}\int_0^{\infty}\int_0^{\pi} p^2 sin\theta dp d\theta \frac{p sin\theta e^{-ip|\mathbf{R}_{mj}|cos\theta}}{\varepsilon_\chi^2-(v_F p)^2}\int_0^{2\pi} cos\phi d\phi \\
&+ e^{-i\chi \boldsymbol{Q}\cdot\mathbf{R}_{mj}}\sigma i\frac{v_0^2 v_F \chi\Omega}{\mathcal{N}(2\pi)^3}\int_0^{\infty}\int_0^{\pi} p^2 sin\theta dp d\theta \frac{p sin\theta e^{-ip|\mathbf{R}_{mj}|cos\theta}}{\varepsilon_\chi^2-(v_F p)^2}\int_0^{2\pi} sin\phi d\phi \\
&= e^{-i\chi \boldsymbol{Q}\cdot\mathbf{R}_{mj}}\frac{v_0^2 v_F \chi\Omega}{\mathcal{N}(2\pi)^3}\int_0^{\infty}\int_0^{\pi} p^2 sin\theta dp d\theta \frac{p sin\theta e^{-ip|\mathbf{R}_{mj}|cos\theta}}{\varepsilon_\chi^2-(v_F p)^2}\left[sin\phi\right]_0^{2\pi} \\
&+ e^{-i\chi \boldsymbol{Q}\cdot\mathbf{R}_{mj}}\sigma i\frac{v_0^2 v_F \chi\Omega}{\mathcal{N}(2\pi)^3}\int_0^{\infty}\int_0^{\pi} p^2 sin\theta dp d\theta \frac{p sin\theta e^{-ip|\mathbf{R}_{mj}|cos\theta}}{\varepsilon_\chi^2-(v_F p)^2}\left[cos\phi\right]_0^{2\pi} \\
&= 0.
\end{aligned} \tag{4.75}$$

Este resultado é válido para $\Sigma^{\chi}_{a_\sigma}$. Portanto, a Eq. (4.56) pode ser escrita como

$$\begin{aligned}
\rho_{LDOS}(\varepsilon) &= \sum_{\chi}\rho_0 \\
&+ \frac{1}{\pi v_0^2}\sum_{\chi\chi'}\sum_{jl}\left[\Sigma^{\chi}_{p_{\sigma z}}(\mathbf{R}_{mj})\,\tilde{\mathcal{G}}_{d_{j\uparrow}d_{l\uparrow}}(\varepsilon)\,\Sigma^{\chi'}_{a_{\sigma z}}(\mathbf{R}_{lm}) + \Sigma^{\chi}_{p_{\sigma z}}(\mathbf{R}_{mj})\,\tilde{\mathcal{G}}_{d_{j\downarrow}d_{l\downarrow}}(\varepsilon)\,\Sigma^{\chi'}_{a_{\sigma z}}(\mathbf{R}_{lm})\right],
\end{aligned} \tag{4.76}$$

ou

$$\boxed{\rho_{LDOS}(\varepsilon) = \rho_0 + \frac{1}{\pi v_0^2}\sum_{\chi\chi'}\sum_{jl}\sum_{\sigma}\left[\Sigma^{\chi}_{\sigma}(\mathbf{R}_{mj})\,\tilde{\mathcal{G}}_{d_{j\sigma}d_{l\sigma}}(\varepsilon)\,\Sigma^{\chi'}_{\sigma}(\mathbf{R}_{lm})\right].} \tag{4.77}$$

Agora, vamos calcular a auto energia Σ^{χ}_{σ}

$$\begin{aligned}
\Sigma_{\sigma}^{\chi} &= e^{-i\chi \boldsymbol{Q}\cdot\mathbf{R}_{mj}} \frac{v_0^2\Omega}{\mathcal{N}\left(2\pi\right)^3} \int_0^{\infty}\int_0^{\pi}\int_0^{2\pi} p^2 sin\theta dp d\theta d\phi \frac{\varepsilon_{\chi} e^{-i\mathbf{p}\cdot\mathbf{R}_{mj}}}{\varepsilon_{\chi}^2 - \left(v_F p\right)^2} \\
&+ \sigma e^{-i\chi \boldsymbol{Q}\cdot\mathbf{R}_{mj}} \frac{v_0^2\Omega v_F\chi}{\mathcal{N}\left(2\pi\right)^3} \int_0^{\infty\pi}\int_0^{2\pi} p^2 sin\theta dp d\theta d\phi \frac{p_z e^{-i\mathbf{p}\cdot\mathbf{R}_{mj}}}{\tilde{\varepsilon}_{\chi}^2 - \left(v_F p\right)^2} \\
&= e^{\mp i\chi \boldsymbol{Q}\cdot\mathbf{R}_{mj}} \frac{v_0^2\Omega}{\mathcal{N}\left(2\pi\right)^3} \int_0^{\infty}\int_0^{\pi}\int_0^{2\pi} p^2 sin\theta dp d\theta d\phi \frac{\varepsilon_{\chi} e^{\mp ip|\mathbf{R}_{mj}|cos\theta}}{\varepsilon_{\chi}^2 - \left(v_F p\right)^2} \\
&+ \sigma e^{\mp i\chi \boldsymbol{Q}\cdot\mathbf{R}_{mj}} \frac{v_0^2\Omega v_F\chi}{\mathcal{N}\left(2\pi\right)^3} \int_0^{\infty}\int_0^{\pi}\int_0^{2\pi} p^3 sin\theta cos\theta dp d\theta d\phi \frac{e^{\mp ip|\mathbf{R}_{mj}|cos\theta}}{\tilde{\varepsilon}_{\chi}^2 - \left(v_F p\right)^2}, \qquad (4.78)
\end{aligned}$$

em que $\mp$ representa o sinal para p e a, respectivamente. Calculando o primeiro termo da Eq. (4.78)

$$\begin{aligned}
I_1 &= e^{\mp i\chi \boldsymbol{Q}\cdot\mathbf{R}_{mj}} \frac{v_0^2\Omega}{\mathcal{N}\left(2\pi\right)^3} 2\pi \int_0^{\infty}\int_0^{\pi} p^2 sin\theta dp d\theta \frac{\varepsilon_{\chi} e^{\mp i\mathbf{p}\cdot\mathbf{R}_{mj}}}{\varepsilon_{\chi}^2 - \left(v_F p\right)^2} \\
&= e^{\mp i\chi \boldsymbol{Q}\cdot\mathbf{R}_{mj}} \frac{v_0^2\Omega}{\mathcal{N}\left(2\pi\right)^3} 2\pi \int_0^{\infty} p^2 dp \frac{\varepsilon_{\chi}}{\varepsilon_{\chi}^2 - \left(v_F p\right)^2} \int_0^{\pi} sin\theta e^{\mp ip|\mathbf{R}_{mj}|cos\theta} d\theta \\
&= e^{\mp i\chi \boldsymbol{Q}\cdot\mathbf{R}_{mj}} \frac{v_0^2\Omega}{\mathcal{N}\left(2\pi\right)^3} 2\pi \int_0^{\infty} p^2 dp \frac{\varepsilon_{\chi}}{\varepsilon_{\chi}^2 - \left(v_F p\right)^2} \int_0^{\pi} sin\theta e^{\mp ip|\mathbf{R}_{mj}|cos\theta} d\theta, \qquad (4.79)
\end{aligned}$$

pelo método de substituição de variável, vamos definir $u = \mp ip \mid \mathbf{R}_{mj} \mid \cos\theta$ e derivando com relação a θ, temos $du = \pm ip \mid \mathbf{R}_{mj} \mid sen\theta d\theta$, a parte angular torna-se

$$\begin{aligned}
\int_0^{\pi} d\theta sin\theta e^{\mp ip|\mathbf{R}_{mj}|cos\theta} &= \int \frac{1}{\pm ip \mid \mathbf{R}_{mj} \mid} e^a da \\
&= \frac{1}{\pm ip \mid \mathbf{R}_{mj} \mid} \left[e^{\mp ip|\mathbf{R}_{mj}|cos\theta}\right]_0^{\pi} \\
&= \frac{1}{\pm ip \mid \mathbf{R}_{mj} \mid} \left(e^{\pm ip|\mathbf{R}_{mj}|} - e^{\mp ip|\mathbf{R}_{mj}|}\right), \qquad (4.80)
\end{aligned}$$

sendo assim

$$
\begin{aligned}
I_1 &= e^{\mp i\chi \boldsymbol{Q}\cdot\mathbf{R}_{mj}} \frac{v_0^2\Omega}{\mathcal{N}\left(2\pi\right)^2} \int_0^\infty p^2 dp \frac{\varepsilon_\chi}{\varepsilon_\chi^2 - \left(v_F p\right)^2} \left(\frac{1}{\pm ip \mid \mathbf{R}_{mj} \mid} e^{\pm ip|\mathbf{R}_{mj}|} - \frac{1}{\pm ip \mid \mathbf{R}_{mj} \mid} e^{\mp ip|\mathbf{R}_{mj}|} \right) \\
&= \pm e^{\mp i\chi \boldsymbol{Q}\cdot\mathbf{R}_{mj}} \frac{v_0^2\Omega}{\mathcal{N} i \mid \mathbf{R}_{mj} \mid \left(2\pi\right)^2} \int_0^\infty p dp \frac{\varepsilon_\chi}{\varepsilon_\chi^2 - \left(v_F p\right)^2} \left(e^{\pm ip|\mathbf{R}_{mj}|} - e^{\mp ip|\mathbf{R}_{mj}|} \right) \\
&= \pm e^{\mp i\chi \boldsymbol{Q}\cdot\mathbf{R}_{mj}} \frac{v_0^2\Omega}{\left(2\pi\right)^2 \mathcal{N} i \mid \mathbf{R}_{mj} \mid} \int_0^\infty p dp \frac{\varepsilon_\chi}{\left(v_F p\right)^2 - \varepsilon_\chi^2} \left(e^{\mp ip|\mathbf{R}_{mj}|} - e^{\pm ip|\mathbf{R}_{mj}|} \right) \\
&= -e^{\mp i\chi \boldsymbol{Q}\cdot\mathbf{R}_{mj}} \frac{v_0^2\Omega\varepsilon_\chi}{\left(2\pi\right)^2 \mathcal{N} i \mid \mathbf{R}_{mj} \mid} \int_{-\infty}^\infty dp \frac{p}{\left(v_F p\right)^2 - \varepsilon_\chi^2} \left(e^{ip|\mathbf{R}_{mj}|} \right), \qquad (4.81)
\end{aligned}
$$

resultando em

$$
I_1 = -e^{\mp i\chi \boldsymbol{Q}\cdot\mathbf{R}_{mj}} \frac{v_0^2\Omega\varepsilon_\chi}{\left(2\pi\right)^2 \mathcal{N} i \mid \mathbf{R}_{mj} \mid v_F^2} \int_{-\infty}^\infty dp \frac{p}{p^2 - \frac{\varepsilon_\chi^2}{v_F^2}} \left(e^{ip|\mathbf{R}_{mj}|} \right). \qquad (4.82)
$$

Agora, vamos calcular o segundo termo

$$
I_2 = \sigma e^{\mp i\chi \boldsymbol{Q}\cdot\mathbf{R}_{mj}} \frac{v_0^2\Omega v_F\chi}{\mathcal{N}\left(2\pi\right)^3} \int_0^\infty \int_0^\pi \int_0^{2\pi} p^3 sin\theta cos\theta dp d\theta d\phi \frac{e^{\mp ip|\mathbf{R}_{mj}|cos\theta}}{\varepsilon_\chi^2 - \left(v_F p\right)^2}. \qquad (4.83)
$$

Pelo método de substituição de variável, como utilizada na Eq. (4.79), temos

$$
\begin{aligned}
\int_0^\pi sin\theta cos\theta e^{\mp ip|\mathbf{R}_{mj}|cos\theta} d\theta &= \int_{\mp ip|\mathbf{R}_{mj}|}^{\pm ip|\mathbf{R}_{mj}|} \left(\pm \frac{da}{ip \mid \mathbf{R}_{mj} \mid} \right) \left(\mp \frac{a}{ip \mid \mathbf{R}_{mj} \mid} \right) e^a \\
&= \frac{1}{\left(p \mid \mathbf{R}_{mj} \mid\right)^2} \int_{\mp ip|\mathbf{R}_{mj}|}^{\pm ip|\mathbf{R}_{mj}|} a e^a da, \qquad (4.84)
\end{aligned}
$$

sendo assim

$$
\begin{aligned}
u &= a, \qquad (4.85) \\
du &= da, \qquad (4.86) \\
v &= e^a, \qquad (4.87) \\
dv &= e^a da, \qquad (4.88)
\end{aligned}
$$

portanto

$$\begin{aligned}
\frac{1}{(p \mid \mathbf{R}_{mj} \mid)^2}\int ae^a da &= \frac{1}{(p \mid \mathbf{R}_{mj} \mid)^2}\left\{[ae^a]_{\mp ip|\mathbf{R}_{mj}|}^{\pm ip|\mathbf{R}_{mj}|} - \int_{\mp ip|\mathbf{R}_{mj}|}^{\pm ip|\mathbf{R}_{mj}|} e^a da\right\} \\
&= \frac{1}{(p \mid \mathbf{R}_{mj} \mid)^2}\left\{[ae^a]_{\mp ip|\mathbf{R}_{mj}|}^{\pm ip|\mathbf{R}_{mj}|} - [e^a]_{\mp ip|\mathbf{R}_{mj}|}^{\pm ip|\mathbf{R}_{mj}|}\right\} \\
&= \frac{1}{(p \mid \mathbf{R}_{mj} \mid)^2}\left\{\pm ip \mid \mathbf{R}_{mj} e^{\pm ip|\mathbf{R}_{mj}} - \left(\mp ip \mid \mathbf{R}_{mj} \mid e^{\mp ip|\mathbf{R}_{mj}|}\right)\right\} \\
&- \frac{1}{(p \mid \mathbf{R}_{mj} \mid)^2}\left\{e^{\pm ip|\mathbf{R}_{mj}|} - e^{\mp ip|\mathbf{R}_{mj}|}\right\} \\
&= \frac{1}{(p \mid \mathbf{R}_{mj} \mid)^2}\left\{\pm ip \mid \mathbf{R}_{mj} e^{\pm ip|\mathbf{R}_{mj}} \pm ip \mid \mathbf{R}_{mj} \mid e^{\mp ip|\mathbf{R}_{mj}|}\right\} \\
&- \frac{1}{(p \mid \mathbf{R}_{mj} \mid)^2}\left\{e^{\pm ip|\mathbf{R}_{mj}|} - e^{\mp ip|\mathbf{R}_{mj}|}\right\} \\
&= \mp\frac{\left[\left(e^{ip|\mathbf{R}_{mj}|} - e^{-ip|\mathbf{R}_{mj}|}\right) - ip \mid \mathbf{R}_{mj} \mid \left(e^{ip|\mathbf{R}_{mj}} + e^{-ip|\mathbf{R}_{mj}|}\right)\right]}{(p \mid \mathbf{R}_{mj} \mid)^2},
\end{aligned} \tag{4.89}$$

como resultado, o termo angular torna-se

$$\int_0^\pi sin\theta cos\theta e^{\mp ip|\mathbf{R}_{mj}|cos\theta} d\theta = \mp\frac{\left[\left(e^{ip|\mathbf{R}_{mj}|} - e^{-ip|\mathbf{R}_{mj}|}\right) - ip \mid \mathbf{R}_{mj} \mid \left(e^{ip|\mathbf{R}_{mj}} + e^{-ip|\mathbf{R}_{mj}|}\right)\right]}{(p \mid \mathbf{R}_{mj} \mid)^2}. \tag{4.90}$$

então temos

$$\begin{aligned}
I_2 &= \mp\sigma e^{\mp i\chi \boldsymbol{Q}\cdot\mathbf{R}_{mj}} \frac{v_0^2 \Omega v_F \chi}{\mathcal{N}(2\pi)^2 \mid \mathbf{R}_{mj} \mid^2}\int_0^\infty pdp \frac{(e^{ip|\mathbf{R}_{mj}|} - e^{-ip|\mathbf{R}_{mj}|} - ip \mid \mathbf{R}_{mj} \mid \left(e^{ip|\mathbf{R}_{mj}|} + e^{-ip|\mathbf{R}_{mj}|}\right)}{\varepsilon_\chi^2 - (v_F p)^2} \\
&= \mp\sigma e^{\mp i\chi \boldsymbol{Q}\cdot\mathbf{R}_{mj}} \frac{v_0^2 \Omega v_F \chi}{\mathcal{N}(2\pi)^2 \mid \mathbf{R}_{mj} \mid^2}\left(\int_0^\infty \frac{pe^{ip|\mathbf{R}_{mj}|}}{\varepsilon_\chi^2 - (v_F p)^2} dp - \int_0^\infty \frac{pe^{-ip|\mathbf{R}_{mj}|}}{\varepsilon_\chi^2 - (v_F p)^2} dp\right) \\
&\mp \sigma e^{\mp i\chi \boldsymbol{Q}\cdot\mathbf{R}_{mj}} (-i) \frac{v_0^2 \Omega v_F \chi \mid \mathbf{R}_{mj} \mid}{\mathcal{N}(2\pi)^2 \mid \mathbf{R}_{mj} \mid^2}\left(\int_0^\infty \frac{p^2 e^{ip|\mathbf{R}_{mj}|}}{\varepsilon_\chi^2 - (v_F p)^2} dp + \int_0^\infty \frac{p^2 e^{-ip|\mathbf{R}_{mj}|}}{\varepsilon_\chi^2 - (v_F p)^2} dp\right),
\end{aligned} \tag{4.91}$$

pelo método de substituição simples, onde $-p = a$ e $-dp = da$,

$$
\begin{aligned}
INT2 &= \mp\sigma e^{\mp i\chi \boldsymbol{Q}\cdot\mathbf{R}_{mj}} \frac{v_0^2\Omega v_F\chi}{\mathcal{N}\left(2\pi\right)^2 \mid \mathbf{R}_{mj} \mid^2}\left(\int_0^{\infty}\frac{pe^{ip|\mathbf{R}_{mj}|}}{\left(\varepsilon+i\eta\right)^2-\left(v_Fp\right)^2}dp-\int_0^{-\infty}\frac{ae^{ia|\mathbf{R}_{mj}|}}{\left(\varepsilon+i\eta\right)^2-\left(v_Fa\right)^2}da\right)\\
&\mp \sigma e^{\mp i\chi \boldsymbol{Q}\cdot\mathbf{R}_{mj}}\left(-i\right)\frac{v_0^2\Omega v_F\chi \mid \mathbf{R}_{mj} \mid}{\mathcal{N}\left(2\pi\right)^2 \mid \mathbf{R}_{mj} \mid^2}\left(\int_0^{\infty}\frac{p^2e^{ip|\mathbf{R}_{mj}|}}{\left(\varepsilon+i\eta\right)^2-\left(v_Fp\right)^2}dp-\int_0^{-\infty}\frac{a^2e^{ia|\mathbf{R}_{mj}|}}{\left(\varepsilon+i\eta\right)^2-\left(v_Fa\right)^2}da\right)\\
&= \mp\sigma e^{\mp i\chi \boldsymbol{Q}\cdot\mathbf{R}_{mj}} \frac{v_0^2\Omega v_F\chi}{\mathcal{N}\left(2\pi\right)^2 \mid \mathbf{R}_{mj} \mid^2}\left(\int_0^{\infty}\frac{pe^{ip|\mathbf{R}_{mj}|}}{\left(\varepsilon+i\eta\right)^2-\left(v_Fp\right)^2}dp+\int_{-\infty}^{0}\frac{ae^{ia|\mathbf{R}_{mj}|}}{\left(\varepsilon+i\eta\right)^2-\left(v_Fa\right)^2}da\right)\\
&\mp \sigma e^{\mp i\chi \boldsymbol{Q}\cdot\mathbf{R}_{mj}}\left(-i\right)\frac{v_0^2\Omega v_F\chi \mid \mathbf{R}_{mj} \mid}{\mathcal{N}\left(2\pi\right)^2 \mid \mathbf{R}_{mj} \mid^2}\left(\int_0^{\infty}\frac{p^2e^{ip|\mathbf{R}_{mj}|}}{\left(\varepsilon+i\eta\right)^2-\left(v_Fp\right)^2}dp+\int_{-\infty}^{0}\frac{a^2e^{ia|\mathbf{R}_{mj}|}}{\left(\varepsilon+i\eta\right)^2-\left(v_Fa\right)^2}da\right)\\
&= \mp\sigma e^{\mp i\chi \boldsymbol{Q}\cdot\mathbf{R}_{mj}} \frac{v_0^2\Omega v_F\chi}{\mathcal{N}\left(2\pi\right)^2 \mid \mathbf{R}_{mj} \mid^2}\left(\int_{-\infty}^{+\infty}\frac{pe^{ip|\mathbf{R}_{mj}|}}{\varepsilon_\chi^2-\left(v_Fp\right)^2}dp+\left(-i\right)\mid \mathbf{R}_{mj} \mid \int_{-\infty}^{+\infty}\frac{p^2e^{ip|\mathbf{R}_{mj}|}}{\varepsilon_\chi^2-\left(v_Fp\right)^2}dp\right),
\end{aligned}
\tag{4.92}
$$

resultando em

$$
\begin{aligned}
\Sigma_{p_z^{\bar{\sigma}}}^{\chi} &= -e^{\mp i\chi \boldsymbol{Q}\cdot\mathbf{R}_{mj}}\frac{v_0^2\Omega\varepsilon_\chi}{\left(2\pi\right)^2\mathcal{N}i \mid \mathbf{R}_{mj} \mid v_F^2}\int_{-\infty}^{\infty}dp\frac{p}{p^2-\frac{\varepsilon_\chi^2}{v_F^2}}\left(e^{ip|\mathbf{R}_{mj}|}\right)\\
&+ \sigma e^{\mp i\chi \boldsymbol{Q}\cdot\mathbf{R}_{mj}}\frac{v_0^2\Omega v_F\chi}{\mathcal{N}\left(2\pi\right)^2 v_F^2 \mid \mathbf{R}_{mj} \mid^2}\left(\mp\int\frac{pe^{ip|\mathbf{R}_{mj}|}}{p^2-\frac{\varepsilon_\chi^2}{v_F^2}}dp\mp\left(-i\right)\mid \mathbf{R}_{mj} \mid \int_{-\infty}^{+\infty}\frac{p^2e^{ip|\mathbf{R}_{mj}|}}{p^2-\frac{\varepsilon_\chi^2}{v_F^2}}dp\right).
\end{aligned}
\tag{4.93}
$$

Para resolver a integral do primeiro termo, vamos utilizar o teorema dos resíduos [51], no qual é definido por

$$
\oint_C f\left(z\right)dz=\int_{-R}^{R}f\left(x\right)dx+\oint f\left(z\right)dz, \tag{4.94}
$$

em que $z=pe^{i\theta}$ ou $z=pe^{-i\theta}$. Por simplicidade devemos escolher o contorno que resulta em zero quando $\mathbf{p}\to\infty$

$$
\begin{aligned}
\oint_C f\left(z\right)dz &= \lim_{\mathrm{R}\to\infty}\left\{\int_{-R}^{R}f\left(p\right)dp+\oint f\left(z\right)dz\right\}=2\pi i\mathrm{Res}f\left(p\right)\\
&= \int_{-\infty}^{\infty}f\left(p\right)dp=2\pi i\mathrm{Res}f\left(p\right),
\end{aligned}
\tag{4.95}
$$

em outras palavras

$$\int_{-\infty}^{\infty} dp \frac{p}{p^2 - \frac{\varepsilon_\chi^2}{v_F^2}} e^{ip|\mathbf{R}_{mj}|} = 2\pi i \text{Res} f\left(p\right). \tag{4.96}$$

Primeiro, temos que calcular os polos do integrando, que são

$$\begin{cases} p_1 & = +\frac{\varepsilon_\chi}{v_F} \\ p_2 & = -\frac{\varepsilon_\chi}{v_F} \end{cases} \tag{4.97}$$

Apenas o primeiro polo está dentro do contorno, portanto, o resíduo pode ser calculado como

$$\begin{aligned} \text{Res} f(p) &= \lim_{p \to \frac{\varepsilon_\chi}{v_F}} \left(p - \frac{\varepsilon_\chi}{v_F}\right) \frac{p}{p^2 - \frac{\varepsilon_\chi^2}{v_F^2}} e^{ip|\mathbf{R}_{mj}|} \\ &= \lim_{p \to \frac{\varepsilon_\chi}{v_F}} \left(p - \frac{\varepsilon_\chi}{v_F}\right) \frac{p}{\left(p - \frac{\varepsilon_\chi}{v_F}\right)\left(p + \frac{\varepsilon_\chi}{v_F}\right)} e^{ip|\mathbf{R}_{mj}|} \\ &= \lim_{p \to \frac{\varepsilon_\chi}{v_F}} \frac{p}{\left(p + \frac{\varepsilon_\chi}{v_F}\right)} e^{ip|\mathbf{R}_{mj}|} \\ &= \frac{\frac{\varepsilon_\chi}{v_F}}{\left(\frac{\varepsilon_\chi}{v_F} + \frac{\varepsilon_\chi}{v_F}\right)} \exp\left[i \mid \mathbf{R}_{mj} \mid \left(\frac{\varepsilon_\chi}{v_F}\right)\right] \\ &= \frac{\frac{\varepsilon_\chi}{v_F}}{2\frac{\varepsilon_\chi}{v_F}} \exp\left[i \mid \mathbf{R}_{mj} \mid \left(\frac{\varepsilon_\chi}{v_F}\right)\right] \\ &= \frac{1}{2} \exp\left[i \mid \mathbf{R}_{mj} \mid \left(\frac{\varepsilon_\chi}{v_F}\right)\right], \end{aligned} \tag{4.98}$$

retomando a Eq. (4.96), temos

$$\int_{-\infty}^{\infty} dp \frac{p}{p^2 - \frac{\varepsilon_\chi^2}{v_F^2}} e^{ip|\mathbf{R}_{mj}|} = \pi i \exp\left[i \mid \mathbf{R}_{mj} \mid \left(\frac{\varepsilon_\chi}{v_F}\right)\right]. \tag{4.99}$$

Agora, vamos resolver a segunda integral

$$\int_{-\infty}^{+\infty} \frac{p^2 e^{ip|\mathbf{R}_{mj}|}}{p^2 - \frac{\varepsilon_\chi^2}{v_F^2}} dp = 2\pi i \text{Res} f(p), \tag{4.100}$$

com os polos

$$\begin{cases} p_1 &= +\frac{\varepsilon_\chi}{v_F} \\ p_2 &= -\frac{\tilde{\varepsilon}_\chi}{v_F} \end{cases} \tag{4.101}$$

sendo assim

$$\begin{aligned} \mathrm{Res} f(p) &= \lim_{p\to\frac{\varepsilon_\chi}{v_F}} \left(p-\frac{\varepsilon_\chi}{v_F}\right) \frac{p^2}{p^2-\frac{\varepsilon_\chi^2}{v_F^2}} e^{ip|\mathbf{R}_{mj}|} \\ &= \lim_{p\to\frac{\varepsilon_\chi}{v_F}} \left(p-\frac{\varepsilon_\chi}{v_F}\right) \frac{p^2}{\left(p-\frac{\varepsilon_\chi}{v_F}\right)\left(p+\frac{\varepsilon_\chi}{v_F}\right)} e^{ip|\mathbf{R}_{mj}|} \\ &= \lim_{p\to\frac{\varepsilon_\chi}{v_F}} \frac{p^2}{\left(p+\frac{\varepsilon_\chi}{v_F}\right)} e^{ip|\mathbf{R}_{mj}|} \\ &= \frac{\left(\frac{\varepsilon_\chi}{v_F}\right)^2}{\left(\frac{\varepsilon_\chi}{v_F}+\frac{\varepsilon_\chi}{v_F}\right)} \exp\left[i \mid \mathbf{R}_{mj} \mid \left(\frac{\varepsilon_\chi}{v_F}\right)\right] \\ &= \frac{\left(\frac{\varepsilon_\chi}{v_F}\right)^2}{2\frac{\varepsilon_\chi}{v_F}} \exp\left[i \mid \mathbf{R}_{mj} \mid \left(\frac{\varepsilon_\chi}{v_F}\right)\right] \\ &= \frac{\varepsilon_\chi}{2v_F} \exp\left[i \mid \mathbf{R}_{mj} \mid \left(\frac{\varepsilon_\chi}{v_F}\right)\right], \end{aligned} \tag{4.102}$$

retomando para Eq. (4.100), temos

$$\int_{-\infty}^{+\infty} \frac{p^2 e^{ip|\mathbf{R}_{mj}|}}{p^2-\frac{(\varepsilon+i\eta)^2}{v_F^2}} dp = \pi i \frac{\varepsilon_\chi}{v_F} \exp\left[i \mid \mathbf{R}_{mj} \mid \left(\frac{\varepsilon_\chi}{v_F}\right)\right]. \tag{4.103}$$

Resultando a auto-energia em

$$\begin{aligned} \Sigma_\sigma^\chi &= -\frac{v_0^2\Omega}{4\pi\frac{\Omega}{2\pi^2 v_F^3}\frac{D^3}{3} \mid \mathbf{R}_{mj} \mid v_F^2} \exp\left[i \mid \mathbf{R}_{mj} \mid \left(\frac{\varepsilon_\chi}{v_F}\right) \mp i\chi \boldsymbol{Q}\cdot\mathbf{R}_{mj}\right] \left\{\varepsilon_\chi \pm \sigma\varepsilon_\chi\chi \pm i\sigma\frac{v_F\chi}{\mid \mathbf{R}_{mj} \mid}\right\} \\ &= -\frac{3v_F\pi v_0^2}{2D^3 \mid \mathbf{R}_{mj} \mid} \exp\left[i \mid \mathbf{R}_{mj} \mid \left(\frac{\varepsilon_\chi}{v_F}\right) \mp i\chi \boldsymbol{Q}\cdot\mathbf{R}_{mj}\right] \left\{\varepsilon_\chi \pm \sigma\varepsilon_\chi\chi \pm i\sigma\frac{v_F\chi}{\mid \mathbf{R}_{mj} \mid}\right\}, \end{aligned} \tag{4.104}$$

onde utilizamos $\mathcal{N} = \sum_{\mathbf{p}} \to \frac{4\pi\Omega}{(2\pi)^3}\int_0^{p_D} p^2 dp$ e $D = v_F p_D$.

4.5 Auto-energia para $\mathbf{R} = 0$

Para $R = 0$, a auto-energia é definida como

$$\Sigma^{\chi}(0) = \frac{v_0^2}{\mathcal{N}} \sum_{\overrightarrow{p}} \frac{\tilde{\varepsilon}_{\chi}}{\tilde{\varepsilon}_{\chi}^2 + (v_F p)^2} + \sigma \frac{v_0^2}{\mathcal{N}} \sum_{\overrightarrow{p}} \frac{v_F \chi p_z}{\tilde{\varepsilon}_{\chi}^2 - (v_F p)^2}. \tag{4.105}$$

Calculando o primeiro termo, temos

$$\begin{aligned}
I_1 &= \frac{v_0^2}{\mathcal{N}} \sum_{\mathbf{p}} \frac{(\varepsilon_{\chi} + i\eta)}{(\varepsilon_{\chi} + i\eta)^2 - (v_F p)^2} \\
&= \frac{v_0^2}{\mathcal{N}} \sum_{\mathbf{p}} \frac{\varepsilon_{\chi}}{\varepsilon_{\chi}^2 + i\eta sgn(\varepsilon_{\chi}) - \eta^2 - (v_F p)^2} \\
&= \frac{v_0^2}{\mathcal{N}} \sum_{\mathbf{p}} \frac{\varepsilon_{\chi}}{\left(\varepsilon_{\chi}^2 - v_F^2 p^2\right) + i\eta sgn(\varepsilon_{\chi})} \left[\frac{\left(\varepsilon_{\chi}^2 - v_F^2 p^2\right) - i\eta sgn(\varepsilon_{\chi})}{\left(\varepsilon_{\chi}^2 - v_F^2 p^2\right) - i\eta sgn(\varepsilon_{\chi})} \right] \\
&= \frac{v_0^2}{\mathcal{N}} \sum_{\mathbf{p}} \frac{\varepsilon_{\chi}\left(\varepsilon_{\chi}^2 - v_F^2 p^2 - i\eta sgn(\varepsilon_{\chi})\right)}{\left(\varepsilon_{\chi}^2 - v_F^2 p^2\right)^2 + \eta^2} \\
&= \frac{v_0^2}{\mathcal{N}} \sum_{\mathbf{p}} \left[\frac{\varepsilon_{\chi}\left(\varepsilon_{\chi}^2 - v_F^2 p^2\right)}{\left(\varepsilon_{\chi}^2 - v_F^2 p^2\right)^2 + \eta^2} - i \frac{\varepsilon_{\chi}\eta sgn(\varepsilon_{\chi})}{\left(\varepsilon_{\chi}^2 - v_F^2 p^2\right)^2 + \eta^2} \right] \\
&= \frac{v_0^2}{\mathcal{N}} \sum_{\mathbf{p}} \left[\frac{\varepsilon_{\chi}}{\left(\varepsilon_{\chi}^2 - v_F^2 p^2\right)} - i \frac{\varepsilon_{\chi}\eta sgn(\varepsilon_{\chi})}{\left(\varepsilon_{\chi}^2 - v_F^2 p^2\right)^2 + \eta^2} \right] \\
&= \mathcal{R}_{R=0}^{WSM} + i\Gamma_{R=0}^{WSM}.
\end{aligned} \tag{4.106}$$

Calculando a parte real com $\mathcal{N} = \sum_{\mathbf{p}} \to \frac{4\pi\Omega}{(2\pi)^3} \int_0^{p_D} p^2 dp$, temos

$$\begin{aligned}
\mathcal{R}_{R=0}^{WSM} &= \frac{v_0^2}{\mathcal{N}}\sum_{\mathbf{p}}\frac{\varepsilon_\chi\left(\varepsilon_\chi^2 - v_F^2p^2\right)}{\left(\varepsilon_\chi^2 - v_F^2p^2\right)^2+\eta^2} \\
&= \frac{v_0^2}{\mathcal{N}}\frac{\Omega}{2\pi^2}\int_0^{p_D} p^2dp\frac{\varepsilon_\chi}{\left(\varepsilon_\chi^2 - v_F^2p^2\right)} \\
&= \frac{v_0^2}{\mathcal{N}}\frac{\Omega}{2\pi^2}\int_0^{p_D} p^2dp\frac{\varepsilon_\chi}{\left(\varepsilon_\chi^2 - v_F^2p^2\right)} \\
&= \frac{v_0^2\varepsilon_\chi}{\mathcal{N}}\frac{\Omega}{2\pi^2}\int_0^{p_D} dp\frac{p^2}{\left(\varepsilon_\chi^2 - v_F^2p^2\right)} \\
&= \frac{v_0^2\varepsilon_\chi}{\mathcal{N}}\frac{\Omega}{2\pi^2}\int_0^{p_D} dp\frac{p^2}{v_F^2\left(\frac{\varepsilon_\chi^2}{v_F^2} - p^2\right)} \\
&= \frac{v_0^2\varepsilon_\chi}{\mathcal{N}v_F^2}\frac{\Omega}{2\pi^2}\int_0^{p_D} dp\frac{p^2}{\left(\frac{\varepsilon_\chi^2}{v_F^2} - p^2\right)}. \qquad (4.107)
\end{aligned}$$

A integral resulta em

$$\begin{aligned}
\int_0^{p_D} dp\frac{p^2}{\left(\frac{\varepsilon_\chi^2}{v_F^2} - p^2\right)} &= \left[\frac{1}{2}\frac{\varepsilon_\chi}{v_F}\ln\left(\frac{\left|p+\frac{\varepsilon_\chi}{v_F}\right|}{\left|p-\frac{\varepsilon_\chi}{v_F}\right|}\right) - p\right]_0^{p_D} \\
&= \left(\frac{1}{2}\frac{\varepsilon_\chi}{v_F}\ln\left(\frac{\left|p_D+\frac{\varepsilon_\chi}{v_F}\right|}{\left|p_D-\frac{\varepsilon_\chi}{v_F}\right|}\right) - p_D\right) - \left(\frac{1}{2}\frac{\varepsilon_\chi}{v_F}\ln\left(\frac{\left|0+\frac{\varepsilon_\chi}{v_F}\right|}{\left|0-\frac{\varepsilon_\chi}{v_F}\right|}\right) - 0\right) \\
&= \left(\frac{1}{2}\frac{\varepsilon_\chi}{v_F}\ln\left(\frac{\left|p_D+\frac{\varepsilon_\chi}{v_F}\right|}{\left|p_D-\frac{\varepsilon_\chi}{v_F}\right|}\right) - p_D\right) - \left(\frac{1}{2}\frac{\varepsilon_\chi}{v_F}\ln(1)\right) \\
&= \left(\frac{1}{2}\frac{\varepsilon_\chi}{v_F}\ln\left(\frac{\left|p_D+\frac{\varepsilon_\chi}{v_F}\right|v_D}{\left|p_D-\frac{\varepsilon_\chi}{v_F}\right|v_F}\right) - \frac{v_Fp_D}{v_F}\right) \\
&= \left(\frac{1}{2}\frac{\varepsilon_\chi}{v_F}\ln\left(\frac{|D+\varepsilon_\chi|}{|D-\varepsilon_\chi|}\right) - \frac{D}{v_F}\right), \qquad (4.108)
\end{aligned}$$

onde $D = v_Fp_D$, portanto

$$\begin{aligned}\mathcal{R}_{R=0}^{WSM} &= \frac{v_0^2\varepsilon_\chi}{v_F^2\frac{\Omega D^3}{6\pi^2 v_F^3}v_F^3}\frac{\Omega}{2\pi^2}\left[\frac{1}{2}\frac{\varepsilon_\chi}{v_F}\ln\left(\frac{|D+\varepsilon_\chi|}{|D-\varepsilon_\chi|}\right)-\frac{D}{v_F}\right]\\ &= \frac{3v_0^2\varepsilon_\chi}{D^3}\left[\frac{1}{2}\varepsilon_\chi\ln\left(\frac{|D+\varepsilon_\chi|}{|D-\varepsilon_\chi|}\right)-D\right]. \end{aligned} \tag{4.109}$$

Calculando a parte imaginária

$$\begin{aligned}\Gamma_{R=0}^{WSM} &= -\frac{v_0^2}{\mathcal{N}}\sum_{\mathbf{p}}\frac{\varepsilon_\chi\eta sgn\left(\varepsilon_\chi\right)}{\left(\varepsilon_\chi^2-v_F^2p^2\right)^2+\eta^2}\\ &= -\frac{|\varepsilon_\chi|\,v_0^2}{\mathcal{N}}\sum_{\mathbf{p}}\frac{\eta}{\left(\varepsilon_\chi^2-v_F^2p^2\right)^2+\eta^2}\\ &= -\frac{|\varepsilon_\chi|\,v_0^2}{\mathcal{N}}\frac{\Omega}{2\pi^2}\int_0^{p_D}p^2dp\frac{\eta}{\left(\varepsilon_\chi^2-v_F^2p^2\right)^2+\eta^2}\\ &= -\frac{|\varepsilon_\chi|\,v_0^2}{\mathcal{N}}\frac{\Omega}{2\pi^2}\int_0^{D}\left(\frac{\varepsilon_p^2}{v_F^2}\right)\left(\frac{d\varepsilon_p}{v_F}\right)\frac{\eta}{\left(\varepsilon_\chi^2-\varepsilon_p^2\right)^2+\eta^2}\\ &= -\frac{|\varepsilon_\chi|\,v_0^2}{\mathcal{N}}\frac{\Omega}{2\pi^2v_F^3}\int_0^{D}\varepsilon_p^2d\varepsilon_p\frac{\eta}{\left(\varepsilon_\chi^2-\varepsilon_p^2\right)^2+\eta^2}\\ &= -\frac{2\,|\varepsilon_\chi|\,v_0^2}{\mathcal{N}}\frac{\Omega}{2\pi^2v_F^3}\int_0^{D}\varepsilon_p^2d\varepsilon_p\left[\pi\delta\left(\varepsilon_\chi^2-\varepsilon_p^2\right)\right]\\ &= -\pi\frac{|\varepsilon_\chi|\,v_0^2}{\mathcal{N}}\frac{\Omega}{2\pi^2v_F^3}\int_0^{D}\varepsilon_p^2d\varepsilon_p\frac{1}{2\,|\varepsilon_\chi|}\left[\delta\left(\varepsilon_\chi-\varepsilon_p\right)+\delta\left(\varepsilon_\chi+\varepsilon_p\right)\right]\\ &= -\frac{\pi}{\mathcal{N}}\frac{\Omega v_0^2}{4\pi^2v_F^3}\int_0^{D}\varepsilon_p^2d\varepsilon_p\left[\delta\left(\varepsilon_\chi-\varepsilon_p\right)+\delta\left(\varepsilon_\chi+\varepsilon_p\right)\right]\\ &= -\frac{3\pi v_0^2}{2D^3}\varepsilon_\chi^2, \end{aligned} \tag{4.110}$$

onde utilizamos as seguintes propriedades

$$\delta\left(\varepsilon_\chi^2-\varepsilon_p^2\right)=\frac{\eta}{\left(\varepsilon_\chi^2-\varepsilon_p^2\right)^2+\eta^2}, \tag{4.111}$$

$$\delta\left(\varepsilon_\chi^2-\varepsilon_p^2\right)=\frac{1}{2\,|\varepsilon_\chi|}\left[\delta\left(\varepsilon_\chi-\varepsilon_p\right)+\delta\left(\varepsilon_\chi+\varepsilon_p\right)\right]. \tag{4.112}$$

No segundo termo da Eq. (4.105), nos deparamos com integrais do tipo $\int_0^\pi d\theta sin\theta cos\theta = 0$, portanto, resulta em 0. Sendo assim, a auto-energia para $R=0$ é

$$\Sigma^{\chi}(0) = \frac{3v_0^2\varepsilon_\chi}{D^3}\left[\frac{1}{2}\varepsilon_\chi \ln\left(\frac{|D+\varepsilon_\chi|}{|D-\varepsilon_\chi|}\right) - D\right] - i\frac{3\pi v_0^2}{2D^3}\varepsilon_\chi^2. \tag{4.113}$$

Capítulo 5

Resultados e discussão

Com base nas equações calculadas no capítulo anterior, o objetivo de estudo é:

- Explorar os estados de impurezas atomicamente frustrados em metais de Weyl. Investigar o efeito da quebra de simetria de inversão na estrutura dos estados moleculares das impurezas nesse sistema. Os resultados foram publicados no Physical Review B 102, 075120 (2020) [26].

5.1 Estados de impurezas atomicamente frustrados em metais de Weyl

Os parâmetros utilizados no estudo do sistema metal de Weyl são: $|\mathbf{R}_{12}| = 2$nm, $\varepsilon_d = -0.07D$, $v_0 = -0.14D$, $U = 0.14D$, $v_F \approx 3$eVÅ e $D \approx 0.2eV$. Consideramos que as impurezas estão enterradas em uma distância de 1nm abaixo da superfície do material de Dirac-Weyl e estão localizadas nos pontos $\mathbf{R}_1 = (0, -1, 0)$nm e $\mathbf{R}_2 = (0, 1, 0)$nm, como apresentado na Fig. 4.1.

A Fig. 5.1 ilustra a evolução do perfil da LDOS espacial na superfície do hospedeiro, obtida pela Eq. (4.77), e que pode ser sondada por uma ponta de STM. O aumento do parâmetro Q_0 descreve o grau da quebra de simetria de inversão.

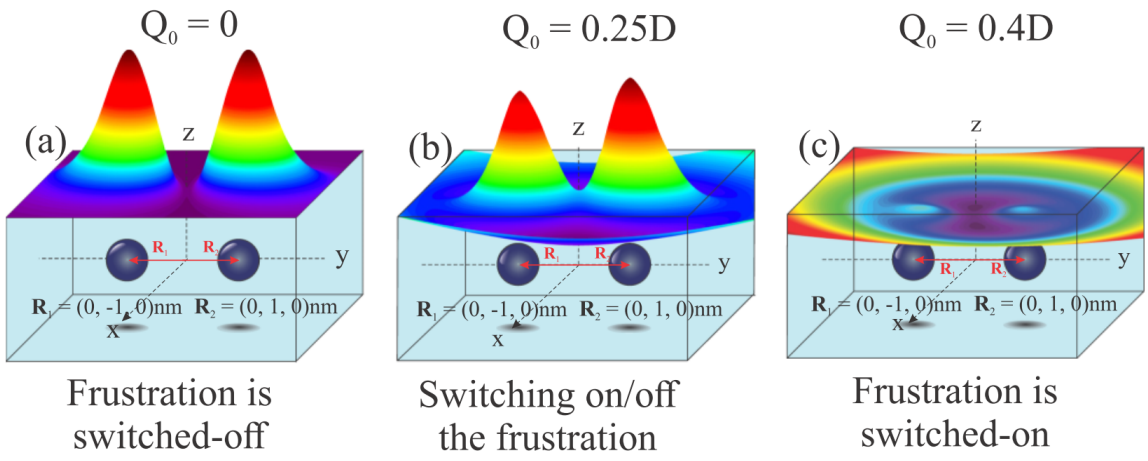

Figura 5.1: Perfil espacial da LDOS, correspondendo ao estado antiligante do par de impurezas, inseridas em um semimetal de Dirac (a) $Q_0 = 0$. (b) Metal de Weyl $Q_0 = 0.25D$. (c) Metal de Weyl $Q_0 = 0.4D$ descrevendo um estado molecular atomicamente frustrado.

Na Fig. 5.1(a), temos o caso do semimetal de Dirac com nós de Weyl degenerados, correspondente ao valor de $Q_0 = 0$. Os orbitais moleculares do tipo ligante e antiligante são formados, sendo mostrado o perfil correspondente ao último, com máximos da LDOS centrados nos pontos onde se localizam as impurezas. Ressaltamos que devido às propriedades da estrutura de bandas do hospedeiro de Dirac, o estado antiligante possui menor energia em relação ao estado ligante, conforme demonstrado na Ref. [7]. O aumento do parâmetro Q_0 faz com que os picos da LDOS sofram um alargamento. Ainda assim, se os valores de Q_0 forem moderados, os perfis da LDOS permanecem qualitativamente os mesmos de $Q_0 = 0$ e ainda podem ser descritos em termos da formação de um estado molecular antiligante, conforme ilustrado na Fig. 5.1(b). No entanto, se o valor do parâmetro Q_0 torna-se suficientemente grande, o perfil da LDOS muda drasticamente, diminuindo na região ao redor das impurezas e correspondendo a uma configuração centro-simétrica distorcida caracterizando um estado atômico frustrado, como mostrado na Fig. 5.1(c).

Para melhor compreensão sobre os mecanismos subjacentes à sua formação, analisamos separadamente diferentes contribuições para a LDOS induzidas pelas impurezas, conforme apresentado nas Figs. 5.2 a 5.4.

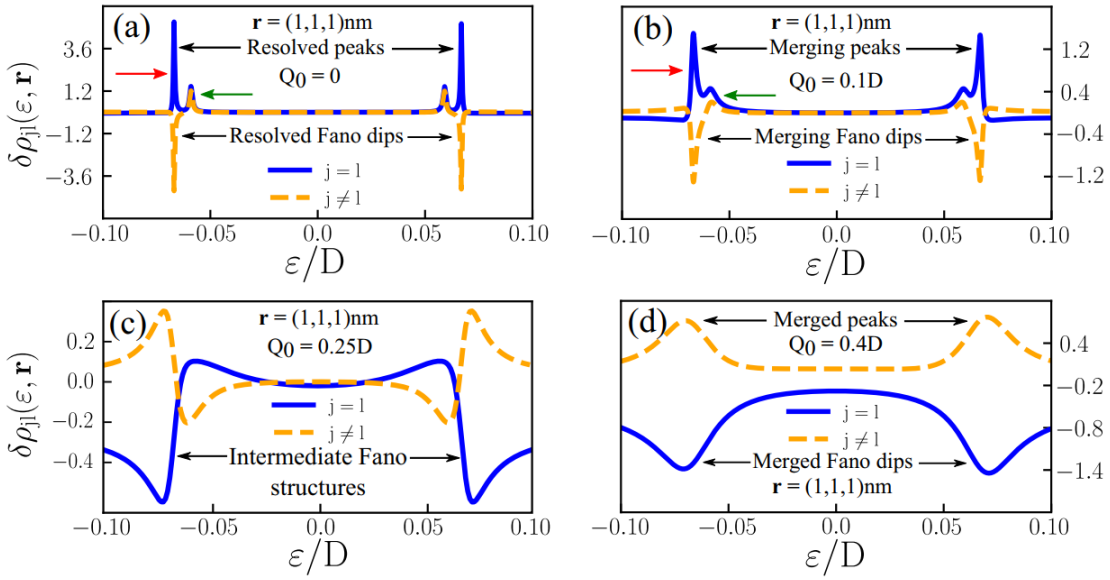

Figura 5.2: Contribuições induzidas por impurezas para a densidade de estados $\delta\rho_{jl}$ da Eq. (6.54) em função da energia. (a) Caso semimetal de Dirac, $Q_0 = 0$. (b) Metal de Weyl com valor pequeno de $Q_0 = 0.1D$. (c) Metal de Weyl com valor moderado de $Q_0 = 0.25D$. (d) Metal de Weyl com valor grande de $Q_0 = 0.4D$ [26].

A Fig. 5.2 mostra os gráficos de $\delta\rho_{jl}$ da Eq. (6.54) em função da energia para uma determinada posição da ponta de STM $\mathbf{r} = (1, 1, 1)$nm. Ambas as contribuições diretas $(j = l)$ e cruzadas $(j \neq l)$ são apresentadas. Na Fig. 5.2(a), no caso Dirac $(Q_0 = 0)$, nota-se a presença de quatro picos em $\delta\rho_{jj}$, correspondendo às bandas de Hubbard bem resolvidas [ver Sec. 2.2], as quais descrevem a formação de orbitais moleculares ligantes e antiligantes em torno de $\varepsilon_d < 0$ e $\varepsilon_d + U > 0$, respectivamente. Para os parâmetros considerados, o pico de menor energia corresponde ao estado antiligante (indicado pela seta vermelha) e o próximo pico ao estado molecular ligante (indicado pela seta verde) [7]. Com o aumento de Q_0 as ressonâncias e antirressonâncias de Fano são alargadas [Fig. 5.2(b), $Q_0 = 0.1D$]. Em um determinado valor, os picos correspondentes aos estados ligante e antiligante se fundem, dando origem às formas intermediárias de linhas de Fano [Fig. 5.2(c), $Q_0 = 0.25D$]. O aumento adicional de Q_0 leva à formação de um platô na densidade de estados em torno de $\varepsilon = 0$, flanqueado por um par de picos $(j \neq l)$ e vales $(j = l)$ fundidos [Fig. 5.2(d), $Q_0 = 0.4D$]. A presença de apenas duas bandas de Hubbard resolvidas é típica para um par de impurezas não correlacionadas, isto é, de impurezas atômicas isoladas [ver Sec. 2.1]. No entanto, no presente caso, as amplitudes $\delta\rho_{jl} \neq 0$ para $j \neq l$, dizem que a ligação molecular ainda persiste, no que chamamos de estado molecular atomicamente frustrado.

Nessa configuração, os papeis dos canais de interferência Fano construtivos e destrutivos entre $\delta\rho_{jj}$ e $\delta\rho_{jl}$ se invertem em relação aos observados no semimetal de Dirac, como pode ser visto claramente na comparação entre as Figs. 5.2(d) e 5.2(a).

Portanto, nesse cenário, o comportamento de uma molécula diatômica imita localmente ($\delta\rho_{jj}$) um par de átomos não correlacionados. Sua caracterização consiste em uma antirressonância Fano em $\delta\rho_{jj}$ em torno das bandas de Hubbard em $\varepsilon_d < 0$ e $\varepsilon_d + U > 0$. Entretanto, uma correlação finita entre as impurezas ($\delta\rho_{jl} \neq 0$ com $j \neq l$) surge como em uma molécula, sendo identificada por dois picos de Hubbard. Sendo assim, como o par de átomos permanece correlacionado através do hospedeiro com $\delta\rho_{jl}$ finito, embora apresente apenas duas estruturas de Hubbard como um átomo não correlacionado, então a esse estado chamamos de estado molecular atomicamente frustrado.

O principal mecanismo responsável pelo estado proposto baseia-se nas oscilações do tipo Friedel [55], que de acordo com trabalhos anteriores de alguns de nós [7, 27], podem ser moduladas pela correlação de Coulomb nas impurezas, sendo capaz de favorecer ligações moleculares em semimetais de Dirac-Weyl. Portanto, no regime em que o metal de Weyl apresenta a fase atomicamente frustrada, revelamos o importante papel das oscilações de Friedel.

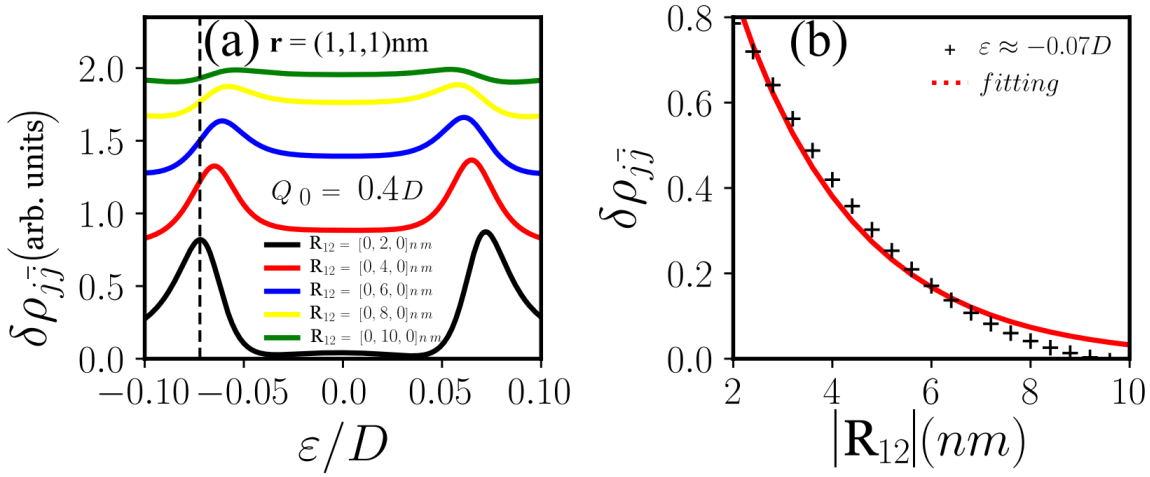

Figura 5.3: (a) LDOS induzida para $\delta\rho_{j\bar{j}}$ ($j = 1, 2$ e $\bar{j} = 2, 1$) para $Q_0 = 0.4D$ com a ponta de STM em r $= (1, 1, 1)$nm para vários valores de distância $|\mathbf{R}_{12}|$ entre as impurezas . (b) Amplitude de $\delta\rho_{j\bar{j}}$ avaliada no corte tracejado preto $\varepsilon \approx -0.07D$ marcado no painel em função de $|\mathbf{R}_{12}|$, que apresenta um decaimento do tipo exponencial (pontos cruzados em preto). Em particular, é ajustado por $\delta\rho_{j\bar{j}}(\varepsilon \approx -0,07D) = 1.96\exp(-0.41|\mathbf{R}_{12}|)$ (linha vermelha) [26].

Para entender o comportamento do estado atômico frustrado ao aumentar $|\mathbf{R}_{12}|$ descrito por $\delta\rho_{jl}$, na Fig. 5.3(a) analisamos tal quantidade para $Q_0 = 0.4D$ e uma ponta de STM em r $= (1,1,1)$nm como função da energia. Podemos perceber que o par de bandas de Hubbard do estado atômico frustrado se torna mais largo à medida que aumentamos a separação entre as impurezas, de forma que $\delta\rho_{jl}$ se aproxima de um perfil inteiramente plano, o que corresponde ao caso dos átomos desacoplados. Assim, fixando a energia, por exemplo, em $\varepsilon \approx -0,07D$ (linha vertical tracejada preta), é possível estimar a rapidez com que $\delta\rho_{jl}$ desaparece. A Fig. 5.3(b) apresenta o decaimento que obedece a um comportamento do tipo exponencial (pontos cruzados em preto), que é ajustado por $\delta\rho_{j\bar{j}}(\varepsilon \approx -0,07D) = 1.96\exp(-0.41|\mathbf{R}_{12}|)$ onde $j = 1,2$ e $\bar{j} = 2,1$. Observe que para $|\mathbf{R}_{12}| = 10$nm, a ligação molecular do estado atômico frustrado é praticamente dissociada.

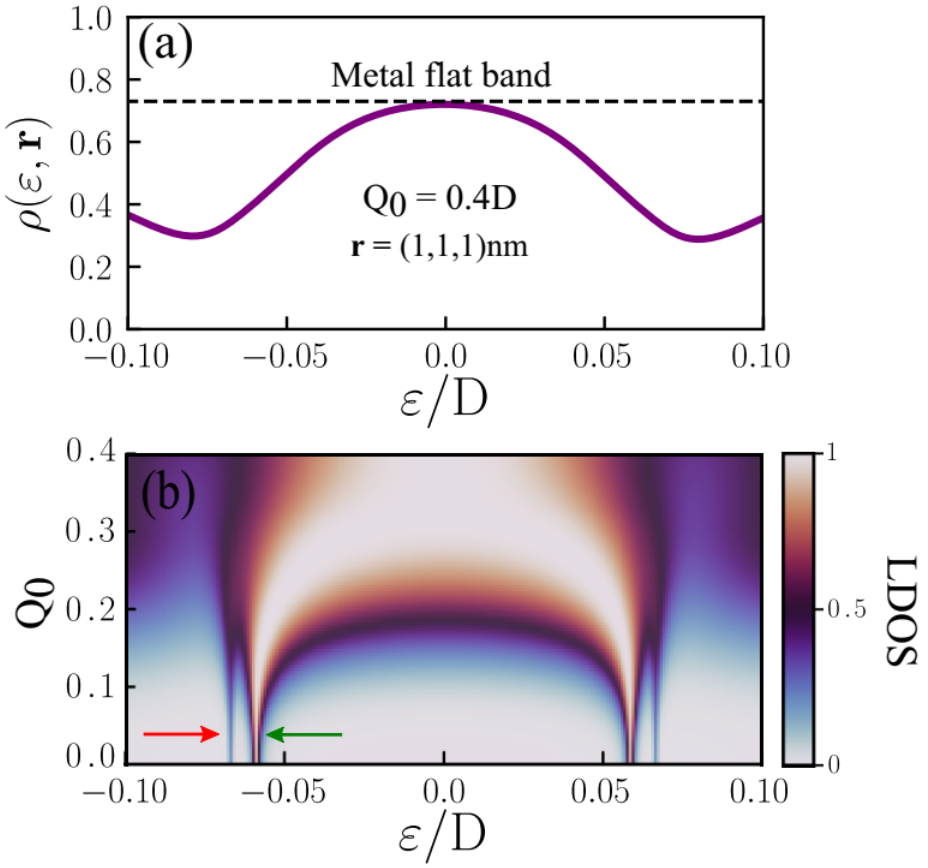

Figura 5.4: (a) A LDOS do sistema constituído por duas impurezas enterradas em um hospedeiro metálico de Weyl com $Q_0 = 0.4D$, correspondendo ao regime de formação de um estado atômico frustrado. A posição da ponta de STM é fixada em r $= (1,1,1)$nm. (b) Diagrama de fases, mostrando a LDOS em função da energia ε e do parâmetro Q_0 [26].

A Figura 5.4(a) mostra que a LDOS total tem um máximo muito amplo em $\varepsilon = 0$ e um par de vales em torno de ε_d e $\varepsilon_d + U$. O surgimento de uma LDOS plana nas proximidades de $\varepsilon = 0$ (a energia de Fermi) é característico do regime metálico do hospedeiro. Este é o resultado direto do fechamento do *pseudogap* em semimetais de Weyl com valores grandes de Q_0, para o qual a DOS do hospedeiro é alargada na energia de Fermi. Sendo assim, leva ao aumento de estados no nível de Fermi, exatamente quando a simetria de inversão é altamente quebrada, o que leva o sistema ao regime metálico de Weyl. Isso vem do aumento da separação dos cones de Dirac obedecendo aos deslocamentos azul e vermelho no eixo de energia [ver Fig. 4.1(c) do esboço do sistema], resultando em um fechamento do *pseudogap* aumentando a quantidade de estados no nível de Fermi. Portanto, isso dá origem ao platô do tipo metálico na LDOS em torno de $\varepsilon = 0$.

A evolução dos estados moleculares ligante e antiligante em um estado atômico frustrado é ilustrado pela Fig. 5.4(b), onde um diagrama de fase mostra a LDOS total em função da energia ε e do parâmetro Q_0. Com o aumento de Q_0, os picos estreitos característicos das quatro bandas de Hubbard bem resolvidas se alargam e finalmente se fundem, produzindo o perfil característico apresentado na Fig. 5.4(a).

Capítulo 6

Hamiltoniano do Grafeno bicamada torcido

Neste estudo, consideramos o grafeno bicamada torcido com padrão hexagonal de super-rede de Moiré para baixos valores de ângulo θ, como apresentado na Fig. 6.1, com duas impurezas acopladas. Analisamos a formação de estados moleculares e o comportamento dos mesmos mediante a uma voltagem externa no sistema TBG, induzindo assim, uma quebra de simetria de inversão.

Portanto, neste capítulo serão apresentados, o Hamiltoniano dos sistemas, os cálculos das funções de Green via método da equação de movimento e os cálculos das funções de Green das impurezas, onde utilizamos a aproximação de Hubbard I.

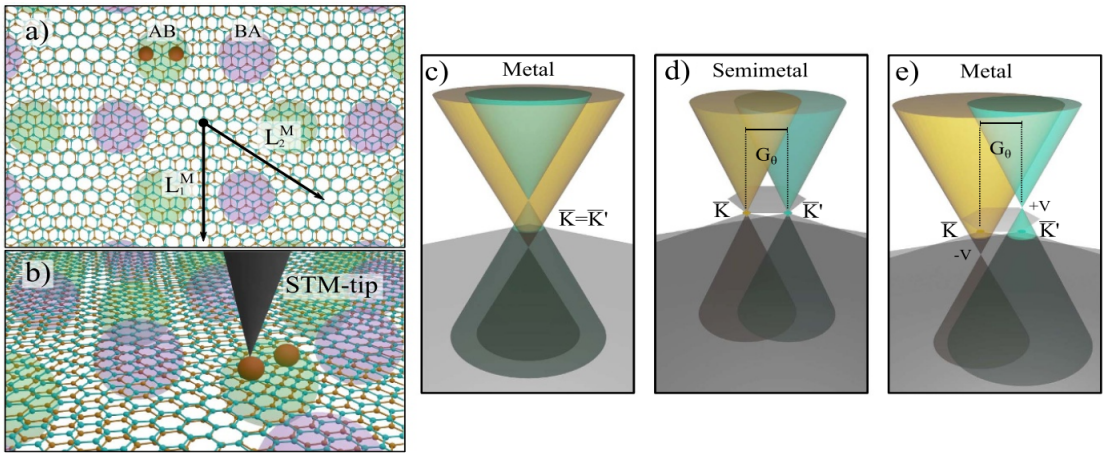

Figura 6.1: Painel (a): vista superior do sistema TBG e seu padrão hexagonal de super-rede de Moiré para pequenos ângulos de torção θ. Os vetores de base são $\mathbf{L}_1^{\mathrm{M}}$ e $\mathbf{L}_2^{\mathrm{M}}$. As regiões de empilhamento AB (verde) e BA (roxo) representam os super-átomos de Moiré e a molécula diatômica é esboçada pelo par de esferas vermelhas, acoplando-se ao sítio AB. Painel (b): perspectiva lateral do painel (a) com uma ponta STM acima de um átomo do dímero. Painel (c): estrutura de bandas para o sistema não torcido com empilhamento AA, onde os cones de Dirac coincidentes nos cantos de vale $\overline{\mathbf{K}} = \overline{\mathbf{K}'}$ surgem das zonas de Brillouin superior e inferior das monocamadas, respectivamente. Esses pontos de Dirac aparecem deslocados em energia, devido à simetria de inversão quebrada na fase metálica [28], em analogia com o metal de Weyl [26]. Painel (d): a torção restaura o caráter semimetálico do sistema, mas agora separa os pontos de Dirac com $\overline{\mathbf{K}} \neq \overline{\mathbf{K}'}$ no espaço dos momentos por $G_\theta = \frac{8\pi \sin\frac{\theta}{2}}{3a}$, onde a é o parâmetro de rede da monocamada de grafeno. Painel (e): voltagens externas ligadas às monocamadas superior (+V) e inferior (−V) induzem a quebra da simetria de inversão com caráter metálico [26, 44].

6.1 Hamiltoniano do sistema

O Hamiltoniano efetivo para o grafeno bicamada torcido (TBG) é definido por

$$H_0 = \sum_{\mathbf{k}\xi\sigma} \psi^\dagger_{\mathbf{k}\xi\sigma} H_{TBG}(\mathbf{k} + \mathbf{K}_\xi)\psi_{\mathbf{k}\xi\sigma}, \tag{6.1}$$

em que $\mathbf{k} = (k_x, k_y)$ é o vetor de onda para duas dimensões, $\xi = \pm 1$ é o índice de vale e spin $\sigma = \uparrow, \downarrow$. Temos que

$$\psi^{\dagger}_{\mathbf{k}\xi\sigma} \;=\; (\; \psi^{\dagger}_{AB\mathbf{k}\xi\sigma} \quad \psi^{\dagger}_{BA\mathbf{k}\xi\sigma} \;) \tag{6.2}$$

e

$$\psi_{\mathbf{k}\xi\sigma} \;=\; \begin{pmatrix} \psi_{AB\mathbf{k}\xi\sigma} \\ \psi_{BA\mathbf{k}\xi\sigma} \end{pmatrix}, \tag{6.3}$$

são os *spinores* e os índices AB e BA são os sítios da super-rede de Moiré. O Hamiltoniano do TBG Hamiltoniano é definido como

$$H_{TBG}(\mathbf{k}+\mathbf{K}_{\xi}) \;=\; \hbar\tilde{v}_F\boldsymbol{\sigma}_{\xi}\cdot\mathbf{k} + \xi\sigma_0 V = \hbar\tilde{v}_F(\xi\sigma_x,\sigma_y)\cdot\mathbf{k} + \xi\sigma_0 V, \tag{6.4}$$

em que

$$\tilde{v}_F \;=\; \frac{v_F\left(\hbar^2 v_F^2 G^2 - 3w_{AB}^2\right)}{3w_{AA}^2 + 3w_{AB}^2 + \hbar^2 v_F^2 G^2} \tag{6.5}$$

é a velocidade de Fermi renormalizada devido à torção entre as camadas de grafeno e seus acoplamentos w_{AA} e w_{AB}, $G = \frac{8\pi\sin\frac{\theta}{2}}{3a}$ a distância no espaço dos momentos entre os pontos de Dirac com o ângulo de desalinhamento θ entre as monocamadas de grafeno, a é o parâmetro de rede da monocamada de grafeno, w_{AB} e w_{AA} são os termos de *hopping* dos sítios AB e AA entre as camadas de grafeno, V é a tensão externa aplicada no sistema que define a separação de energia entre os nós de Dirac, semelhante ao caso do metal de Weyl, e σ_0 e $\boldsymbol{\sigma} = \sigma_x\hat{i} + \sigma_y\hat{j}$ são as matrizes identidade e de Pauli, respectivamente. A matriz do Hamiltoniano é

$$H_{TBG}(\mathbf{k}+\mathbf{K}_{\xi}) \;= \begin{pmatrix} \xi V & \hbar\tilde{v}_F(\xi k_x - ik_y) \\ \hbar\tilde{v}_F(\xi k_x + ik_y) & \xi V \end{pmatrix} \quad . \tag{6.6}$$

Aplicando os *spinores* no Hamiltoniano, temos

$$\begin{aligned} H_0 &= \sum_{\mathbf{k}\xi\sigma} \psi^{\dagger}_{\mathbf{k}\xi\sigma} \begin{pmatrix} \xi V & \hbar\tilde{v}_F(\xi k_x - ik_y) \\ \hbar\tilde{v}_F(\xi k_x + ik_y) & \xi V \end{pmatrix} \psi_{\mathbf{k}\xi\sigma} \\ &= \sum_{\mathbf{k}\xi\sigma} \begin{pmatrix} C_1 & C_2 \end{pmatrix} \psi_{\mathbf{k}\xi\sigma}, \end{aligned} \tag{6.7}$$

em que

$$C_1 = \xi V \psi^{\dagger}_{AB\mathbf{k}\xi\sigma} + \hbar\tilde{v}_F(\xi k_x + ik_y)\psi^{\dagger}_{BA\mathbf{k}\xi\sigma}, \tag{6.8}$$

$$C_2 = \hbar\tilde{v}_F(\xi k_x - ik_y)\psi^{\dagger}_{AB\mathbf{k}\xi\sigma} + \xi V \psi^{\dagger}_{BA\mathbf{k}\xi\sigma}, \tag{6.9}$$

sendo assim,

$$\begin{aligned} H_0 &= \sum_{\mathbf{k}\xi\sigma} (C_1\psi_{AB\mathbf{k}\xi\sigma} + C_2\psi_{BA\mathbf{k}\xi\sigma}) \\ &= \sum_{\mathbf{k}\xi\sigma} [\xi V \psi^{\dagger}_{AB\mathbf{k}\xi\sigma}\psi_{AB\mathbf{k}\xi\sigma} + \hbar\tilde{v}_F(\xi k_x + ik_y)\psi^{\dagger}_{BA\mathbf{k}\xi\sigma}\psi_{AB\mathbf{k}\xi\sigma}] \\ &+ \sum_{\mathbf{k}\xi\sigma} [\hbar\tilde{v}_F(\xi k_x - ik_y)\psi^{\dagger}_{AB\mathbf{k}\xi\sigma}\psi_{BA\mathbf{k}\xi\sigma} + \xi V \psi^{\dagger}_{BA\mathbf{k}\xi\sigma}\psi_{BA\mathbf{k}\xi\sigma}] \\ &= \sum_{\mathbf{k}\xi\sigma} [\hbar\tilde{v}_F(\xi k_x + ik_y)\psi^{\dagger}_{BA\mathbf{k}\xi\sigma}\psi_{AB\mathbf{k}\xi\sigma} + \hbar\tilde{v}_F(\xi k_x - ik_y)\psi^{\dagger}_{AB\mathbf{k}\xi\sigma}\psi_{BA\mathbf{k}\xi\sigma}] \\ &+ \sum_{\mathbf{k}\xi\sigma} [\xi V \psi^{\dagger}_{AB\mathbf{k}\xi\sigma}\psi_{AB\mathbf{k}\xi\sigma} + \xi V \psi^{\dagger}_{BA\mathbf{k}\xi\sigma}\psi_{BA\mathbf{k}\xi\sigma}]. \end{aligned} \tag{6.10}$$

O Hamiltoniano do sistema total é

$$H = H_0 + H_d + H_{hyb},$$

em que

$$H_d = \sum_{j\sigma} \varepsilon_{j\sigma} d^{\dagger}_{j\sigma} d_{j\sigma} + \sum_j U_j d^{\dagger}_{j\uparrow} d_{j\uparrow} d^{\dagger}_{j\downarrow} d_{j\downarrow}, \tag{6.11}$$

descreve as impurezas $j = 1, 2$ e

$$H_{hyb} = \sum_{\mathbf{k}\xi\sigma j} V_{AB}\psi^{\dagger}_{AB\mathbf{k}\xi\sigma}d_{j\sigma} + \sum_{\mathbf{k}\xi\sigma j} V_{BA}\psi^{\dagger}_{BA\mathbf{k}\xi\sigma}d_{j\sigma} + \text{H.c.}, \tag{6.12}$$

descreve a hibridização entre o hospedeiro e as impurezas.

6.2 Transformações do Hamiltoniano TBG

Aplicando $\hbar\tilde{v}_F(\xi k^t_{x\xi} \mp ik^t_{y\xi}) = \hbar\tilde{v}_F|k|\xi e^{\mp i\xi\theta} = \hbar\tilde{v}_F k\xi e^{\mp i\xi\theta}$, temos

$$\begin{aligned} H &= \sum_{\mathbf{k}\xi\sigma} \hbar\tilde{v}_F k\xi e^{-i\xi\theta}\psi^{\dagger}_{AB\mathbf{k}\xi\sigma}\psi_{BA\mathbf{k}\xi\sigma} + \sum_{\mathbf{k}\xi\sigma} \hbar\tilde{v}_F k\xi e^{i\xi\theta}\psi^{\dagger}_{BA\mathbf{k}\xi\sigma}\psi_{AB\mathbf{k}\xi\sigma} \\ &+ \sum_{\mathbf{k}\xi\sigma} \xi V\psi^{\dagger}_{AB\mathbf{k}\xi\sigma}\psi_{AB\mathbf{k}\xi\sigma} + \sum_{\mathbf{k}\xi\sigma} \xi V\psi^{\dagger}_{BA\mathbf{k}\xi\sigma}\psi_{BA\mathbf{k}\xi\sigma} \\ &+ \sum_{j\sigma} \varepsilon_{j\sigma}d^{\dagger}_{j\sigma}d_{j\sigma} + \sum_{j} U_j d^{\dagger}_{j\uparrow}d_{j\uparrow}d^{\dagger}_{j\downarrow}d_{j\downarrow} \\ &+ \sum_{\mathbf{k}\xi j\sigma} V_{AB}\psi^{\dagger}_{AB\mathbf{k}\xi\sigma}d_{\sigma} + \sum_{\mathbf{k}\xi j\sigma} V_{BA}\psi^{\dagger}_{BA\mathbf{k}\xi\sigma}d_{\sigma} + \text{H.c.}. \end{aligned} \tag{6.13}$$

Considerando as seguintes transformações

$$\psi_{AB\mathbf{k}\xi\sigma} = \frac{1}{\sqrt{2}}\left[\zeta^{\xi}_{+\sigma}(\mathbf{k}) + \zeta^{\xi}_{-\sigma}(\mathbf{k})\right] \tag{6.14}$$

e

$$\psi_{BA\mathbf{k}\xi\sigma} = \frac{\xi}{\sqrt{2}}e^{i\xi\theta}\left[\zeta^{\xi}_{+\sigma}(\mathbf{k}) - \zeta^{\xi}_{-\sigma}(\mathbf{k})\right], \tag{6.15}$$

e aplicando no Hamiltoniano, temos $H_0 = H_{01} + H_{02}$, onde

$$
\begin{aligned}
H_{01} &= \sum_{\mathbf{k}\xi\sigma} \hbar\tilde{v}_F k\xi e^{-i\xi\theta} \left\{ \frac{1}{\sqrt{2}} \left[\zeta^{\xi\dagger}_{+\sigma}(\mathbf{k}) + \zeta^{\xi\dagger}_{-\sigma}(\mathbf{k}) \right] \right\} \left\{ \frac{\xi}{\sqrt{2}} e^{i\xi\theta} \left[\zeta^{\xi}_{+\sigma}(\mathbf{k}) - \zeta^{\xi}_{-\sigma}(\mathbf{k}) \right] \right\} \\
&+ \sum_{\mathbf{k}\xi\sigma} \hbar\tilde{v}_F k\xi e^{i\xi\theta} \left\{ \frac{\xi}{\sqrt{2}} e^{-i\xi\theta} \left[\zeta^{\xi\dagger}_{+\sigma}(\mathbf{k}) - \zeta^{\xi\dagger}_{-\sigma}(\mathbf{k}) \right] \right\} \left\{ \frac{1}{\sqrt{2}} \left[\zeta^{\xi}_{+\sigma}(\mathbf{k}) + \zeta^{\xi}_{-\sigma}(\mathbf{k}) \right] \right\} \\
&= \sum_{\mathbf{k}\xi\sigma} \frac{1}{2} \hbar\tilde{v}_F k \left[\zeta^{\xi\dagger}_{+\sigma}(\mathbf{k}) \zeta^{\xi}_{+\sigma}(\mathbf{k}) - \zeta^{\xi\dagger}_{-\sigma}(\mathbf{k}) \zeta^{\xi}_{-\sigma}(\mathbf{k}) \right] \\
&+ \sum_{\mathbf{k}\xi\sigma} \frac{1}{2} \hbar\tilde{v}_F k \left[\zeta^{\xi\dagger}_{+\sigma}(\mathbf{k}) \zeta^{\xi}_{+\sigma}(\mathbf{k}) - \zeta^{\xi\dagger}_{-\sigma}(\mathbf{k}) \zeta^{\xi}_{-\sigma}(\mathbf{k}) \right] \\
&= \sum_{\mathbf{k}\xi\sigma} \hbar\tilde{v}_F k \left[\zeta^{\xi\dagger}_{+\sigma}(\mathbf{k}) \zeta^{\xi}_{+\sigma}(\mathbf{k}) - \zeta^{\xi\dagger}_{-\sigma}(\mathbf{k}) \zeta^{\xi}_{-\sigma}(\mathbf{k}) \right], \qquad (6.16)
\end{aligned}
$$

$$
\begin{aligned}
H_{02} &= \xi V \frac{1}{\sqrt{2}} \left[\zeta^{\xi\dagger}_{+\sigma}(\mathbf{k}) + \zeta^{\xi\dagger}_{-\sigma}(\mathbf{k}) \right] \frac{1}{\sqrt{2}} \left[\zeta^{\xi}_{+\sigma}(\mathbf{k}) + \zeta^{\xi}_{-\sigma}(\mathbf{k}) \right] \\
&+ \xi V \frac{\xi}{\sqrt{2}} e^{-i\xi\theta} \left[\zeta^{\xi\dagger}_{+\sigma}(\mathbf{k}) - \zeta^{\xi\dagger}_{-\sigma}(\mathbf{k}) \right] \frac{\xi}{\sqrt{2}} e^{i\xi\theta} \left[\zeta^{\xi}_{+\sigma}(\mathbf{k}) - \zeta^{\xi}_{-\sigma}(\mathbf{k}) \right] \\
&= \xi V \left[\frac{1}{2} \zeta^{\xi\dagger}_{+\sigma}(\mathbf{k}) \zeta^{\xi}_{+\sigma}(\mathbf{k}) + \zeta^{\xi\dagger}_{+\sigma}(\mathbf{k}) \zeta^{\xi}_{-\sigma}(\mathbf{k}) \right] \\
&+ \xi V \left[\zeta^{\xi\dagger}_{-\sigma}(\mathbf{k}) \zeta^{\xi}_{+\sigma}(\mathbf{k}) + \zeta^{\xi\dagger}_{-\sigma}(\mathbf{k}) \zeta^{\xi}_{-\sigma}(\mathbf{k}) \right] \\
&+ \xi V \frac{1}{2} \left[\zeta^{\xi\dagger}_{+\sigma}(\mathbf{k}) \zeta^{\xi}_{+\sigma}(\mathbf{k}) - \zeta^{\xi\dagger}_{+\sigma}(\mathbf{k}) \zeta^{\xi}_{-\sigma}(\mathbf{k}) \right] \\
&+ \xi V \frac{1}{2} \left[-\zeta^{\xi\dagger}_{-\sigma}(\mathbf{k}) \zeta^{\xi}_{+\sigma}(\mathbf{k}) + \zeta^{\xi\dagger}_{-\sigma}(\mathbf{k}) \zeta^{\xi}_{-\sigma}(\mathbf{k}) \right] \\
&= \xi V \left[\zeta^{\xi\dagger}_{+\sigma}(\mathbf{k}) \zeta^{\xi}_{+\sigma}(\mathbf{k}) + \zeta^{\xi\dagger}_{-\sigma}(\mathbf{k}) \zeta^{\xi}_{-\sigma}(\mathbf{k}) \right], \qquad (6.17)
\end{aligned}
$$

$$
\begin{aligned}
H_{hyb} &= \sum_{\mathbf{k}\xi\sigma} V_{AB} \psi^{\dagger}_{A\mathbf{k}\xi\sigma} d_{\sigma} + \sum_{\mathbf{k}\xi\sigma} V_{BA} \psi^{\dagger}_{BA\mathbf{k}\xi\sigma} d_{\sigma} \\
&+ \sum_{\mathbf{k}\xi\sigma} V_{AB} d^{\dagger}_{1\sigma} \psi_{A\mathbf{k}\xi\sigma} + \sum_{\mathbf{k}\xi\sigma} V_{BA} d^{\dagger}_{1\sigma} \psi^{\dagger}_{B\mathbf{k}\xi\sigma} \\
&= \sum_{\mathbf{k}\xi\sigma} V_{AB} \left\{ \frac{1}{\sqrt{2}} \left[\zeta^{\xi\dagger}_{+\sigma}(\mathbf{k}) + \zeta^{\xi\dagger}_{-\sigma}(\mathbf{k}) \right] \right\} d_{\sigma} + \sum_{\mathbf{k}\xi\sigma} V_{BA} \left\{ \frac{\xi}{\sqrt{2}} e^{-i\xi\theta_k} \left[\zeta^{\xi\dagger}_{+\sigma}(\mathbf{k}) - \zeta^{\xi\dagger}_{-\sigma}(\mathbf{k}) \right] \right\} d_{\sigma} \\
&+ \sum_{\mathbf{k}\xi\sigma} V^{*}_{AB} d^{\dagger}_{\sigma} \left\{ \frac{1}{\sqrt{2}} \left[\zeta^{\xi}_{+\sigma}(\mathbf{k}) + \zeta^{\xi}_{-\sigma}(\mathbf{k}) \right] \right\} + \sum_{\mathbf{k}\xi\sigma} V^{*}_{BA} d^{\dagger}_{\sigma} \left\{ \frac{\xi}{\sqrt{2}} e^{i\xi\theta} \left[\zeta^{\xi}_{+\sigma}(\mathbf{k}) - \zeta^{\xi}_{-\sigma}(\mathbf{k}) \right] \right\}. \\
& \qquad (6.18)
\end{aligned}
$$

Considerando $V_{AB} = v_0$ e $V_{BA} = \xi \frac{\hbar \tilde{v}_F k v_1 e^{i\xi\theta_k}}{-t}$, temos

$$\begin{aligned} H_{hyb} &= \sum_{\mathbf{k}\xi\sigma} v_0 \left\{ \frac{1}{\sqrt{2}} \left[\zeta^{\xi\dagger}_{+\sigma}(\mathbf{k}) + \zeta^{\xi\dagger}_{-\sigma}(\mathbf{k}) \right] \right\} d_\sigma \\ &+ \sum_{\mathbf{k}\xi\sigma} \xi \frac{\hbar \tilde{v}_F k v_1 e^{i\xi\theta}}{-t} \left\{ \frac{\xi}{\sqrt{2}} e^{-i\xi\theta} \left[\zeta^{\xi\dagger}_{+\sigma}(\mathbf{k}) - \zeta^{\xi\dagger}_{-\sigma}(\mathbf{k}) \right] \right\} d_\sigma \\ &+ \sum_{\mathbf{k}\xi\sigma} v_0 d^\dagger_\sigma \left\{ \frac{1}{\sqrt{2}} \left[\zeta^{\xi}_{+\sigma}(\mathbf{k}) + \zeta^{\xi}_{-\sigma}(\mathbf{k}) \right] \right\} \\ &+ \sum_{\mathbf{k}\xi\sigma} \xi \frac{\hbar \tilde{v}_F k v_1 e^{-i\xi\theta}}{-t} d^\dagger_\sigma \left\{ \frac{\xi}{\sqrt{2}} e^{i\xi\theta} \left[\zeta^{\xi}_{+\sigma}(\mathbf{k}) - \zeta^{\xi}_{-\sigma}(\mathbf{k}) \right] \right\}, \end{aligned} \tag{6.19}$$

resultando em

$$\begin{aligned} H_{hyb} &= \sum_{\mathbf{k}\xi\sigma} \frac{v_0}{\sqrt{2}} \left[\zeta^{\xi\dagger}_{+\sigma}(\mathbf{k}) d_\sigma + \zeta^{\xi\dagger}_{-\sigma}(\mathbf{k}) d_\sigma \right] + \text{H.c.} \\ &+ \sum_{\mathbf{k}\xi\sigma} \frac{\hbar \tilde{v}_F k v_1}{-t\sqrt{2}} \left[\zeta^{\xi\dagger}_{+\sigma}(\mathbf{k}) d_\sigma - \zeta^{\xi\dagger}_{-\sigma}(\mathbf{k}) d_\sigma \right] + \text{H.c.}. \end{aligned} \tag{6.20}$$

6.3 Decomposição de ondas parciais

Mudando da base discreta para o correspondente contínuo $\mathbf{k}$, escrevemos

$$H_0 = \sum_{\xi\sigma} 2\pi \frac{\Omega}{(2\pi)^2} \int k dk \hbar \tilde{v}_F k \left[\zeta^{\xi\dagger}_{+\sigma}(\mathbf{k}) \zeta^{\xi}_{+\sigma}(\mathbf{k}) - \zeta^{\xi\dagger}_{-\sigma}(\mathbf{k}) \zeta^{\xi}_{-\sigma}(\mathbf{k}) \right], \tag{6.21}$$

$$\begin{aligned} H_{hyb} &= \sum_{\xi\sigma} 2\pi \frac{\Omega}{(2\pi)^2} \int k dk \frac{v_0}{\sqrt{2}} \left[\zeta^{\xi\dagger}_{+\sigma}(\mathbf{k}) d_\sigma + \zeta^{\xi\dagger}_{-\sigma}(\mathbf{k}) d_\sigma \right] + \text{H.c.} \\ &+ \sum_{\xi\sigma} 2\pi \frac{\Omega}{(2\pi)^2} \int k dk \frac{\hbar \tilde{v}_F k v_1}{-t\sqrt{2}} \left[\zeta^{\xi\dagger}_{+\sigma}(\mathbf{k}) d_\sigma - \zeta^{\xi\dagger}_{-\sigma}(\mathbf{k}) d_\sigma \right] + \text{H.c.}, \end{aligned} \tag{6.22}$$

onde a decomposição de ondas parciais é

$$\zeta_{\pm}^{\xi}(\mathbf{k}) = \frac{1}{\sqrt{k}}\left[\frac{(2\pi)^2}{\Omega}\right]^{\frac{1}{2}}\sum_{m=-\infty}^{\infty}\frac{1}{\sqrt{2\pi}}e^{im\theta}\zeta_{\pm\sigma\xi}^{m}(k). \tag{6.23}$$

Ressaltamos que apenas o estado $m = 0$ (isotrópico) deve ser levado em consideração, uma vez que assumimos simetria radial para as impurezas,

$$\begin{aligned} H_{01} &= \sum_{\xi\sigma} 2\pi\frac{\Omega}{(2\pi)^2}\int kdk\hbar\tilde{v}_F k\left[\frac{1}{\sqrt{k}}\left[\frac{(2\pi)^2}{\Omega}\right]^{\frac{1}{2}}\frac{1}{\sqrt{2\pi}}\zeta_{+\sigma\xi}^{\dagger}(k)\right]\left[\frac{1}{\sqrt{k}}\left[\frac{(2\pi)^2}{\Omega}\right]^{\frac{1}{2}}\frac{1}{\sqrt{2\pi}}\zeta_{+\sigma\xi}(k)\right] \\ &- \sum_{\xi\sigma} 2\pi\frac{\Omega}{(2\pi)^2}\int kdk\hbar\tilde{v}_F k\left[\frac{1}{\sqrt{k}}\left[\frac{(2\pi)^2}{\Omega}\right]^{\frac{1}{2}}\frac{1}{\sqrt{2\pi}}\zeta_{-\sigma\xi}^{\dagger}(k)\right]\left[\frac{1}{\sqrt{k}}\left[\frac{(2\pi)^2}{\Omega}\right]^{\frac{1}{2}}\frac{1}{\sqrt{2\pi}}\zeta_{-\sigma\xi}(k)\right] \\ &= \sum_{\xi\sigma}\int_0^{\infty} dk\hbar\tilde{v}_F|k|\zeta_{+\sigma\xi}^{\dagger}(k)\,\zeta_{+\sigma\xi}(k) - \sum_{\xi\sigma}\int_0^{\infty} dk\hbar\tilde{v}_F|k|\zeta_{-\sigma\xi}^{\dagger}(k)\,\zeta_{-\sigma\xi}(k), \end{aligned} \tag{6.24}$$

$$\begin{aligned} H_{02} &= \sum_{\xi\sigma}\xi V\left[2\pi\frac{\Omega}{(2\pi)^2}\int kdk\zeta_{+\sigma}^{\xi\dagger}(\mathbf{k})\,\zeta_{+\sigma}^{\xi}(\mathbf{k}) + 2\pi\frac{\Omega}{(2\pi)^2}\int kdk\zeta_{-\sigma}^{\xi\dagger}(\mathbf{k})\,\zeta_{-\sigma}^{\xi}(\mathbf{k})\right] \\ &= \sum_{\xi\sigma}\xi V\left[\int_0^{\infty} dk\zeta_{+\sigma\xi}^{\dagger}(k)\,\zeta_{+\sigma\xi}(k) + \int_0^{\infty} dk\zeta_{-\sigma\xi}^{\dagger}(k)\,\zeta_{-\sigma\xi}(k)\right] \\ &= \sum_{\xi\sigma}\int_{-\infty}^{+\infty}\xi V dkc_{\sigma\xi}^{\dagger}(k)\,c_{\sigma\xi}(k) \end{aligned} \tag{6.25}$$

e

$$
\begin{aligned}
H_{hyb} &= \sum_{\xi\sigma} 2\pi \frac{\Omega}{(2\pi)^2} \int kdk \frac{v_0}{\sqrt{2}} \frac{1}{\sqrt{k}} \left[\frac{(2\pi)^2}{\Omega}\right]^{\frac{1}{2}} \frac{1}{\sqrt{2\pi}} \zeta^{\dagger}_{+\sigma\xi}(k)\, d_\sigma \\
&+ \sum_{\xi\sigma} 2\pi \frac{\Omega}{(2\pi)^2} \int kdk \frac{v_0}{\sqrt{2}} \frac{1}{\sqrt{k}} \left[\frac{(2\pi)^2}{\Omega}\right]^{\frac{1}{2}} \frac{1}{\sqrt{2\pi}} \zeta^{\dagger}_{-\sigma\xi}(k)\, d_\sigma \\
&+ \sum_{\xi\sigma} 2\pi \frac{\Omega}{(2\pi)^2} \int kdk \frac{v_0}{\sqrt{2}} d^{\dagger}_\sigma \frac{1}{\sqrt{k}} \left[\frac{(2\pi)^2}{\Omega}\right]^{\frac{1}{2}} \frac{1}{\sqrt{2\pi}} \zeta_{+\sigma\xi}(k) \\
&+ \sum_{\xi\sigma} 2\pi \frac{\Omega}{(2\pi)^2} \int kdk \frac{v_0}{\sqrt{2}} d^{\dagger}_\sigma \frac{1}{\sqrt{k}} \left[\frac{(2\pi)^2}{\Omega}\right]^{\frac{1}{2}} \frac{1}{\sqrt{2\pi}} \zeta_{-\sigma\xi}(k) \\
&+ \sum_{\xi\sigma} 2\pi \frac{\Omega}{(2\pi)^2} \int kdk \frac{\hbar\tilde{v}_F k v_1}{-t\sqrt{2}} \frac{1}{\sqrt{k}} \left[\frac{(2\pi)^2}{\Omega}\right]^{\frac{1}{2}} \frac{1}{\sqrt{2\pi}} \zeta^{\dagger}_{+\sigma\xi}(k)\, d_\sigma \\
&- \sum_{\xi\sigma} 2\pi \frac{\Omega}{(2\pi)^2} \int kdk \frac{\hbar\tilde{v}_F k v_1}{-t\sqrt{2}} \frac{1}{\sqrt{k}} \left[\frac{(2\pi)^2}{\Omega}\right]^{\frac{1}{2}} \frac{1}{\sqrt{2\pi}} \zeta^{\dagger}_{-\sigma\xi}(k)\, d_\sigma \\
&+ \sum_{\xi\sigma} 2\pi \frac{\Omega}{(2\pi)^2} \int kdk \frac{\hbar\tilde{v}_F k v_1}{-t\sqrt{2}} d^{\dagger}_\sigma \frac{1}{\sqrt{k}} \left[\frac{(2\pi)^2}{\Omega}\right]^{\frac{1}{2}} \frac{1}{\sqrt{2\pi}} \zeta_{+\sigma\xi}(k) \\
&- \sum_{\xi\sigma} 2\pi \frac{\Omega}{(2\pi)^2} \int kdk \frac{\hbar\tilde{v}_F k v_1}{-t\sqrt{2}} d^{\dagger}_\sigma \frac{1}{\sqrt{k}} \left[\frac{(2\pi)^2}{\Omega}\right]^{\frac{1}{2}} \frac{1}{\sqrt{2\pi}} \zeta_{-\sigma\xi}(k) \\
&= \sum_{\xi\sigma} \int_0^\infty dk \frac{v_0\sqrt{\Omega|k|\pi}}{2\pi} \left[\zeta^{\dagger}_{+\sigma\xi}(k)\, d_\sigma + \zeta^{\dagger}_{-\sigma\xi}(k)\, d_\sigma\right] \\
&+ \sum_{\xi\sigma} \int_0^\infty dk \frac{v_0\sqrt{\Omega|k|\pi}}{2\pi} \left[d^{\dagger}_\sigma \zeta_{+\sigma\xi}(k) + d^{\dagger}_\sigma \zeta_{-\sigma\xi}(k)\right] \\
&+ \sum_{\xi\sigma} \int_0^\infty dk \frac{v_1\sqrt{\Omega|k|\pi}}{2\pi} \frac{\hbar\tilde{v}_F|k|}{-t} \left[\zeta^{\dagger}_{+\sigma\xi}(k)\, d_\sigma - \zeta^{\dagger}_{-\sigma\xi}(k)\, d_\sigma\right] \\
&+ \sum_{\xi\sigma} \int_0^\infty dk \frac{v_1\sqrt{\Omega|k|\pi}}{2\pi} \frac{\hbar\tilde{v}_F|k|}{-t} \left[d^{\dagger}_\sigma \zeta_{+\sigma\xi}(k) - d^{\dagger}_\sigma \zeta_{-\sigma\xi}(k)\right].
\end{aligned}
\tag{6.26}
$$

Agora estendemos k de $(0,\infty)$ à $(-\infty,+\infty)$ definindo $c_{\sigma\xi}(k) = \zeta^{\xi}_{+\sigma}(k)$ para $k > 0$ e $c_{\sigma\xi}(k) = \zeta^{\xi}_{-\sigma}(k)$, para $k < 0$. Sendo assim

$$H_0 = \sum_{\xi\sigma}\int_{-\infty}^{+\infty} dk(\hbar\tilde{v}_F k + \xi Q_0)c^{\dagger}_{\sigma\xi}(k)\, c_{\sigma\xi}(k)\,, \tag{6.27}$$

e

$$H_{hyb} = \sum_{\xi\sigma}\int dk\frac{\sqrt{\Omega|k|\pi}}{2\pi}\left(v_0 + v_1\frac{\hbar\tilde{v}_F k}{(-t)}\right)c^{\dagger}_{\sigma\xi}(k)\, d_\sigma + \text{H.c.}, \tag{6.28}$$

O Hamiltoniano total do sistema pode ser escrito como

$$\begin{aligned} H &= H_0 + H_d + H_{hyb} \\ &= \sum_{\xi\sigma}\int_{-\infty}^{+\infty} dk(\hbar\tilde{v}_F k + \xi V)c^{\dagger}_{\sigma\xi}(k)\, c_{\sigma\xi}(k) \\ &+ \sum_{j\sigma}\varepsilon_{j\sigma}d^{\dagger}_{j\sigma}d_{j\sigma} + \sum_j U_j d^{\dagger}_{j\uparrow}d_{j\uparrow}d^{\dagger}_{j\downarrow}d_{j\downarrow} \\ &+ \sum_{\xi\sigma j}\int dk\frac{\sqrt{\Omega|k|\pi}}{2\pi}v_j^0\left(1 + q_j\frac{\hbar\tilde{v}_F k}{(-D)}\right)c^{\dagger}_{\sigma\xi}(k)\, d_{j\sigma} \\ &+ \sum_{\xi\sigma j}\int dk\frac{\sqrt{\Omega|k|\pi}}{2\pi}v_j^{0*}\left(1 + q_j^*\frac{\hbar\tilde{v}_F k}{(-D)}\right)d^{\dagger}_{j\sigma}c_{\sigma\xi}(k)\,, \end{aligned} \tag{6.29}$$

com

$$q_j = \frac{v_j^1}{v_j^0}\frac{D}{t}. \tag{6.30}$$

Entretanto, para esse trabalho consideramos $q_j = 0$ (acoplamento local), sendo assim

$$\begin{aligned} H &= H_0 + H_d + H_{hyb} \\ &= \sum_{\xi\sigma} \int_{-\infty}^{+\infty} dk(\hbar\tilde{v}_F k + \xi V) c^{\dagger}_{\sigma\xi}(k)\, c_{\sigma\xi}(k) \\ &+ \sum_{j\sigma} \varepsilon_{j\sigma} d^{\dagger}_{j\sigma} d_{j\sigma} + \sum_{j} U_j d^{\dagger}_{j\uparrow} d_{j\uparrow} d^{\dagger}_{j\downarrow} d_{j\downarrow} \\ &+ \sum_{\xi\sigma j} \int dk \frac{\sqrt{\Omega|k|\pi}}{2\pi} v_0 c^{\dagger}_{\sigma\xi}(k)\, d_{j\sigma} \\ &+ \sum_{\xi\sigma j} \int dk \frac{\sqrt{\Omega|k|\pi}}{2\pi} v_0 d^{\dagger}_{j\sigma} c_{\sigma\xi}(k)\,. \end{aligned} \tag{6.31}$$

6.4 Densidade local de estados (LDOS)

A LDOS para o sistema TBG é definida como

$$\rho_{LDOS} = -\frac{1}{\pi}\mathrm{Im}\left[\tilde{\mathcal{G}}(\omega)\right], \tag{6.32}$$

onde é necessário calcular a função de Green

$$\tilde{\mathcal{G}}(t) = -\frac{i}{\hbar}\theta(t) Z^{-1} \sum_n e^{-\beta E_n} \left\langle n \left| \left[\psi(t), \psi^{\dagger}(0)\right]_+ \right| n \right\rangle, \tag{6.33}$$

onde

$$\psi(\mathbf{R}) = \frac{1}{2}\sum_{\xi\sigma j} \int dk \frac{\sqrt{\Omega|k|\pi}}{2\pi} c_{\sigma\xi}(k) \tag{6.34}$$

é o operador de campo. Sendo assim, a função de Green para obtermos a LDOS é definida como

$$\tilde{\mathcal{G}}(\omega) = \frac{1}{4}\sum_{\sigma\xi\xi'} \left(\frac{\sqrt{\Omega\pi}}{2\pi}\right)^2 \int dk \int dq \sqrt{|k|}\sqrt{|q|}\mathcal{G}_{c_{\sigma\xi}(k) c_{\sigma'\xi'}(q)}(\omega), \tag{6.35}$$

sendo necessário calcular a função de Green

$$\mathcal{G}_{c_{\sigma\xi}(k)c_{\sigma'\xi'}(q)}(t) = -\frac{i}{\hbar}\theta(t)\,Z^{-1}\sum_n e^{-\beta E_n}\left\langle n\left|\left[c_{\sigma\xi}(k),c^{\dagger}_{\sigma'\xi'}(q)\right]_+\right|n\right\rangle. \tag{6.36}$$

Aplicando a EOM e a transformada de Fourier, temos

$$\begin{aligned}\tilde{\mathcal{G}}_{c_{\sigma\xi}(k)c_{\sigma\xi'}(q)}(\omega) &= \frac{\delta_{\xi\xi'}\delta(k-q)}{\left(\omega^+_\xi-\hbar\tilde{v}_F k\right)}\\ &+ \sum_j \frac{\sqrt{\Omega|k|\pi}}{2\pi\left(\omega^+_\xi-\hbar\tilde{v}_F k\right)}v_0\tilde{\mathcal{G}}_{d_{j\sigma}c_{\sigma\xi'}(q)}(\omega),\end{aligned} \tag{6.37}$$

onde $\omega^+_\xi=\omega-\xi V+i\eta$ e $\sigma=\sigma'$. Agora, precisamos calcular $\tilde{\mathcal{G}}_{d_{j\sigma}c_{\sigma\xi'}(q)}(\omega)$. Como no cálculo do semimetal de Weyl, utilizaremos a função de Green avançada

$$\mathcal{F}_{d_{j\sigma}c_{\sigma\xi'}(q)}(t) = \frac{i}{\hbar}\theta(t)\,Z^{-1}\sum_n e^{-\beta E_n}\left\langle n\left|\left[d^{\dagger}_{j\sigma},c_{\sigma\xi'}(q)\right]_+\right|n\right\rangle. \tag{6.38}$$

Aplicando a EOM e a transformada de Fourier, temos

$$\tilde{\mathcal{F}}_{d_{j\sigma}c_{\sigma\xi'}(q)}(\omega) = \sum_l \frac{\sqrt{\Omega|q|\pi}}{2\pi\left(\omega^-_{\xi'}-\hbar\tilde{v}_F q\right)}v_0\tilde{\mathcal{F}}_{d_{j\sigma}d_{l\sigma}}(\omega). \tag{6.39}$$

Aplicando a propriedade $\tilde{\mathcal{G}}_{d_{j\sigma}c_{\sigma\xi'}(q)}(\omega)=\left[\mathcal{F}_{d_{j\sigma}c_{\sigma\xi'}(q)}(\omega)\right]^{\dagger}$, temos que

$$\tilde{\mathcal{G}}_{d_{j\sigma}c_{\sigma\xi'}(q)}(\omega) = \sum_l \frac{\sqrt{\Omega|q|\pi}}{2\pi\left(\omega^+_{\xi'}-\hbar\tilde{v}_F q\right)}v_0\tilde{\mathcal{G}}_{d_{j\sigma}d_{l\sigma}}(\omega). \tag{6.40}$$

Substituindo a Eq. (6.40) em Eq. (6.37), temos

$$\begin{aligned}\mathcal{G}_{c_{\sigma\xi}(k)c_{\sigma\xi'}(q)}(\omega) &= \frac{\delta_{\xi\xi'}\delta(k-q)}{\left(\omega^+_\xi-\hbar\tilde{v}_F k\right)}\\ &+ \sum_{jl}\left[\frac{\sqrt{\Omega\pi}}{2\pi}\frac{\sqrt{|k|}}{\left(\omega^+_\xi-\hbar\tilde{v}_F k\right)}v_0\right]\left[\frac{\sqrt{\Omega\pi}}{2\pi}\frac{\sqrt{|q|}}{\left(\omega^+_{\xi'}-\hbar\tilde{v}_F q\right)}v_0\right]\tilde{\mathcal{G}}_{d_{j\sigma}d_{l\sigma}}(\omega).\end{aligned} \tag{6.41}$$

Voltando para a Eq. (6.32), a expressão da LDOS é dada por

$$\begin{aligned}
\rho_{LDOS} &= -\frac{1}{\pi}\mathrm{Im}\left[\frac{1}{4}\sum_{\sigma\xi\xi'}\left(\frac{\sqrt{\Omega\pi}}{2\pi}\right)^2\int dk\int dq\sqrt{|k|}\sqrt{|q|}\mathcal{G}_{c_{\sigma\xi}(k)c_{\sigma\xi'}(q)}\left(\omega\right)\right] \\
&= -\frac{1}{\pi}\mathrm{Im}\left[\sum_{\xi}2\frac{1}{v_0^2}\left(\frac{\sqrt{\Omega\pi}}{2\pi}\right)^2\int dk v_0^2\frac{|k|}{\left(\omega_\xi^+-\hbar\tilde{v}_F k\right)}\right] \\
&+ -\frac{1}{\pi}\mathrm{Im}\left\{\sum_{\xi\xi'\sigma}\sum_{jl}\int dk\frac{1}{v_0^2}\left[\frac{\Omega\pi}{(2\pi)^2}\frac{|k|}{\left(\omega_\xi^+-\hbar\tilde{v}_F k\right)}v_0^2\right]\right. \\
&\times \left.\int dq\left[\frac{\Omega\pi}{(2\pi)^2}\frac{|q|}{\left(\omega_{\xi'}^+-\hbar\tilde{v}_F q\right)}v_0^2\right]\tilde{\mathcal{G}}_{d_{j\sigma}d_{l\sigma}}\left(\omega\right)\right\} \\
\rho_{LDOS}\left(\omega\right) &= \frac{1}{v_0^2}2\rho_0+\sum_{\xi\xi'\sigma}\sum_{jl}\frac{1}{v_0^2}\mathrm{Im}\left\{\Sigma_\xi\left(\omega\right)\left\langle\left\langle d_{j\sigma};d_{l\sigma}^\dagger\right\rangle\right\rangle\Sigma_{\xi'}\left(\omega\right)\right\},
\end{aligned} \tag{6.42}$$

onde

$$\rho_0=\sum_\xi\left(\frac{\sqrt{\Omega\pi}}{2\pi}\right)^2\int dk\mathrm{Im}\left[v_0^2\frac{|k|}{\left(\omega_\xi^+-\hbar\tilde{v}_F k\right)}\right]=\sum_\xi\frac{\Omega}{4\pi\hbar^2\tilde{v}_F^2}\left|\omega_\xi\right| \tag{6.43}$$

é a densidade de estados do TBG e

$$\Sigma_\xi\left(\omega\right)=\int dk\frac{\Omega\pi}{(2\pi)^2}\frac{|k|}{\left(\omega_\xi^+-\hbar\tilde{v}_F k\right)}v_0^2 \tag{6.44}$$

é a auto energia.

6.5 Auto-energia

Separando as partes real e a imaginária

$$\begin{aligned}
\Sigma_{\xi}(\omega) &= \int dk v_0^2 \frac{\Omega\pi}{(2\pi)^2} \frac{|k|}{(\omega_\xi - \hbar\tilde{v}_F k + i\eta)} \\
&= \int_{-D}^{0} v_0^2 \frac{d\omega_k}{\hbar\tilde{v}_F} \frac{\Omega\pi}{(2\pi)^2} \frac{1}{\hbar\tilde{v}_F} \frac{|\omega_\xi|}{(\omega_\xi - \omega_k + i\eta)} \frac{(\omega_\xi - \omega_k - i\eta)}{(\omega_\xi - \omega_k - i\eta)} \\
&= \int_{-D}^{0} v_0^2 \frac{d\omega_k}{\hbar^2\tilde{v}_F^2} |\omega_\xi| \frac{\Omega\pi}{(2\pi)^2} \left[\frac{(\omega_\xi - \omega_k)}{(\omega_\xi - \omega_k)^2 + \eta^2} - i \frac{\eta}{(\omega_\xi - \omega_k)^2 + \eta^2} \right] \\
&= \int_{-D}^{0} v_0^2 \frac{d\omega_k}{\hbar^2\tilde{v}_F^2} |\omega_\xi| \frac{\Omega\pi}{(2\pi)^2} \left[\frac{1}{(\omega_\xi - \omega_k)} - i\delta(\omega_\xi - \omega_k) \right] \\
&= \int_{-D}^{0} v_0^2 \frac{d\omega_k}{\hbar^2\tilde{v}_F^2} \frac{\Omega\pi}{(2\pi)^2} \left[\frac{\omega_\xi}{(\omega_\xi - \omega_k)} - i|\omega_\xi| \pi\delta(\omega_\xi - \omega_k) \right] \\
&= \int_{-D}^{0} v_0^2 \frac{d\omega_k}{\hbar^2\tilde{v}_F^2} \frac{\Omega\pi}{(2\pi)^2} \left[\frac{\omega_\xi}{(\omega_\xi - \omega_k)} \right] \\
&- i\pi|\omega_\xi| \frac{\Omega}{4\pi\hbar^2\tilde{v}_F^2} v_0^2. \qquad (6.45)
\end{aligned}$$

Vamos calcular a parte real

$$\Sigma_{\xi}^{\mathrm{R}}(\omega) = \int_{-D}^{0} v_0^2 \frac{d\omega_k}{\hbar^2\tilde{v}_F^2} \frac{\Omega\pi}{(2\pi)^2} \left[\frac{\omega_\xi}{(\omega_\xi - \omega_k)} \right]. \qquad (6.46)$$

O cálculo da integral é

$$\begin{aligned}
\int_{-D}^{D} d\omega_k \frac{\omega_k}{(\omega_\xi - \omega_k)} &= \int_{-D}^{D} d\omega_k \left[-\frac{\omega_\xi}{(\omega_k - \omega_\xi)} - \frac{(\omega_k - \omega_\xi)}{(\omega_k - \omega_\xi)} \right] \\
&= \int_{-D}^{D} d\omega_k \left[-\frac{\omega_\xi}{(\omega_k - \omega_\xi)} - 1 \right] \\
&= \left[-\omega_\xi \mathbf{ln}(|\omega_k - \omega_\xi|) - \omega_k \right]_0^D \\
&- \left[-\omega_\xi \mathbf{ln}(|\omega_k - \omega_\xi|) - \omega_k \right]_{-D}^0 \\
&= -\omega_\xi \mathbf{ln}(|D - \omega_\xi|) - D + \omega_\xi \mathbf{ln}(|\omega_\xi|) \\
&+ \omega_\xi \mathbf{ln}(|\omega_\xi|) - \omega_\xi \mathbf{ln}(|-D - \omega_\xi|) + D \\
&= \omega_\xi \mathbf{ln}\left(\frac{|\omega_\xi|}{|D - \omega_\xi|} \right) + \omega_\xi \mathbf{ln}\left(\frac{|\omega_\xi|}{|D + \omega_\xi|} \right) \\
&= \omega_\xi \mathbf{ln}\left(\frac{|\omega_\xi^2|}{|D^2 - \omega_\xi^2|} \right). \qquad (6.47)
\end{aligned}$$

Sendo assim

$$\Sigma_{\xi}^{\mathrm{R}}(\omega) = v_0^2 \frac{\Omega}{4\pi\hbar^2\tilde{v}_F^2}\omega_{\xi}\ln\left(\frac{\left|\omega_{\xi}^2\right|}{\left|D^2-\omega_{\xi}^2\right|}\right). \tag{6.48}$$

Como resultado, a auto-energia é definida como

$$\begin{aligned}\Sigma_{\xi}(\omega) &= v_0^2 \frac{\Omega}{4\pi\hbar^2\tilde{v}_F^2}\omega_{\xi}\ln\left(\frac{\left|\omega_{\xi}^2\right|}{\left|D^2-\omega_{\xi}^2\right|}\right) \\ &- i\pi\left|\omega_{\xi}\right| v_0^2\frac{\Omega}{4\pi\hbar^2\tilde{v}_F^2}.\end{aligned} \tag{6.49}$$

6.6 Funções de Green das impurezas

Do mesmo modo que utilizamos o modelo de Anderson para o sistema Weyl, as funções de Green das impurezas no sistema TBG são semelhantes, tendo como diferença as auto-energias para cada sistema. Sendo assim, as funções de Green das impurezas podem ser definidas como

$$\tilde{\mathcal{G}}_{d_{j\sigma}d_{l\sigma}}(\omega) = \frac{\lambda_j^{\bar{\sigma}}}{\left(\omega^+ - \varepsilon_{j\sigma} - \Sigma_{j\bar{j}}^{\bar{\sigma}}\right)}, \tag{6.50}$$

e

$$\tilde{\mathcal{G}}_{d_{j\sigma}d_{\bar{j}\sigma}}(\omega) = \frac{\Sigma_0\lambda_j^{\bar{\sigma}}}{\left(\omega^+ - \varepsilon_{j\sigma} - \Sigma_{j\bar{j}}^{\bar{\sigma}}\right)}\tilde{\mathcal{G}}_{d_{\bar{j}\sigma}d_{\bar{j}\sigma}}(\omega), \tag{6.51}$$

onde

$$\Sigma_{j\bar{j}}^{\bar{\sigma}} = \tilde{\Sigma}(\omega) + \lambda_j^{\bar{\sigma}}\lambda_{\bar{j}}^{\bar{\sigma}}\frac{\tilde{\Sigma}(\omega)\tilde{\Sigma}(\omega)}{\left(\omega^+ - \varepsilon_{\bar{j}\sigma} - \tilde{\Sigma}(\omega)\right)},$$

sendo $\tilde{\Sigma} = \sum_{\xi}\Sigma_{\xi}$

$$\lambda_j^{\bar{\sigma}} = 1 + \frac{< n_{jd\bar{\sigma}} > U_j}{(\omega^+ - \varepsilon_{j\sigma} - U_j - \Sigma_0)}, \tag{6.52}$$

e

$$< n_{jd\bar{\sigma}} > = -\frac{1}{\pi} \int_{-D}^{0} \mathrm{Im} \left[\left\langle \left\langle d_{j\bar{\sigma}}; d_{j\bar{\sigma}}^{\dagger} \right\rangle \right\rangle \right] d\omega, \tag{6.53}$$

sendo o cálculo da ocupação do átomo e D é a energia de *cutoff*.

Como o objetivo de estudo neste sistema foi observar a interação entre as impurezas, definimos a função de Green de correlação a partir da LDOS já calculada, isto é,

$$\delta\rho_{jl}(\omega) = -\frac{1}{\pi v_0^2} \sum_{\xi\xi'\sigma} \mathrm{Im} \left\{ \Sigma_\xi(\omega) \tilde{\mathcal{G}}_{d_{j\sigma} d_{l\sigma}}(\omega) \Sigma_\xi(\omega) \right\}. \tag{6.54}$$

Capítulo 7

Resultados e discussão

Com base nas equações calculadas no capítulo anterior, o objetivo de estudo é:

- Explorar a twistrônica baseada em frustração atômica. Investigar estados atômicos frustrados em moléculas diatômicas hospedadas pela configuração do grafeno bicamada torcido pelo primeiro ângulo mágico e com simetria de inversão quebrada nos cones de Dirac das mini-zonas de Brillouin do sistema. Os resultados foram publicados na 2D Materials 8, 045038 (2021) [44], assim como foi matéria de reportagem da FAPESP [56].

7.1 Twistrônica baseada em frustração atômica

Nesta seção, adotamos o formato da tese apresentada por um dos egressos do grupo [57], uma vez que os resultados do TBG contém os mesmos mecanismos físicos do caso do metal de Weyl, porém, com algumas particularidades. Portanto, para evitar uma repetição de conteúdo, apresentamos uma descrição geral do trabalho realizado em conjunto com a metodologia e a versão de acesso livre do artigo publicado no Anexo A.1.

7.1.1 Descrição geral

Considerando a introdução apresentada sobre o grafeno bicamada torcido na seção 1.2, nós propusemos um modelo teórico com os padrões de super-rede de Moiré com uma configuração inicial de empilhamento do tipo AB, com o propósito de analisar estados moleculares com a adição de impurezas de Anderson no

sistema. Vale ressaltar que consideramos dois valores de torção entre as folhas de grafeno, sendo elas $\theta = 1.07°$ (regime fora do ângulo mágico) e $\theta = \theta_M = 1.08°$ (ângulo mágico). Observamos a formação dos estados moleculares em ambos os regimes. Na sequência, realizamos a quebra de simetria de inversão do sistema com a aplicação de uma tensão V, tornando-o em um sistema metálico (ver Fig. 1.8(c)). Na fase metálica, identificamos a formação do estado atômico frustrado no regime fora e dentro do ângulo mágico. Entretanto, observamos a formação de um estado atômico frustrado centrado em zero de energia no regime de θ_M com o aumento da tensão aplicada no sistema TBG. Destacamos que esse modo zero mostra-se robusto com a quebra de simetria de inversão.

7.1.2 Metodologia

Como apresentado na seção 6 e tomando como motivação o estudo da formação de estados moleculares no metal de Weyl, utilizamos a expressão que calcula a densidade de estados induzidas no hospedeiro pela impureza, definida como

$$\delta\rho_{jl}(\omega) = -\frac{1}{\pi v_0^2}\sum_{\xi\xi'\sigma}\mathrm{Im}\left\{\Sigma_\xi(\omega)\,\tilde{\mathcal{G}}_{d_{j\sigma}d_{l\sigma}}(\omega)\,\Sigma_{\xi'}(\omega)\right\}, \tag{7.1}$$

onde $\tilde{\mathcal{G}}_{d_{j\sigma}d_{l\sigma}}(\omega)$ é a função de Green das impurezas e Σ_ξ é a auto energia. Adotamos os parâmetros do modelo obedecendo à condição de simetria partícula-buraco $2\varepsilon_{dj\sigma} + Uj = 0$, considerando $\varepsilon_{dj\sigma} = -0,01D$ com $D = 1$eV (a energia de cutoff) e $v_0 = 0.1$meV.

Capítulo 8

Conclusão

Ao longo desta tese, estudamos os estados moleculares de impurezas, em particular em um dímero, acoplado ora a um metal de Weyl, ora ao grafeno bicamada torcido. Tais resultados agregam à área de Física da Matéria Condensada de materiais topológicos, no que podemos chamar de ligações químicas topológicas. Separadamente, podemos concluir que:

- Demonstramos a natureza dos estados eletrônicos de impurezas acopladas à um metal de Weyl e sua dependência com o parâmetro Q_0 para a quebra de simetria de inversão. Para valores pequenos, formam-se orbitais moleculares convencionais, mas para valores elevados de Q_0, há uma transição para um estado atômico frustrado. Essa transição introduz o conceito de uma plataforma capaz de alternar entre os estados moleculares convencionais e atômico frustrado.

- Demonstramos um modo de energia zero também atomicamente frustrado, ao considerarmos um dímero, no regime de simetria partícula-buraco, acoplado ao TBG. Ao quebrar a simetria de inversão com a aplicação de uma tensão externa no regime do primeiro ângulo mágico $\theta_M \approx 1,08^\circ$, observamos a fusão dos picos de Hubbard convergindo no ponto de Dirac, formando um modo zero molecular atomicamente frustrado. Em resumo, nossas descobertas apontam que a super-rede de Moiré pode ser considerada uma nova plataforma para estudar ligações moleculares não convencionais via *twistrônica* de grafeno.

Capítulo 9

Impacto e Relevância Científico-Social

O estudo dos semimetais de Dirac-Weyl e do grafeno bicamada torcido tem um impacto significativo no campo da física de materiais e na ciência em geral. Essas áreas de pesquisa têm o potencial de trazer avanços tecnológicos e aplicações práticas, bem como impactos sociais relevantes. Além do trabalho apresentado contribuir com conhecimento científico para possíveis realizações experimentais futuras, também pode enriquecer outros campos, como por exemplo:

Avanços tecnológicos: Os semimetais de Dirac-Weyl e o Grafeno bicamada torcido possuem propriedades eletrônicas particulares e distintas de materiais comumente utilizados em transporte eletrônico, podendo contribuir com o avanço da tecnologia. Tanto os semimetais de Dirac-Weyl quanto o grafeno bicamada torcida têm sido objeto de estudo no campo emergente da computação quântica. Suas propriedades eletrônicas, como apresentado nesta tese, podem ser utilizadas para a possível criação de qubits estáveis e manipuláveis, que são a base da informação quântica.

Educação e formação científica: O estudo desses materiais proporciona oportunidades de aprendizado e desenvolvimento científico para estudantes e pesquisadores. À medida que a pesquisa avança, o conhecimento e as habilidades adquiridas podem ser aplicados em outras áreas científicas e tecnológicas, estimulando o avanço da sociedade como um todo. Além disso, o estudo desses materiais incentiva a formação de cientistas e engenheiros altamente qualificados, que podem impulsionar a inovação e contribuir para o desenvolvimento de tecnologias de ponta em diversos setores da economia.

Capítulo 10

Publicações

Este capítulo apresenta três artigos principais publicados que estão relacionados aos resultados desta tesse:

- Atomic frustrated impurity states in Weyl metals, publicado no *Physical Review B 102, 075120* (2020). (DOI: 10.1103/PhysRevB.102.075120)
- Atomic frustration-based twistronics, publicado no *2D Materials 8, 045038* (2021). (DOI: 10.1088/2053-1583/ac277f)

É importante destacar que o autor deste trabalho teve participação na concepção da ideia, cálculos analíticos e numéricos, discussão e redação da versão inicial dos artigos mencionados. Além disso, também esteve envolvido em análise de dados e discussão nos seguintes artigos adicionais:

- Majorana molecules and their spectral fingerprints, publicado no *Physical Review B 102, 075128* (2020). (DOI: 10.1103/PhysRevB.102.075128)
- Topological charge Fano effect in multi-Weyl semimetals, publicado no *Physical Review B 105, 235135* (2022). (DOI: 10.1103/PhysRevB.105.235135)

Referências Bibliográficas

[1] P. A. M. Dirac, Proc. Roy. Soc. Lond., 117, 610-624 (1928).

[2] Weinberg, S. (2002), The Quantum Theory of Fields, vol. 1, Cambridge University Press, ISBN 0-521-55001-7.

[3] Novoselov, K. S., A. K. Geim, S. V. Morozov, D. Jiang, Y. Zhang, S. V. Dubonos, I. V. Grigorieva, and A. A. Firsov, Science 306, 666 (2004).

[4] K.S. Novoselov, Rev. Mod. Phys. 83, 837 (2011).

[5] N. M. R. Peres, Rev. Mod. Phys. 82, 2673 (2010).

[6] A. H. Castro Neto, F. Guinea, N. M. R. Peres, K. S. Novoselov, and A. K. Geim, Rev. Mod. Phys. 81, 109 (2009).

[7] Y. Marques, A. E. Obispo, L. S. Ricco, M. de Souza, I. A. Shelykh, and A. C. Seridonio, Phys. Rev. B 96, 041112 (2017).

[8] Z. K. Liu, J. Jiang, B. Zhou, Z. J. Wang, Y. Zhang, H. M. Weng, D. Prabhakaran, S.-K. Mo, H. Peng, P. Dudin, T. Kim, M. Hoesch, Z. Fang, X. Dai, Z. X. Shen, D. L. Feng, Z. Hussain, and Y. L. Chen, Nat. Mater. 13, 677 (2014).

[9] J. Feng, Y. Pang, D. Wu, Z. Wang, H. Weng, J. Li, X. Dai, Z. Fang, Y. Shi, and L. Lu, Phys. Rev. B 92, 081306(R) (2015).

[10] P. J. W. Moll, N. L. Nair, T. Helm, A. C. Potter, I. Kimchi, A. Vishwanath, and J. G. Analytis, Nature (London) 535, 266 (2016).

[11] T. Liang, Q. Gibson, M. N. Ali, M. Liu, R. J. Cava, and N. P. Ong, Nat. Mater. 14, 280 (2014).

[12] I. Crassee, R. Sankar, W.-L. Lee, A. Akrap, and M. Orlita, Phys. Rev. Materials 2, 120302 (2018).

[13] Z. K. Liu, B. Zhou, Y. Zhang, Z. J. Wang, H. M. Weng, D. Prabhakaran, S.-K. Mo, Z. X. Shen, Z. Fang, X. Dai, Z. Hussain, and Y. L. Chen, Science 343, 864 (2014).

[14] J. Liu and D. Vanderbilt, Phys. Rev. B 88, 224202 (2013).

[15] X. Wan, A. M. Turner, A. Vishwanath, and S. Y. Savrasov, Phys. Rev. B 83, 205101 (2011).

[16] S. M. Young, S. Zaheer, J. C. Y. Teo, C. L. Kane, E. J. Mele, and A. M. Rappe, Phys. Rev. Lett. 108, 140405 (2012).

[17] S. Murakami, New J. Phys. 9, 356 (2007).

[18] M. M. Vazifeh and M. Franz, Phys. Rev. Letter, 111, 027201 (2013).

[19] A. A. Zyuzin, Si Wu, A. A. Burkov, Phys. Rev B, 85, 165110 (2012).

[20] H.-R. Chang, J. Zhou, S.-X. Wang, W.-Y. Shan, & D. Xiao, Phys. Rev. B 92, 241103 (2015).

[21] H. Weyl, Proc. Natl. Acad. Sci. U.S.A. 15, 323 (1929).

[22] D. Xiao, M.-C. Chang, and Q. Niu, Rev. Mod. Phys. 82, 1959 (2010).

[23] M. Z. Hasan, G. Chang, I. Belopolski, G. Bian, S.-Y. Xu & J.-X. Yin, Nature Reviews Materials 6, 784–803 (2021).

[24] S.-Y. Xu, et al. Science 349 (6248): 613–617 (2015).

[25] B. Q. Lv, et al. Nature Physics 11, 724 EP–{} (2015).

[26] W. N. Mizobata, Y. Marques, M Penha,J. E. Sanches, L. S. Ricco, M. de Souza, I. A. Shelykh and A. C. Seridonio, Phys. Rev. B 102, 075120 (2020).

[27] Y. Marques, W. N. Mizobata, R. S. Oliveira, M. de Souza, M. S. Figueira, I. A. Shelykh, and A. C. Seridonio, Sci. Rep. 9, 8452 (2019).

[28] A. V. Rozhkov, A. O. Sboychakov, A. L. Rakhmanov, F. Nori, Physics Reports, 648, 1-104 (2016).

[29] A. K. Geim and I. V. Grigorieva, Nature 499, 419–425 (2013).

[30] Y. Liu, N. O. Weiss, X. Duan, H.-C. Cheng, Y. Huang and X. Duan, Nature Reviews Materials 16042, 1-17 (2016).

[31] D. Jariwala, T. J. Marks and M. C. Hersam, Nature Materials 16, 170–181 (2017).

[32] Yuan Cao, et al, Nature 556, 80–84 (2018).

[33] C. Xu and L. Balents, Phys. Rev. Lett. 121, 087001 (2018).

[34] B. Dóra, Topological Superconductivity Could be a Twist Away, Physics viewpoint (2018).

[35] V. T. Phong and E. J. Mele, Phys. Rev. Lett. 125, 176404 (2020).

[36] J. M. B. Lopes dos Santos, N. M. R. Peres, and A. H. C. Neto, Phys. Rev. Lett. 99, 256802 (2007).

[37] J. M. B. Lopes dos Santos, N. M. R. Peres, and A. H. C. Neto, Phys. Rev. B 86, 155449 (2012).

[38] A. V. Rozhkov, A. O. Sboychakov, A. L. Rakhmanov, F. Noriae, Phys. Rep. 648 1–104 (2016).

[39] Y. Cao, V. Fatemi, S. Fang, K. Watanabe, T. Taniguchi, E. Kaxiras and P. Jarillo-Herrero, Nature 556, 43–50 (2018).

[40] R. Bistritzer and A. H. MacDonald, PNAS 26, 108 (30) (2011).

[41] Cheng-Cheng Liu, Li-Da Zhang, Wei-Qiang Chen, and Fan Yang, Phys. Rev. Lett. 121, 217001 (2018).

[42] B. Padhi, C. Setty and P. W. Phillips, Nano Lett. 18 6175 (2018).

[43] H. C. Po, L. Zou, A. Vishwanath, and T. Senthil, Phys. Rev. X 8, 031089 (2018).

[44] W. N. Mizobata, et. al. 2D Materials 8, 045038 (2021).

[45] P. W. Anderson. Phys. Rev. 124, 41 (1961).

[46] A. F. Otte, M. Ternes, K. V. Bergmann, S. Loth, H. Brune, C. P. Lutz, C. F. Hirjibehedin, and A. J. Heinrich, Nature Physics \{}textbf{4}, 847 (2008).

[47] Mariana M. Odashima , Beatriz G. Prado , E. Vernek. Rev. Bras. Ensino Fís. 39 (2017).

[48] P. Phillips. *Advanced Solid State Physics*. 2nd edition, Cambridge University Press, 2012. ISBN: 9781139031066

[49] H. Bruus and K. Flensberg. *Many-body Quantum Theory in Condensed Matter Physics: An Introduction*. Oxford Graduate Texts, 2004. ISBN-13: 978-0198566335.

[50] J. Hubbard. Proc. R. Soc. A 276: 238-257 (1963).

[51] H. J. Weber and G. B. Arfken, Essential Mathematical Methods for Physicists, 1nd Edition (Academic Press, 2003).

[52] E.Y. Andrei, et al, Rep. Prog. Phys. 75 056501 (2012).

[53] N. P. Armitage, E. J. Mele, and A. Vishwanath, Rev. Mod. Phys. 90, 015001 (2018).

[54] H. Weng, C. Fang, Z. Fang, B. A. Bernevig, and X. Dai Phys. Rev. X 5, 011029 (2015).

[55] J. Friedel, Nuovo Cimento 7, 287 (1958).

[56] José Tadeu Arantes. *Torção de bicamada de grafeno gera um novo tipo de ligação molecular*. Agencia FAPESP, 16 mai.2022. Disponível em: https://agencia.fapesp.br/torcao-de-bicamada-de-grafeno-gera-um-novo-tipo-de-ligacao-molecular/38624/. Acesso em: 26 jan.2023.

[57] RICCO, Luciano Henrique Siliano. Majorana bound states in hybrid quantum dot-topological superconducting nanowires: detection and applications. Tese de Doutorado, 2020, Universidade Estadual Paulista (UNESP).

Apêndice A

Apêndice: Artigo publicado (versão de acesso livre)

A.1 Atomic frustration-based twistronics

Atomic frustration-based twistronics

W. N. Mizobata,[1] J. E. Sanches,[1] M. Penha,[1] W. C. Silva,[1]
C. A. Carvalho,[1] M. S. Figueira,[2] M. de Souza,[3] and A. C. Seridonio[1,3,*]

[1] *São Paulo State University (Unesp), School of Engineering, Department of Physics and Chemistry, 15385-000, Ilha Solteira-SP, Brazil*
[2] *Instituto de Física, Universidade Federal Fluminense, 24210-340, Niterói, Rio de Janeiro, Brazil*
[3] *São Paulo State University (Unesp), IGCE, Department of Physics, 13506-970, Rio Claro-SP, Brazil*

We theoretically investigate atomic frustrated states in diatomic molecules hosted by the bilayer graphene setup twisted by the first magic angle and with broken inversion symmetry in the Dirac cones of the system mini Brillouin zones. Such states show local spectral features typically from uncoupled atoms, but counterintuitively, they also exhibit nonlocal molecular correlations, which turn them into atomically frustrated. By considering a particle-hole symmetric molecule in the Moiré superlattice length-scale, we reveal distinctly from the metallic Weyl counterparts, a molecular zero mode atomically frustrated at the spectral densities of the dimer's atoms. To this end, a strong metallic phase with a plateau in the density of states established by the broken inversion symmetry, together with pronounced blue and red shifts in the molecular levels, due to the magic angle condition, should occur synergistically with atomic Coulomb correlations. Consequently, an entire collapse of these molecular peaks into a single one atomically frustrated, taking place exactly at the Fermi energy, becomes feasible just by tuning properly opposite gate voltages attached to the graphene monolayers. Therefore, we propose that unusual molecular bindings can be engineered via the twistronics of the bilayer graphene system, in particular, if its metallic phase is fully established.

I. INTRODUCTION

In the twisted bilayer graphene (TBG) system, astonishing experimental findings have revealed delicate interplay between the strong correlated insulating and superconducting states[1, 2]. Consequently, this scenario has stimulated substantial theoretical focus on such a matter[3–14]. Essentially, the TBG setup consists of two stacked graphene monolayers misaligned to each other by a twist angle θ[15–17], from which the band-structure becomes highly dependent. Particular attention should be paid to slight twists, once they yield the Moiré superlattice represented by an effective honeycomb pattern, which is a result from the interference between those found in the graphene monolayers. Amazingly, twist angles are then capable of changing dramatically the underlying Dirac Physics. This is noticed when the Fermi velocity vanishes, in particular, by tuning the twist angles to the so-called magic angles, which lead to flat bands in the domain of low energies, namely, at the corners of the mini Brillouin zones[18–30]. As the TBG system is naturally a platform with a huge number of degrees of freedom, due to an expressive quantity of carbon atoms per unit cell and a long-range lattice parameter for the Moiré superlattice, the determination of the TBG electronic properties constitutes a hard task to perform. In this context, two common theoretical strategies are usually employed to overcome such an issue[21, 29, 30]. The first alternative is based on the continuum model[21, 29], which individually accounts for the Hamiltonians from the misaligned graphene monolayers and that for their interlayer couplings. However, such an approach still exhibits a significant number of energy bands. Unfortunately as a result, the continuum model does not allow a simple description of the system in case of considering impurity atoms. Interestingly enough, as the flat bands are within the low energy domain, excited bands can be safely neglected, if we are interested in the Dirac Physics. As aftermath, Wannier wave functions centered around the AB and BA stacking regions of the Moiré superlattice can be assumed, as a second theoretical strategy[30]. By means of such a procedure, a hexagonal effective lattice emerges to better handle impurity atoms, once the emulation of the TBG is performed by an effective graphene monolayer in the Moiré length-scale. It is worth mentioning that, differently from the continuum model where the pieces of the TBG system are treated separately, in such a superlattice description, the Dirac cones at the corners of the mini Brillouin zones, then wrap up all these parts entirely into a renormalized Fermi velocity, depending upon the twist angle and interlayer couplings[21, 28–30].

Here, based on the framework discussed in Ref.[30], we theoretically analyze the emergence of atomic frustrated states in diatomic molecules, made by two impurity atoms, and hosted by the TBG system. Our proposal of atomic frustration is: it represents a molecular-type behavior in which the correlated constituent atoms of the molecule emulate themselves as isolated from each other. Thus, it characterizes a state that locally, i.e., at the atom sites, seems to be noninteracting, while nonlocally still shows, counterintuitively, a correlated behavior by means of an inter-atomic electronic scattering through the molecular host. In equivalent words, the atomic frustration occurs in a molecule that has the trend to split itself into independent atoms, but it is highly prevented of achieving that by its surrounding environment,

* corresponding author: antonio.seridonio@unesp.br

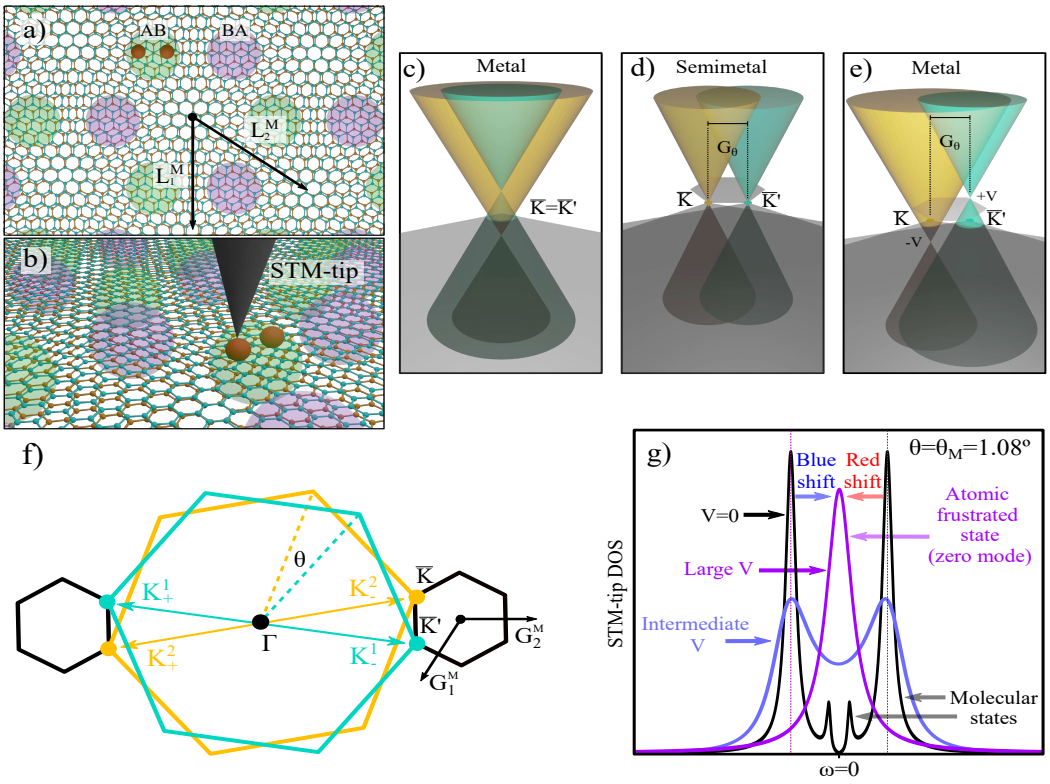

Figure 1. (Color online) Panels a) and f) were prepared after Ref.[30]. Panel (a): Top view for the TBG system and its Moiré superlattice hexagonal pattern for small twist angles θ. The base vectors are $\mathbf{L}_1^{\mathrm{M}}$ and $\mathbf{L}_2^{\mathrm{M}}$. The AB (green) and BA (purple) stacking regions represent the Moiré superatoms and the diatomic molecule, sketched by the pair of red spheres, couples to the AB site. Panel (b): Lateral perspective of panel (a) with an STM-tip above one atom of the dimer. The tip, via the differential conductance, measures the density of states (DOS) of such an atom. Panel (c): Band-structure for the untwisted system for the AA stacking, with coincident Dirac cones at the valley corners $\overline{\mathbf{K}} = \overline{\mathbf{K}'}$ arising from the top and bottom Brillouin zones of the monolayers, respectively. These Dirac points appear shifted in energy, due to the broken inversion symmetry in the metallic phase[28], in analogy to the metallic Weyl counterparts[31]. Panel (d): The twist restores the semimetallic character of the system, but now splits the Dirac points with $\overline{\mathbf{K}} \neq \overline{\mathbf{K}'}$ in momentum space by $G_\theta = \frac{8\pi \sin\frac{\theta}{2}}{3a}$, where a is the lattice parameter of the graphene monolayer. Panel (e): External gate voltages attached to the top $(+V)$ and bottom $(-V)$ monolayers induce the breaking down of the inversion symmetry with metallic character. Panel (f): Mini Brillouin zones with reciprocal base vectors $\mathbf{G}_1^{\mathrm{M}}$ and $\mathbf{G}_2^{\mathrm{M}}$, arising from the twist between the top (1) and bottom (2) Brillouin zones of the graphene monolayers, which have as valley corners $\mathbf{K}_+^1, \mathbf{K}_-^1, \mathbf{K}_+^2$ and $\mathbf{K}_-^2$. Panel (g): Key finding of this work: for the first twist magic angle $\theta = \theta_M = 1.08^\circ$, a crossover in the particle-hole symmetric profile in the spectral DOS for the dimer's atoms is observed. It evolves from a pattern with ordinary molecular states (black lineshape) towards that characterized by a molecular single zero mode ($\omega = 0$) (purple lineshape), which is atomically frustrated [see Fig.3]. This zero mode is the aftermath of the merge between the ordinary molecular states, which is due to the blue and red shifts enhancement of their resonant peak positions, in particular, upon increasing the breaking down of the inversion symmetry of the Dirac cones located at the mini Brillouin zone.

which should be of Weyl-metallic nature to emerge[31]. It means that just a pair of Dirac cones, with or without time-reversal symmetry broken, is not enough to provide the requirements to form the atomically frustrated state. We call the attention that these cases correspond to Weyl and Dirac semimetals, respectively, which show a pseudogap at the Fermi energy as their primary fingerprint. In case of breaking time-reversal symmetry, the Dirac point of this pair formed by two coincident Weyl nodes with opposite chiralities, then splits into resolved ones in momenta, but still degenerate in energy. Particularly, this operation preserves, as expected, the system inversion symmetry invariance and gapped features. In contrast, if these Weyl nodes minimally move, keeping or not the same momenta, in opposite directions in energy axis, i.e., showing blue and red shifts, which can be accomplished by breaking the inversion symmetry, the band-structure under this change, distinctly, becomes gapless. For atomic frustration, a metallic finite density of states at the Fermi energy (pseudogap closing) assisted by two Weyl nodes with opposite chiralities lifted in energy, at last, constitutes the cornerstone of the proposed state. Thus, due to this frustration in breaking the chemical bound of this state with atomic-

like features, it is termed as a molecular state atomically frustrated. To this end, we consider the setup sketched in Fig.1(a), in particular, settled to the well-known first twist magic angle $\theta = \theta_M = 1.08^{\circ}$ [30] and with broken inversion symmetry in the Dirac cones, which reside in the system band-structure [Fig.1(e)]. This scenario, indeed, approaches the corresponding present in the Weyl metals, as demonstrated in Ref.[31]. In the latter, a crossover can be observed from the ordinary molecular bonding and antibonding states, typically from the semimetallic Dirac phase[32, 33], changing to atomic frustrated ones, upon breaking the inversion symmetry. Consequently, this characteristic then allows the system to enter into the Weyl metal phase[31]. Simultaneously, atomic frustrated states are revealed as very intriguing, once locally they seem to behave as those from noninteracting atoms, but counterintuitively, nonlocally they are still bounded as molecular states. Thus, distinctly from the metallic Weyl counterparts, atomic frustrated states in our proposal, have the advantage of being completely tunable, in particular, by twist angles and opposite gate voltages applied to the graphene monolayers. These gate voltages are indeed, employed just to break the inversion symmetry in the Dirac cones and close the pseudogap of the system, in order to produce a metallic phase [Fig.1(e)], where the density of states is finite at the Fermi level. By placing the twist at the first magic angle condition, in parallel to the pseudogap closing mechanism previously reported in Weyl metals, here we observe that the molecular levels suffer strong renormalization characterized by blue and red shifts, respectively for levels below and above the Fermi energy. Thus, upon increasing the gate voltages, in the case of the on-site Coulomb interactions present at the impurity atoms, the graphene Moiré superlattice then mediate the connection between these dimer's atoms, just in order to glue them exclusively through itself and build the molecule. As aftermath, the aforementioned frequency dependent shifts in these levels, lead to a collapse of the ordinary molecular states into a single peak [Fig.1(g)]. This merging occurs at the Fermi energy (zero mode) for particle-hole symmetric molecules and exhibits the atomic frustration character. We clarify that we designate our impurity dimer by "particle-hole symmetric molecule" in the entire text, just to label the regime where the molecular energy levels become symmetrical to the Fermi level ($\omega = 0$). By introducing the molecule with charge mirror symmetry, we report here a phenomenon nonexistent in Weyl metals[31], which arise from Dirac semimetals and exhibit broken inversion symmetry. Particularly, the TBG nearly flat band Physics, characterized by an extremely low Fermi velocity, then rules the formation of a zero mode atomically frustrated, specially at a sweet spot, namely, the one given by the magic angle. For such a special band-structure, and consequently, different from Weyl metals[31], where flat bands are lacking, here the system self-energy affected by the twist, strongly renormalizes the energy spectrum of the impurity atoms, leading to particle-hole symmetric zero mode. As aftermath, this atomically frustrated state rises, specially due to its particle-hole symmetry characteristic, as a promising candidate to a Majorana bound state (MBS), which has topological protection[34, 35]. As MBSs are considered the holy grail for the realization of perfect fault-tolerant topological quantum computing[34, 35], the emergence of zero modes in TBG with atomic dimers at magic angle, is expected to stimulate more exploration and future works covering this subject. Therefore, our results introduce the twistronics of the bilayer graphene system, as an approach to perform unusual molecular bindings in condensed matter platforms.

II. THE MODEL

The Hamiltonian of the TBG system, within the theoretical framework of Ref.[30] and sketched in Figs.1(a)-(b), then follows the Anderson-like Hamiltonian[36], i.e.,

$$\mathcal{H} = \sum_{\mathbf{k}\xi\sigma} \psi^{\dagger}_{\mathbf{k}\xi\sigma} H_{\rm TBG}(\mathbf{k}+\mathbf{K}_{\xi})\psi_{\mathbf{k}\xi\sigma} + \sum_{j\sigma} \varepsilon_{dj\sigma} d^{\dagger}_{j\sigma} d_{j\sigma} + \sum_{j} U_j d^{\dagger}_{j\uparrow} d_{j\uparrow} d^{\dagger}_{j\downarrow} d_{j\downarrow} + V_{AB} \sum_{j\sigma} (f^{\dagger}_{0\sigma} d_{j\sigma} + \text{H.c.}). \quad (1)$$

The first term in Eq.(1) is the low energy Hamiltonian $H_{\rm TBG}(\mathbf{k}+\mathbf{K}_{\xi}) = \hbar\tilde{v}_F(\xi\sigma_x, \sigma_y)\cdot\mathbf{k} + \xi\sigma_0 V$ for the pristine TBG, with $\hbar$ as the reduced Planck's constant and valley indexes $\xi = \pm 1$ for the Dirac points $\overline{\mathbf{K}} = \mathbf{K}_{\xi=-1}$ and $\overline{\mathbf{K}'} = \mathbf{K}_{\xi=+1}$ at the corners of the mini Brillouin zone depicted in Figs.1(c)-(f). The first part of $H_{\rm TBG}(\mathbf{k}+\mathbf{K}_{\xi})$ describes the setup within the length-scale of the Moiré superlattice, which is the result from the interference pattern due to the misalignment θ between the graphene monolayers. Particularly, the emergent hexagonal lattice in real space, i.e., the Moiré superlattice, is constituted by the AB and BA spots, where distinct stacking regions made by clusters of carbon atoms appear depicted by green and purple delimiting spheres, respectively in Figs.1(a)-(b). As such stacking spots resemble the sites where carbon atoms sit at sublattices A and B of graphene monolayer, thus constituting the basis for the unit cell, these AB and BA regions do similarly, but for the supercell from the Moiré superlattice, which relies on a much larger length-scale. Additionally, as Wannier orbitals are constructed around carbon atoms at sublattices A and B in single graphene to perform the model tight-binding analysis, analogously, corresponding orbitals are also taken into account for the TBG system, but with respect to the AB and BA centers of the Moiré superlattice[30]. Thus, following the employment of the prefix "super" in this context, we then make the extrapolation of such a concept to AB and BA spots, where Wannier orbitals are centered, in such a way that hereafter, for a sake of simplicity, we are free to label them as superatoms, in contrast to ordinary carbon atoms from the unit cell of a single graphene sheet, which differently,

has a much smaller length-scale. The superlattice in real space is characterized by the primitive unit vectors $\mathbf{L}_1^{\mathrm{M}}$ and $\mathbf{L}_2^{\mathrm{M}}$, which define the twist angle-dependent unit cell area $\Omega_\theta = |\mathbf{L}_1^{\mathrm{M}} \times \mathbf{L}_2^{\mathrm{M}}| = \frac{\sqrt{3}a^2}{8(\sin\frac{\theta}{2})^2}$ [21, 28–30]. The lattice model then corresponds to an effective graphene monolayer, with renormalized Fermi velocity given by

$$\tilde{v}_F = \frac{v_F\left(\hbar^2 v_F^2 G_\theta^2 - 3w_{AB}^2\right)}{3w_{AA}^2 + 3w_{AB}^2 + \hbar^2 v_F^2 G_\theta^2}, \tag{2}$$

which according to band-structure calculations reveal the existence of linear dispersion relations at the corners $\overline{\mathbf{K}}$ and $\overline{\mathbf{K}'}$, thus giving support to our adopted theoretical framework[30]. For $\tilde{v}_F$, we have $v_F \sim \frac{c}{300}$ the bare Fermi velocity for the graphene monolayer (c is the speed of light) and $G_\theta = \frac{8\pi\sin\frac{\theta}{2}}{3a}$ the distance in momentum space between the aforementioned Dirac points. Particularly in Fig.1(c) $\overline{\mathbf{K}} = \overline{\mathbf{K}'}$, we then have the untwist system with the AA stacking, which corresponds to a metallic-type structure[28]. The AA stacking bilayer arrangement is ideal for the emergence of the atomic frustrated states, once metallic band-structure features from this system, resemble those from Weyl metals[31]. However, the former is energetically unlikely to engineer from a genuine point of view[28]. Astonishingly, it is still feasible, if we perform a twist and break the inversion symmetry, in particular, in the Bernal-type stacking, which is instead, energetically favorable. This appears in Fig.1(e) and is in perfect agreement with Ref.[29], where the authors show that the electronic parabolic dispersion of the Bernal stacking[28], surprisingly, then turns into linear under twist and without inversion symmetry, just by applying opposite gate voltages to graphene sheets. It means that our findings do not depend on the AA stacking to manifest. Hence, our choice to show its band-structure at Fig.1(c), just highlights that this ideal metallic phase is entirely accomplishable by bilayer graphene twistronics and gate microscopy, since we begin with the bilayer graphene in Bernal stacking[29]. The lattice parameter for the graphene monolayer is $a = \frac{\hbar v_F}{2135.4\mathrm{meV}}$, $w_{AB} = 97.5$meV and $w_{AA} = 79.7$meV are the AB and AA hopping terms, respectively and σ_x, σ_y the Pauli matrices. The first twist magic angle condition is obtained from $\hbar^2 v_F^2 G_\theta^2 = 3w_{AB}^2$ in Eq.(2), once it leads to the flat band characterized by $\tilde{v}_F = 0$, giving rise to $\theta = \theta_M = 1.08^\circ$. Then, $H_{\mathrm{TBG}}(\mathbf{k} + \mathbf{K}_\xi)$ is the momentum representation of the tight-binding model with Wannier orbitals centered at the AB and BA superatoms[30], characterized by the spinor $\psi^\dagger_{\mathbf{k}\xi\sigma} = (\ \psi^\dagger_{AB\mathbf{k}\xi\sigma}\ \ \psi^\dagger_{BA\mathbf{k}\xi\sigma}\ )$ describing the electronic states by the operators $\psi_{AB\mathbf{k}\xi\sigma}$ and $\psi_{BA\mathbf{k}\xi\sigma}$, with wave vector $\mathbf{k}$, valley index ξ and spin σ. Additionally, the term $\xi\sigma_0 V$ in $H_{\mathrm{TBG}}(\mathbf{k} + \mathbf{K}_\xi)$, with σ_0 being the identity matrix, is put to break the inversion symmetry of the Dirac cones. This breaking can be performed by applying opposite top and bottom gate voltages $\pm V$ to the graphene monolayers. Such a demonstration can be found in Refs.[29, 30] and leads to the closing of the system pseudogap, driving the TBG arrangement to a metallic phase [Fig.1(e)]. We shall see that atomic frustrated states become feasible in such a regime, as demonstrated for Weyl metals[31], where the chirality degree of freedom plays the role of the current valley index. The operators $d^\dagger_{j\sigma}, d_{j\sigma}$ describe the electronic states of the individual impurity atoms ($j = 1, 2$) (red spheres within the AB site depicted in Figs.1(a)-(b)) with single-particle energies $\varepsilon_{dj\sigma}$ and the on-site Coulomb correlation energies U_j. The term $V_{AB} = v_0$ is the coupling strength between the AB site and the dimer's atoms. We would like to highlight that we extrapolate the use of the concept of the dimer word, which here still represents the diatomic molecule itself, even in the absence of a direct hopping between its constituent atoms, as it occurs in the current theoretical framework. Contrasting with the standard molecular bindings, which are defined in terms of this tunneling term, we then reveal that the considered impurity atoms of the system, distinctly, connect to each other through the host, in particular, via the AB site of the superlattice depicted in Figs.1(a)-(b). It is worth mentioning that we strictly follow both Ref.[30] and its Supplementary Material, in which the grounds for sustaining impurities placed at AB sites (or BA equivalently) in Moiré superlattice, appear well-established. Indeed, such impurities differ completely from those ordinary placed above isolated carbon atoms in single graphene sheet. According to tight-binding calculations, in particular for low twist angles and energies, the system Wannier orbitals around AB and BA sites, do not exhibit maximum localization on themselves. Instead, a three-peak localization at the triangle corners made by neighboring hexagonal centers (hollow sites) is revealed, as depicted in Figs.2(b)-(c) from Ref.[30]. Hence, we should be aware that impurities with sizes of carbon atoms atop these hollow centers, will overlap on equal footing, inevitably, to both Wannier orbitals. However, in order to catch preferably just one set of these wave-functions, in such a way that AB sites become energetically favorable to host impurities, one should, as pointed out in Supplementary Material from Ref.[30], engineer impurities bigger than carbon atoms, but still within the Moiré superlattice length-scale. Thus, according to Figs.2(b)-(c) from Ref.[30], by sitting large impurities at one AB site, their wave-functions overlap stronger with this spot, where the Wannier orbital has a higher amplitude, with respect to Wannier orbitals from the nearest three surrounding BA sites, which at this AB site, show instead, a lower amplitude and then, overlap with the impurities, as aftermath, in a much weaker strength. By this manner, we can safely describe the hybridization between the AB site and impurities by the fermionic field operator given by

$$f_{0\sigma} = \sum_{\mathbf{k}\xi} \psi_{AB\mathbf{k}\xi\sigma}. \tag{3}$$

Under these assumptions, we propose that these two large impurities of the dimer, could be designed by making

atomic clusters, similarly to Ref.[37]. By this reason, we expect that this experimental approach can engineer, in the future, proper impurities for the Moiré superlattice in TBG, provided that a given chemical element of such, is correctly considered. Hence, such an approach in Ref.[37] rises as promising and deserves extra exploration for the realization of our current theoretical proposal. Particularly, the particle-hole symmetric regime, will be crucial to define zero modes, as we will see later on, as atomic frustrated states. Thus, the experimental challenge consists of extrapolating the technique to TBG system, taking into account cluster sizes now bigger than carbon atoms and within the Moiré superlattice length-scale. This assumption can be safely adopted, once in the length-scale of the graphene monolayers the impurity atoms are assumed to be far apart, in such a way that the overlapping between the wave functions from this pair of atoms vanishes. However, in the Moiré superlattice length-scale, these impurities are close enough and locally coupled to the AB site via $f_{0\sigma}$. It means that as the impurity atoms perceive the superlattice as their host instead of the graphene monolayers individually, we are still free to call this pair of impurities by dimer's atoms, once this dimer stays well-established by the superlattice environment. Thus, we can solely focus on this inter-atomic mediation afforded by the Moiré superlattice, which is indeed the cornerstone to provide molecular bindings in the TBG system. Additionally, we shall see later on that such a host-assisted molecular binding, as a matter of fact, will be of capital relevance to analyze the molecular correlation function.

The spectral features of the dimer's atoms can be extracted from their Density of States (DOS) $\rho^{\sigma}_{jj}(\omega) = -\frac{1}{\pi}\mathrm{Im}[\tilde{\mathcal{G}}_{j\sigma|j\sigma}(\omega)]$ $(j = 1, 2)$, where $\tilde{\mathcal{G}}_{j\sigma|j\sigma}(\omega)$ is the Green's function (GF) in energy domain ω. This DOS, via differential conductance measurements, can be detected by an STM-tip (*Scanning Tunneling Microscope*-tip)[38, 39] placed above the j$^{\mathrm{th}}$ atom of the dimer. To obtain such, we first define this quantity in time domain as $\mathcal{G}_{j\sigma|j\sigma}(t) = -\frac{i}{\hbar}\theta(t) < \{d_{j\sigma}(t), d^{\dagger}_{j\sigma}(0)\} >_{\mathcal{H}}$ and later on, apply to it the time-Fourier transform, in particular with the Hubbard-I approximation[40] [see the Appendices], which gives

$$\tilde{\mathcal{G}}_{j\sigma|j\sigma}(\omega) = \frac{\lambda^{\bar{\sigma}}_{j}}{g^{-1}_{j\sigma|j\sigma}(\omega) - \lambda^{\bar{\sigma}}_{j}\Sigma_0(\omega)g_{l\sigma|l\sigma}(\omega)\lambda^{\bar{\sigma}}_{l}\Sigma_0(\omega)}, \tag{4}$$

where $\bar{\sigma} = -\sigma$, $j \neq l$,

$$g_{j\sigma|j\sigma}(\omega) = \frac{1}{\omega - \varepsilon_{dj\sigma} - \Sigma_0(\omega)} \tag{5}$$

is the single-atom noninteracting GF,

$$\lambda^{\sigma}_{j} = 1 + \frac{U_j}{g^{-1}_{j\bar{\sigma}|j\bar{\sigma}}(\omega) - U_j}\langle n_{j\sigma}\rangle \tag{6}$$

is the spectral weight,

$$\langle n_{j\sigma}\rangle = -\frac{1}{\pi}\int_{-D}^{+D} n_{_F}(\omega)\mathrm{Im}[\tilde{\mathcal{G}}_{j\sigma|j\sigma}(\omega)]d\omega \tag{7}$$

is the atom occupation, D is the energy cutoff and $\Sigma_0(\omega) = \sum_{\xi}\Sigma^{\xi}_0(\omega)$ the self-energy given by

$$\Sigma^{\xi}_0(\omega) = \frac{v^2_0\Omega_\theta}{4\pi\hbar^2\tilde{v}^2_F}(\omega_\xi \ln\frac{\omega^2_\xi}{|D^2 - \omega^2_\xi|} - i\pi|\omega_\xi|), \tag{8}$$

with $\omega_\xi = \omega - \xi V$. We call attention that $-\mathrm{Im}\Sigma_0(\omega)$ contains the Moiré superlattice density of states with a pseudogap at the Fermi level $\omega = 0$ and $V = 0$. However, due to $V \neq 0$ in ω_ξ, the $-\mathrm{Im}\Sigma^{\xi}_0(\omega)$ and $\mathrm{Re}\Sigma^{\xi}_0(\omega)$ quantities, as functions of ω for the valley indexes $\xi = +1$ and $\xi = -1$, show blue and red shifts in their profiles, respectively. Particularly with $V \neq 0$, the pseudogap closes in $-\mathrm{Im}\Sigma_0(\omega)$ and a metallic plateau takes place, with a finite density of states around the Fermi energy. Concerning the explicit form of Eq.(4), we can predict in our system, the appearance of bonding and antibonding molecular states. Before to perceive how they emerge, let us assume the impurity atoms decoupled from each other, which corresponds to impose $\lambda^{\bar{\sigma}}_{j}\Sigma_0(\omega)g_{l\sigma|l\sigma}(\omega)\lambda^{\bar{\sigma}}_{l}\Sigma_0(\omega) = 0$ in Eq.(4), just in order to reveal spectrally the decoupled behavior $[\tilde{\mathcal{G}}^{\mathrm{dec}}_{j\sigma|j\sigma}(\omega)]$ of such atoms in $\rho^{\sigma}_{jj}(\omega)$ $(j = 1, 2)$. Under this assumption, we recover the well-established GF for the Hubbard-I approximation in the single atom problem[40]:

$$\tilde{\mathcal{G}}^{\mathrm{dec}}_{j\sigma|j\sigma}(\omega) = \frac{1 - \langle n_{j\bar{\sigma}}\rangle}{\omega - \varepsilon_{dj\sigma} - \Sigma_0(\omega)} + \frac{\langle n_{j\bar{\sigma}}\rangle}{\omega - \varepsilon_{dj\sigma} - U_j - \Sigma_0(\omega)}, \tag{9}$$

where we recognize the two bare (atomic) poles $\varepsilon_{dj\sigma} < 0$ and $\varepsilon_{dj\sigma} + U_j > 0$, which in the presence of an electronic reservoir, namely, our Moiré superlattice, are converted into bands, with peak positions and widths being renormalized and broadened by $\mathrm{Re}\Sigma_0(\omega)$ and $-\mathrm{Im}\Sigma_0(\omega)$, respectively. Particularly for large twist angles $\theta >> \theta_M$, let us say for instance $\theta = 13^{\circ}$ and $\theta = 30^{\circ}$, just to illustrate our goal here, we astonishingly reveal $\tilde{v}_F \to v_F$ and $\Sigma_0(\omega) \to 0$ from Eqs.(2) and (8), respectively. This turns out when the interlayer coupling for graphene monolayers approaches ideal suppression, once the fingerprint of such relies on recovering the pristine Fermi velocity v_F[28]. Consequently, the Moiré superlattice-impurity hybrid system picture of Fig.1(a) breaks down and impurities show Dirac-delta like-behavior, i.e., $\rho_{jj}(\omega) \approx \delta(\omega - \varepsilon_{dj\sigma}) + \delta(\omega - \varepsilon_{dj\sigma} - U)$, typically for isolated atomic states. In this regime, twist angles and gate voltages, as expected, play no role to sustain molecular bindings, clearly due to the scenario very close to perfect decoupled impurities and isolated graphene sheets. By turning-on the inter-atomic correlation by keeping the term $\lambda^{\bar{\sigma}}_{j}\Sigma_0(\omega)g_{l\sigma|l\sigma}(\omega)\lambda^{\bar{\sigma}}_{l}\Sigma_0(\omega) \neq 0$ in Eq.(4), the resonant level $\varepsilon_{dj\sigma} < 0$ $(\varepsilon_{dj\sigma} + U_j > 0)$ splits into molecular levels, known as bonding and antibonding states. These

states are still ruled by the self-energy $\Sigma_0(\omega)$, as we shall see. It is worth mentioning that our central finding relies on such a quantity, namely, the self-energy $\Sigma_0(\omega)$, in particular at $\theta = \theta_M = 1.08^\circ$ and with $V \neq 0$, together with the parameter $\lambda_j^{\bar{\sigma}}$, which is dependent on the on-site Coulomb interaction U_j. In this case, when the particle-hole $2\varepsilon_{dj\sigma} + U_j = 0$ constraint is fulfilled, the splittings of the Hubbard bands around $\varepsilon_{dj\sigma} < 0$ and $\varepsilon_{dj\sigma} + U_j > 0$, then become suppressed in $\rho_{jj}^{\sigma}(\omega)$ $(j = 1, 2)$ upon increasing V, as illustrated in Fig.1(g), with a single peak at the Fermi level as a zero mode. This occurs, as we shall see, due to the strong renormalization of the molecular levels arising from $\mathrm{Re}\Sigma_0(\omega)$, which leads to blue and red shifts in the split bands $\varepsilon_{dj\sigma} < 0$ and $\varepsilon_{dj\sigma} + U_j > 0$, respectively. Thereafter, the molecular levels collapse into a single one [Fig.1(g)]. This can be achieved by choosing $2\varepsilon_{dj\sigma} + U_j = 0$ in the model as stated previously, and verified in its spectral analysis by $\rho_{jj}^{\sigma}(\omega) = \rho_{jj}^{\sigma}(-\omega)$. Such even-parity feature is a straight consequence of this particular Hamiltonian, which is invariant under a standard particle-hole transformation[41], characterized by the half-filling occupation $\langle n_{j\bar{\sigma}} \rangle = 1/2$. Thus, due to this charge mirror symmetry, we naturally adopt the term "particle-hole symmetric molecule" for the dimer's atoms. However, if the BG system from the experimental framework, instead of being prepared in suspended geometry and within a high-vacuum chamber, upon considering, the typical SiC substrate, as the BG platform, it can introduce a doping level in the entire system spectrum[42]. As aftermath, it will compromise the particle-hole symmetry, due to the lifting of the Dirac point and Fermi level degeneracy[42], thus yielding $\langle n_{j\bar{\sigma}} \rangle \neq 1/2$ and a single peak state off the zero mode. Despite such a contamination, the recovery of this degeneracy becomes feasible, just by controlling nitrogen dopants on SiC. As a result, these dopants lead to electron-lack puddles in graphene, thus decreasing the original doping by approaching the Fermi level towards the Dirac point[42]. As pointed out in Ref.[43], instead of doping the substrate as in Ref.[42], n-type or p-type doping techniques performed directly in graphene, similarly, could rule the system particle-hole symmetry. Thus, for a given doping and slight twist, the $2\varepsilon_{dj\sigma} + U_j = 0$ situation could be, in principle, achieved as well, giving rise to a zero mode at magic angle. Intuitively, with this single peak, we naturally infer that the molecule is dissociated, once the splittings of the atomic levels are absent in $\rho_{jj}^{\sigma}(\omega)$ $(j = 1, 2)$. However, in order to put such an usual statement to the test, we should focus on the molecular correlation function $\delta\rho_{jl}(\omega)$, namely, $\sum_{jl} \delta\rho_{jl}(\omega) = -\frac{1}{\pi}\mathrm{Im}[\tilde{\mathcal{G}}^{\mathrm{corr}}(\omega)]$ $(j \neq l = 1, 2)$, which is determined from the time-Fourier transform of the GF $\mathcal{G}^{\mathrm{corr}}(t) = -\frac{i}{\hbar}\theta(t) < \{f_{0\sigma}(t), f_{0\sigma}^{\dagger}(0)\} >_{\mathcal{H}}$. As a result, we find

$$\delta\rho_{jl}(\omega) = -\frac{1}{\pi v_0^2} \sum_{\xi\xi'\sigma} \mathrm{Im}[\Sigma_0^{\xi}(\omega)\tilde{\mathcal{G}}_{j\sigma|l\sigma}(\omega)\Sigma_0^{\xi'}(\omega)], \quad (10)$$

expressed in terms of the GF

$$\tilde{\mathcal{G}}_{j\sigma|l\sigma}(\omega) = g_{j\sigma|j\sigma}(\omega)\lambda_j^{\bar{\sigma}}\Sigma_0(\omega)\tilde{\mathcal{G}}_{l\sigma|l\sigma}(\omega), \quad (11)$$

which in time domain is defined by $\mathcal{G}_{j\sigma|l\sigma}(t) = -\frac{i}{\hbar}\theta(t) < \{d_{j\sigma}(t), d_{l\sigma}^{\dagger}(0)\} >_{\mathcal{H}}$ and accounts for the interference processes between the atoms j and l $(j \neq l)$ through the Moiré superlattice, in particular, assisted by the on-site Coulomb correlation U_j within the parameter $\lambda_j^{\bar{\sigma}}$. Thus, if nonlocally $\delta\rho_{jl}(\omega)$ is finite for $j \neq l$, despite the local absence of splittings in the atomic levels for $\rho_{jj}^{\sigma}(\omega)$ $(j = 1, 2)$, we will see that the dimer's atoms, then look like as free atoms individually, but they still build the molecule. In this scenario, we find an unusual molecular binding, which we introduce as atomically frustrated.

III. RESULTS AND DISCUSSION

In what follows, we adopt model parameters obeying the particle-hole symmetric condition $2\varepsilon_{dj\sigma} + U_j = 0$, by considering $\varepsilon_{dj\sigma} = -0.01D$ with $D = 1$eV (the energy cutoff) and $v_0 = 0.1$meV. Naturally, once the region above the Fermi level is the mirror for the corresponding below, the profiles presentation for $\rho_{jj}^{\sigma}(\omega)$ $(j = 1, 2)$ in this domain is needless. It means that the Hubbard bands around $\varepsilon_{dj\sigma} < 0$ and $\varepsilon_{dj\sigma} + U_j > 0$ are equally distant from the Fermi energy and exhibit the same spectral profiles.

In Fig.2, we analyze $\rho_{jj}^{\sigma}(\omega)$ $(j = 1, 2)$ in two scenarios. The first treats the twist angle $\theta = 1.07^\circ$ [Figs.2(a)-(c)], which is off the magic angle condition, while the second is exactly settled to such a point, i.e., $\theta = \theta_M = 1.08^\circ$ [Figs.2(d)-(f)]. Both share an ordinary characteristic when the inversion symmetry is preserved ($V = 0$) in the Dirac cones for the mini Brillouin zone: the emergence of the molecular bonding and antibonding states due to the atomic level splitting in $\varepsilon_{dj\sigma} = -0.01D$, as pointed out by the rose arrows in Figs.2(a) and (d). Although they have this feature in common, these states are broadened by $-\mathrm{Im}\Sigma_0(\omega)$, whose resonant peak positions depend on $\mathrm{Re}\Sigma_0(\omega)$, both distinctly for each θ. Particularly, $-\mathrm{Im}\Sigma_0(\omega)$ shows a semimetallic pseudogap [Figs.2(a)-I and (d)-I] leading to narrow widths in these states when $\varepsilon_{dj\sigma}$ approaches the Fermi energy, which is the point where this gap opens with the decreasing in the number of density of states. This narrowing then allows to resolve the splitting of $\varepsilon_{dj\sigma} = -0.01D$ into the molecular levels present in $\rho_{jj}^{\sigma}(\omega)$. However, the $\mathrm{Re}\Sigma_0(\omega)$ quantity magnifies differently for $\theta = 1.07^\circ$ and $\theta = \theta_M = 1.08^\circ$ [Figs.2(a)-II and (d)-II] according to the blue ($\mathrm{Re}\Sigma_0(\omega) > 0$) and red ($\mathrm{Re}\Sigma_0(\omega) < 0$) shifts indicated by the vertical arrows for state levels placed below ($\varepsilon_{dj\sigma} < 0$) and above ($\varepsilon_{dj\sigma} + U_j > 0$) the Fermi energy ($\omega = 0$), respectively. Notice that the renormalization from $\mathrm{Re}\Sigma_0(\omega)$ in the levels for $\rho_{jj}^{\sigma}(\omega)$ is stronger when $\theta = \theta_M = 1.08^\circ$, once they are driven closer to the Fermi energy [Fig.2(d)] than in the $\theta = 1.07^\circ$ case, where we

still observe the molecular states around $\varepsilon_{dj\sigma} = -0.01D$ [Fig.2(a)]. As $\mathrm{Re}\Sigma_0(\omega)$ depends on the Fermi velocity inversely, in particular for $\theta = \theta_M = 1.08^\circ$, it increases substantially and displaces strongly with blue (red) shift the molecular negative (positive) peak positions. It is worth citing that $-\mathrm{Im}\Sigma_0^\xi(\omega)$ and $\mathrm{Re}\Sigma_0^\xi(\omega)$ for the valley indexes $\xi = \pm 1$ of the mini Brillouin zone, as we can see in the inset panels from Figs.2(a) and (d), are degenerate when the inversion symmetry is preserved. Interestingly enough, by breaking down such a symmetry with $V \neq 0$, the ordinary molecular profiles in $\rho_{jj}^\sigma(\omega)$ change drastically, once the degeneracy in $-\mathrm{Im}\Sigma_0^\xi(\omega)$ and $\mathrm{Re}\Sigma_0^\xi(\omega)$ quantities is lifted. Their profiles split into blue and red shifts for $\xi = +1$ and $\xi = -1$, respectively [inset panels for Figs.2(b), (c), (e) and (f)]. Particularly in Fig.2(b) [Fig.2(e)], we observe partially (completely) collapse of the molecular states with $V = 0.01D$. The case for Fig.2(b) is ruled exclusively by the blue and red shifts in $-\mathrm{Im}\Sigma_0^\xi(\omega)$ profiles, which close the pseudogap in $-\mathrm{Im}\Sigma_0(\omega)$ and make the molecular states broader, but not enough for the entire collapse. This constitutes a gapless phase of the Moiré superlattice, with a metallic plateau emerging in $-\mathrm{Im}\Sigma_0(\omega)$, whose amplitude defines the broadening of the molecular peaks. This phenomenon has been already observed in the metallic Weyl counterparts, triggered exactly by the pseudogap closing from the semimetallic Dirac phase. It leads to molecular states atomically frustrated[31], in particular off the Fermi energy with the increase of V, as depicted by the resonant peak in Fig.2(c) with $V = 0.03D$. We should remember that, there is also another one in the positive energy domain, due to the existing charge mirror symmetry in the dimer's atoms. However, for $\theta = \theta_M = 1.08^\circ$ and $V = 0.03D$, the strong regime of the vertical blue and red shifts in $\mathrm{Re}\Sigma_0(\omega)$ is enough to allow the complete merge between the molecular peaks into a single resonant structure, in particular, exactly at the Fermi energy [Fig.2(f)]. As a matter of fact, the blue and red shifts in $\mathrm{Re}\Sigma_0(\omega)$ at the inset panels (d)-II, (e)-II and (f)-II from Fig.2 are considered pronounced, due to their enhanced amplitudes, which are up to $\approx 10^{-1}D$, i.e., 10 times greater when compared to the $\theta = 1.07^\circ$ case shown in the inset panels (a)-II, (b)-II and (c)-II of the same figure. Thus, distinctly from the Weyl metal case[31], this single peak still has its origin from the pseudogap closing, but in addition to such a mechanism, in order to become a zero mode, it needs also the one from the strong renormalization of the molecular levels, due to the $\mathrm{Re}\Sigma_0(\omega)$ function. Such a feature then allows the blue and red shifts for the molecular states found below and above the Fermi energy, respectively and inevitably, to a collapsed final state wherein the ordinary molecular peaks are not resolved as earlier [see also the cartoon in Fig.1(g)]. This feature strongly suggests that the atoms from the dimer does not constitute a molecule anymore and can be considered, in principle, decoupled from each other. As a matter of fact, in Fig.3 we will see that such a single peak is not atomic as it seems to be, as pointed out by the on-site spectral function $\rho_{jj}^\sigma(\omega)$ pattern. Surprisingly, such a case is peculiar and it has a molecular nature, as can be ensured by the finite values extracted from the molecular correlation function $\delta\rho_{jl}(\omega)$ $(j \neq l = 1, 2)$ in Eq.(10). This nonlocal quantity then reveals that the molecular binding persists and due to such, we recognize this molecular zero mode as atomically frustrated.

In Fig.3(a) for the first twist magic angle condition $\theta = \theta_M = 1.08^\circ$, we summarize via the $\rho_{jj}^\sigma(\omega)$ color map (in normalized units) as a function of V and ω, the crossover from ordinary molecular states towards a molecular zero mode atomically frustrated. This density plot makes explicit three distinct phases, which we recognize as: I) the weak metallic Moiré phase, where four molecular states can be viewed corresponding to the splittings in the Hubbard bands $\varepsilon_{dj\sigma} < 0$ and $\varepsilon_{dj\sigma} + U_j > 0$, II) the intermediate metallic phase with two atomic frustrated states well established as in Weyl metals[31] and finally, III) the strong metallic Moiré phase, where the molecular zero mode atomically frustrated emerges. Although we have showed in Fig.2(f) that the gate $V = 0.03D$ between the layers affects the energy spectrum of the atomic impurities with the presence of the zero mode when $\theta = \theta_M = 1.08^\circ$, in the $\theta = 1.07^\circ$ case, this single peak does not exist for such a V strength. However, for $\theta = \theta_M = 1.08^\circ$, the zero mode threshold to rise is much lower, i.e., it is given by $V = 0.019D$, as marked at Fig.3(a) in rose color. Such a minor value is expected, since our findings lie within the domains of linear dispersion approximation and nearly flat bands. Thus, to better understand the reason for which the absence of splittings in the atomic levels observed in $\rho_{jj}^\sigma(\omega)$ is considered naive to characterize the dimer's atoms dissociated and the final state as a genuine atomic one, we call attention to the molecular correlation function $\delta\rho_{jl}(\omega)$ $(j \neq l = 1, 2)$ as a function of ω. Notice that in Fig.3(b) for $V = 0$, which corresponds to the split bonding and antibonding molecular levels in Fig.2(d), the $\delta\rho_{jl}(\omega)$ spectral function is finite (red lineshape), as expected for a molecular binding. The same occurs for $V = 0.01D$ (green lineshape) and $V = 0.03D$ (blue lineshape). However, the latter leads to only one single resonant structure at $\omega = 0$ (zero mode) in Fig.2(f), which could give the impression that the atoms become decoupled from each other, turning into authentic atomic states. As $\delta\rho_{jl}(\omega)$ is finite even with $V = 0.03D$, the Moiré superlattice intermediates the connection between the atoms, just in order to sustain the molecular binding. Particularly, this mediation is assisted by the atomic Coulomb interactions U_j, as we can verify in the term $\lambda_j^{\bar{\sigma}}\Sigma_0(\omega)g_{j\sigma|l\sigma}(\omega)\lambda_l^{\bar{\sigma}}\Sigma_0(\omega)$ $(j \neq l = 1, 2)$ for Eq.(4). Its origin arises from the interplay between the fulfilment of the first twist magic angle condition $\theta = \theta_M = 1.08^\circ$ in the presence of Coulomb terms and the breaking down of the inversion symmetry in the Dirac cones by the gate voltage V. To conclude, we analyze in Fig.3(c) how the *quasiparticle* lifetime $\tau(U_j)$[44] for the molecular zero

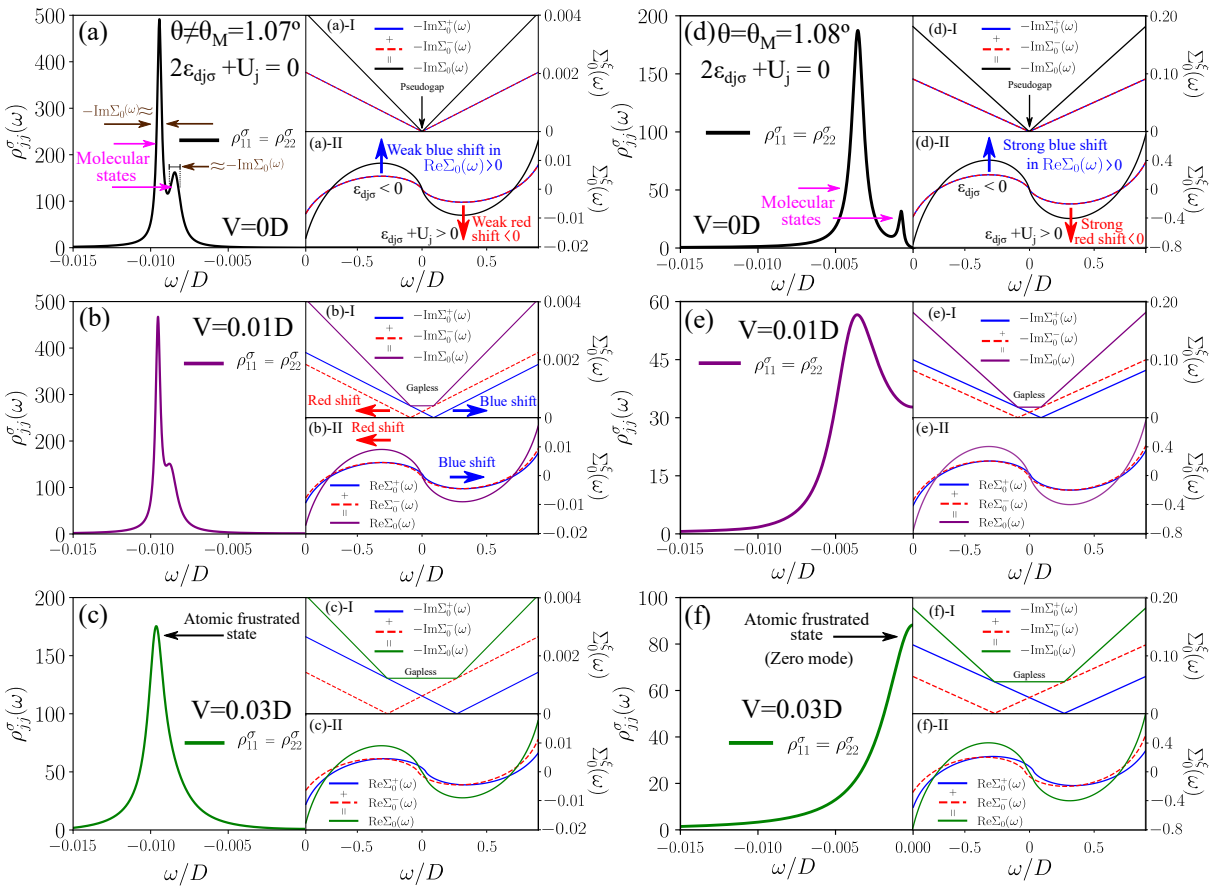

Figure 2. (Color online) Panels (a)-(c): Crossover observed in the spectral density of states $\rho^{\sigma}_{jj}(\omega)$ $(j = 1, 2)$ for the dimer's atoms, with $\varepsilon_{dj\sigma} = -0.01D$ and particle-hole symmetry $(2\varepsilon_{dj\sigma} + U_j = 0)$, as a function of the single particle energy ω in the negative domain, in particular, off the first twist magic angle, i.e., $\theta = 1.07^{\circ}$. Here, we visualize the evolution from the ordinary molecular states (level splitting in $\varepsilon_{dj\sigma}$ into bonding and antibonding states) at panel (a), which are approximately broadened by $-\mathrm{Im}\Sigma_0(\omega)$, via the breaking down of the inversion symmetry by the gate voltage V [panels (b) and (c)], towards the final atomic frustrated state, where the aforementioned level splitting is absent, as depicted at panel (c). Additionally, a second atomic frustrated state exists in the positive energy domain, but it is not shown, due to the aforementioned charge mirror symmetry for the dimer. Notice that the peak in panel (c) is the result of the merge between the molecular peaks from panels (a)-(b), ruled by the pseudogap closing in $-\mathrm{Im}\Sigma_0(\omega)$, which is characterized by a metallic (gapless) plateau [inset panels (b)-I and (c)-I]. The plateau amplitude defines the broadening of the molecular peaks and arises from the blue and red shifts in the profiles for $-\mathrm{Im}\Sigma^{+}_0(\omega)$ and $-\mathrm{Im}\Sigma^{-}_0(\omega)$, respectively. Consequently, the molecular states collapse into a unique resonant state, as in panel (c), but still placed around $\varepsilon_{dj\sigma} = -0.01D$, once the blue and red shifts in $\mathrm{Re}\Sigma_0(\omega)$ are in the weak regime (up to $\approx 10^{-2}D$ according to the right axis of the inset panels (a)-II, (b)-II and (c)-II). Such a single peak is still considered of molecular nature, but with atomic frustration as in the metallic Weyl counterparts[31]. Panels (d)-(f): The corresponding crossover for panels (a)-(c) in the case of the first twist magic angle $\theta = \theta_M = 1.08^{\circ}$. Distinctly from $\theta = 1.07^{\circ}$, beyond the pseudogap closing mechanism in $-\mathrm{Im}\Sigma_0(\omega)$ [panels (e)-I and (f)-I], the blue and red shifts in $\mathrm{Re}\Sigma_0(\omega)$ [panels (d)-II, (e)-II and (f)-II] enter into the strong regime (up to $\approx 10^{-1}D$, i.e., 10 times the $\theta = 1.07^{\circ}$ case), thus also ruling the emergence of the atomic frustrated state. This second mechanism does not manifest in Weyl metals, once the Fermi velocity is not tunable by twist angles. By this manner, the molecular states at negative and positive (not shown) energy positions merge exactly at $\omega = 0$, therefore constituting a molecular zero mode of energy [panel (f)], which is considered atomically frustrated [see Figs.3(a)-(c)], cf. details in the main text.

mode in the atomic frustrated state regime ($V = 0.03D$) changes with the Coulomb interactions U_j. Thus, we restore in the profile of $\rho^{\sigma}_{jj}(\omega)$ the positive energy domain ($\omega > 0$), once the lifetime is inversely proportional to the spectral width $2\Gamma(U_j)$[44], i.e., $\tau(U_j) = \frac{\hbar}{2\Gamma(U_j)}$. Parameterizing by $\varepsilon_{dj\sigma} = -0.01fD$ and $U_j = -2\varepsilon_{dj\sigma}$, we find out that the *quasiparticle* lifetime increases by decreasing f. It means that, hypothetically in the absence of such an interaction ($f = 0$), the dimer's atoms become isolated from the superlattice and the atomic frustrated state disappears, due to the $\rho^{\sigma}_{jj}(\omega) \approx \delta(\omega)$ behavior [panel (c)-I of the same figure]. Therefore, the molecular binding found

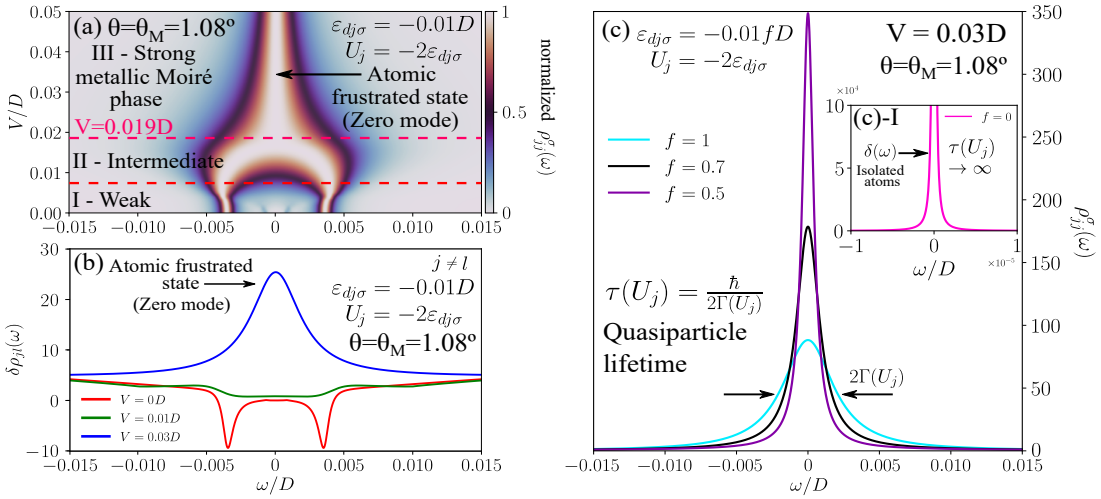

Figure 3. (Color online) Panel (a): Color map of the normalized $\rho^{\sigma}_{jj}(\omega)$ $(j = 1, 2)$ for the dimer's atoms, with $\varepsilon_{dj\sigma} = -0.01D$ and particle-hole symmetry $(U_j = -2\varepsilon_{dj\sigma})$, spanned by V and ω at the first twist magic angle $\theta = \theta_M = 1.08^{\circ}$. A crossover is shown from the ordinary molecular states (I- the weak metallic Moiré phase) triggered by the continuous changing of the V parameter (II- the intermediate metallic Moiré phase), which results in the levels collapse into a single zero mode (III- the strong metallic Moiré phase, with $V = 0.019D$ as the zero mode threshold to emerge). This mode is atomically frustrated, as we shall verify later on. Panel (b): Molecular correlation function $\delta\rho_{jl}(\omega)$ $(j \neq l = 1, 2)$ as a function of ω, with particle-hole symmetry $(U_j = -2\varepsilon_{dj\sigma})$. Finite values of $\delta\rho_{jl}(\omega)$ identify molecular bindings as well-established, due to usual splitting of the atomic level into molecular states, such as the one observed in Fig.2(d) with $V = 0$. However, when this splitting is absent as in Fig.2(f) with $V = 0.03D$, it suggests the decoupling of the atoms from each other and the recovering of an atomic state. Counterintuitively, the correlation $\delta\rho_{jl}(\omega)$ is still finite even in such a situation. It means that locally the dimer's atoms behave, by means of $\rho^{\sigma}_{jj}(\omega)$, as uncoupled atoms due to the spectral single peak characteristic, while its nonlocal behavior $(\delta\rho_{jl}(\omega) \neq 0,\ j \neq l)$ is of molecular nature mediated by the Moiré superlattice, in particular, assisted by the atomic Coulomb interaction (III- strong metallic Moiré phase). For this case, we call this peculiar molecular mode at $\omega = 0$ that seems to be atomic, as a molecular zero mode atomically frustrated. Panel (c): Coulomb interaction (U_j) dependence in the particle-hole symmetric $(\varepsilon_{dj\sigma} = -0.01fD$ and $U_j = -2\varepsilon_{dj\sigma})$ spectral density of states $\rho^{\sigma}_{jj}(\omega)$ $(j = 1, 2)$ for the atomic frustrated state regime $(V = 0.03D)$. We see that the *quasiparticle* lifetime $\tau(U_j) = \frac{\hbar}{2\Gamma(U_j)}$, which is inversely proportional to the spectral width $2\Gamma(U_j)$ of $\rho^{\sigma}_{jj}(\omega)$, increases upon decreasing f. In the inset (c)-I, the limit case with $f = 0$ $(U_j = 0)$ leads to a $\rho^{\sigma}_{jj}(\omega) \approx \delta(\omega)$ behavior. The latter denotes that the dimer's atoms become completely isolated from the host, in such a way that the atomic frustrated state, which should be assisted by the U_j term to exist, quenches.

in this work should be afforded by a finite U_j to exist. Interestingly enough, the Anderson theory on impurity systems[36] predicts spectral densities with single peaks solely in the absence of Coulomb interactions. Such a signature, as we can notice, arises rightly from the Hubbard-I solution, which by imposing $U_j = 0$ in Eq.(9), provides a spectral density with a *Lorentzian* lineshape. However, the molecular zero mode of the atomic frustrated state here reported, which is also a single one resonant peak of a *Lorentzian*, then contrasts with the aforementioned feature and constitutes an exception to this rule. As a matter of fact, the results from Fig.3(c) ensure that such a state is indeed, a strongly correlated metallic state, which emerges at the first twist magic angle condition.

IV. CONCLUSIONS

We have demonstrated that the TBG is a promising candidate to host a molecular zero mode atomically frustrated, upon considering diatomic molecules with charge mirror symmetry. To realize such, in particular, at the first twist magic angle, the TBG system should be driven into a strong metallic phase, which arises from the broken inversion symmetry in the Dirac cones for the emergent mini Brillouin zones of the Moiré superlattice. This can be performed by applying top and bottom opposite gate voltages to the graphene monolayers. By this manner, this configuration leads to an enhancement of the blue and red shifts in the molecular levels, which in the case of considering atomic Coulomb correlations, make the possibility of merging entirely these molecular peaks into a zero mode in the dimer's atoms, just by changing the gate voltages. These tunable states constitute a spectral single peak, which suggests that the atoms are found decoupled from each other. However, the molecular correlation function from the dimer's atoms is still finite in this case, thus revealing the molecular nature of such a binding, which in particular, is mediated by the Moiré superlattice. As a result, this leads then to the concept of atomic frustration in molecules. In summary, our findings point out that the Moiré superlattice can

be considered as a new platform to build unconventional molecular bindings via graphene twistronics.

V. ACKNOWLEDGMENTS

We thank the Brazilian funding agencies CNPq (Grants. Nos. 128919/2021-3, 308410/2018-1, 305668/2018-8 and 302887/2020-2), the São Paulo Research Foundation (FAPESP; Grant No. 2018/09413-0) and Coordenação de Aperfeiçoamento de Pessoal de Nível Superior - Brasil (CAPES) – Finance Code 001.

APPENDICES

We summarize the main mathematical steps to derive the GFs of the dimer's atoms [Eqs.(4) and (11)] and the molecular correlation function [Eq.(10)]. Such evaluations will be performed via the equation-of-motion (EOM) approach on the system GFs[44], in particular, within the Hubbard-I approximation[40].

Appendix A: Helical basis for the TBG Anderson-like Hamiltonian

In order to accomplish the previous announced purpose, we first need to diagonalize the Hamiltonian of the TBG system and later on, express it into the helical basis with right- and left-movers. Thus, by using the spinor $\psi^{\dagger}_{\mathbf{k}\xi\sigma} = (\ \psi^{\dagger}_{AB\mathbf{k}\xi\sigma}\ \ \psi^{\dagger}_{BA\mathbf{k}\xi\sigma}\ )$ in Eq.(1), we begin with

$$\begin{aligned}\mathcal{H} &= \mathcal{H}_{\rm TBG} + \mathcal{H}_{\rm dimer} + \mathcal{H}_{\rm Hyb}\\ &= \sum_{\mathbf{k}\xi\sigma}[\hbar\tilde{v}_F(\xi k_x - ik_y) + \xi V]\psi^{\dagger}_{AB\mathbf{k}\xi\sigma}\psi_{BA\mathbf{k}\xi\sigma} + \text{H.c.}\\ &+ \sum_{j\sigma}\varepsilon_{dj\sigma}d^{\dagger}_{j\sigma}d_{j\sigma} + \sum_{j}U_j d^{\dagger}_{j\uparrow}d_{j\uparrow}d^{\dagger}_{j\downarrow}d_{j\downarrow}\\ &+ \sum_{\mathbf{k}\xi j\sigma} v_0(\psi^{\dagger}_{AB\mathbf{k}\xi\sigma}d_{j\sigma} + \text{H.c.}).\end{aligned} \tag{A1}$$

Now we change to polar coordinates $\hbar\tilde{v}_F(\xi k_x \mp ik_y) = \hbar\tilde{v}_F k\xi e^{\mp i\xi\theta}$, perform the transformations $\psi_{AB\mathbf{k}\xi\sigma} = \frac{1}{\sqrt{2}}[\zeta^{\xi}_{+\sigma}(\mathbf{k}) + \zeta^{\xi}_{-\sigma}(\mathbf{k})]$, $\psi_{BA\mathbf{k}\xi\sigma} = \frac{\xi}{\sqrt{2}}e^{i\xi\theta}[\zeta^{\xi}_{+\sigma}(\mathbf{k}) - \zeta^{\xi}_{-\sigma}(\mathbf{k})]$ and $\sum_{\mathbf{k}} \to \frac{\Omega_\theta}{(2\pi)^2}\int d^2\mathbf{k}$ in the Hamiltonians $\mathcal{H}_{\rm TBG}$ and $\mathcal{H}_{\rm Hyb}$, just to obtain the continuum limit of $\mathbf{k}$ space. Thus, by taking into account all these procedures together, we find

$$\begin{aligned}\mathcal{H}_{\rm TBG} = \sum_{\xi\sigma}\frac{\Omega_\theta}{2\pi}[\int_0^{\infty}\varepsilon_k k dk(&\zeta^{\xi\dagger}_{+\sigma}(\mathbf{k})\zeta^{\xi}_{+\sigma}(\mathbf{k})\\ &- \zeta^{\xi\dagger}_{-\sigma}(\mathbf{k})\zeta^{\xi}_{-\sigma}(\mathbf{k})) + \xi V(\zeta^{\xi\dagger}_{+\sigma}(\mathbf{k})\zeta^{\xi}_{+\sigma}(\mathbf{k})\\ &+ \zeta^{\xi\dagger}_{-\sigma}(\mathbf{k})\zeta^{\xi}_{-\sigma}(\mathbf{k}))],\end{aligned} \tag{A2}$$

with $\varepsilon_k = \hbar\tilde{v}_F k$ and

$$\mathcal{H}_{\rm Hyb} = \sum_{\xi j\sigma}\frac{\Omega_\theta}{2\pi}\int_0^{\infty} k dk\frac{v_0}{\sqrt{2}}(\zeta^{\xi\dagger}_{+\sigma}(\mathbf{k}) + \zeta^{\xi\dagger}_{-\sigma}(\mathbf{k}))d_{j\sigma} + \text{H.c.}. \tag{A3}$$

As we are interested in the low energy Physics of the TBG system, which should be isotropic as expected, we perform an angular plane-wave decomposition of the form $\zeta^{\xi}_{\pm\sigma}(\mathbf{k}) = \frac{1}{\sqrt{k}}[\frac{(2\pi)^2}{\Omega_\theta}]^{\frac{1}{2}}\sum_{m=-\infty}^{\infty}\frac{1}{\sqrt{2\pi}}\ e^{im\theta}\zeta^{m}_{\pm\sigma\xi}(k)$, from where we only catch the contribution of the $m = 0$ state. Later on, we unfold the range of the momenta k from $(0,\infty)$ to $(-\infty,+\infty)$, which allows us to introduce the helical basis $c_{\sigma\xi}(k) = \zeta^{\xi}_{+\sigma}(k)$ for $k > 0$ and $c_{\sigma\xi}(k) = \zeta^{\xi}_{-\sigma}(k)$ for $k < 0$ to describe right- and left-movers, respectively. Consequently, we find an Anderson-like Hamiltonian[36] for the TBG system, which reads

$$\begin{aligned}\mathcal{H} = &\sum_{\xi\sigma}\int_{-\infty}^{+\infty} dk(\varepsilon_k + \xi V)c^{\dagger}_{\sigma\xi}(k)c_{\sigma\xi}(k) + \mathcal{H}_{\rm dimer}\\ &+ \sum_{\xi j\sigma}\int_{-\infty}^{+\infty} dk\mathcal{V}_k(\theta)(c^{\dagger}_{\sigma\xi}(k)d_{j\sigma} + \text{H.c.}),\end{aligned} \tag{A4}$$

where $\mathcal{V}_k(\theta) = \frac{v_0\sqrt{\Omega_\theta|k|\pi}}{2\pi}$ encodes the momentum and twist angle dependent coupling between the impurity atoms and the Moiré superlattice.

Appendix B: The evaluation of the GFs for the dimer's atoms

The EOM approach can be summarized as follows: $\omega^{+}\tilde{\mathcal{G}}_{\mathcal{A}|\mathcal{B}}(\omega) = \{\mathcal{A},\mathcal{B}\} + \tilde{\mathcal{G}}_{[\mathcal{A},\mathcal{H}]|\mathcal{B}}(\omega)$, $\omega^{+} = \omega + i0^{+}$, the time Fourier transform $\tilde{\mathcal{G}}_{\mathcal{A}|\mathcal{B}}(\omega) = \int_{-\infty}^{+\infty} dt\mathcal{G}_{\mathcal{A}|\mathcal{B}}(t)e^{-\frac{i}{\hbar}\omega^{+}t}$ for the energy domain GF $\tilde{\mathcal{G}}_{\mathcal{A}|\mathcal{B}}(\omega)$ and $\mathcal{G}_{\mathcal{A}|\mathcal{B}}(t) = -\frac{i}{\hbar}\theta(t) < \{\mathcal{A}(t),\mathcal{B}^{\dagger}(0)\} >_{\mathcal{H}}$ is the corresponding GF in time domain. To obtain Eqs.(4) and (11), we follow the EOM prescription taking into account Eq.(A4) and show

$$\begin{aligned}(\omega^{+} - \varepsilon_{dj\sigma})\tilde{\mathcal{G}}_{j\sigma|l\sigma}(\omega) &= \delta_{jl} + U_j\tilde{\mathcal{G}}_{j\sigma n_{j\bar{\sigma}}|l\sigma}(\omega)\\ &+ \sum_{\xi}\int_{-\infty}^{+\infty} dk\mathcal{V}_k(\theta)\tilde{\mathcal{G}}_{c_{\sigma\xi}(k)|l\sigma}(\omega),\end{aligned} \tag{B1}$$

with $\mathcal{G}_{j\sigma n_{j\bar{\sigma}}|l\sigma}(t) = -\frac{i}{\hbar}\theta(t) < \{d_{j\sigma}(t)n_{j\bar{\sigma}}(t), d^{\dagger}_{l\sigma}(0)\} >_{\mathcal{H}}$ as a GF of high hierarchy that encodes the on-site Coulomb correlations, with $n_{j\bar{\sigma}} = d^{\dagger}_{j\bar{\sigma}}d_{j\bar{\sigma}}$, while the host-atom mixing GF arises from

$$\tilde{\mathcal{G}}_{c_{\sigma\xi}(k)|l\sigma}(\omega) = \sum_{j'}\frac{\mathcal{V}_k(\theta)}{(\omega^{+} - \varepsilon_k - \xi V)}\tilde{\mathcal{G}}_{j'\sigma|l\sigma}(\omega), \tag{B2}$$

in which $\mathcal{G}_{c_{\sigma\xi}(k)|l\sigma}(t) = -\frac{i}{\hbar}\theta(t) < \{c_{\sigma\xi}(k,t), d^{\dagger}_{l\sigma}(0)\} >_{\mathcal{H}}$. From Eq.(B1), we need to obtain $\tilde{\mathcal{G}}_{j\sigma n_{j\bar{\sigma}}|l\sigma}(\omega)$. As we are not interested in the Kondo regime[41], spin-flip processes can be safely disregarded in the evaluation

of $\tilde{\mathcal{G}}_{j\sigma n_{j\bar{\sigma}}|l\sigma}(\omega)$. Such an assumption consists the main cornerstone of the Hubbard-I approach in decoupling the system of GFs[40]. The Hubbard-I holds at temperatures $T \gg T_K$, where T_K represents the Kondo temperature[41]. Particularly in the calculation of $\langle n_{j\bar{\sigma}} \rangle$ given by Eq.(7) and below, we make explicit that T should not be very high, so that we can safely adopt the Heaviside step function for the Fermi-Dirac distribution $n_{_F}(\varepsilon)$. Thus, by this manner, after successive steps of the EOM, we obtain

$$(\omega^+ - \varepsilon_{dj\sigma} - U_j)\tilde{\mathcal{G}}_{j\sigma n_{j\bar{\sigma}}|l\sigma}(\omega) = \delta_{jl} < n_{j\bar{\sigma}} > + \sum_{\xi} \int_{-\infty}^{+\infty} dk \mathcal{V}_k(\theta) \tilde{\mathcal{G}}_{c_{\sigma\xi}(k) n_{j\bar{\sigma}}|l\sigma}(\omega), \tag{B3}$$

$\mathcal{G}_{c_{\sigma\xi}(k) n_{j\bar{\sigma}}|l\sigma}(t) = -\frac{i}{\hbar}\theta(t) < \{c_{\sigma\xi}(k,t) n_{j\bar{\sigma}}(t), d^{\dagger}_{l\sigma}(0)\} >_{\mathcal{H}}$ and

$$(\omega^+ - \varepsilon_k - \xi V)\tilde{\mathcal{G}}_{c_{\sigma\xi}(k) n_{j\bar{\sigma}}|l\sigma}(\omega) = \sum_{j'} \mathcal{V}_k(\theta) \tilde{\mathcal{G}}_{j'\sigma n_{j\bar{\sigma}}|l\sigma}(\omega), \tag{B4}$$

with $\mathcal{G}_{j'\sigma n_{j\bar{\sigma}}|l\sigma}(t) = -\frac{i}{\hbar}\theta(t) < \{d_{j'\sigma}(t) n_{j\bar{\sigma}}(t), d^{\dagger}_{l\sigma}(0)\} >_{\mathcal{H}}$. At this stage, we impose the mean-field approximation $\tilde{\mathcal{G}}_{j'\sigma n_{j\bar{\sigma}}|l\sigma}(\omega) \approx < n_{j\bar{\sigma}} > \tilde{\mathcal{G}}_{j'\sigma|l\sigma}(\omega)$, which allows us to close the set of equations for the system of GFs. This gives rise to Eqs.(4) and (11), wherein

$$\Sigma^{\xi}_0(\omega) = \int_{-D}^{+D} \frac{d\varepsilon_k}{\hbar \tilde{v}_F} \frac{\mathcal{V}^2_k(\theta)}{(\omega^+ - \varepsilon_k - \xi V)} \tag{B5}$$

determines the self-energy in Eq.(8), with $\pm D$ as the ultraviolet $(+)$ and infrared energy-cutoffs $(-)$, respectively.

Appendix C: The molecular correlation function

As previously stated in the main text, the correlation function $\delta\rho_{jl}(\omega)$ in $\sum_{jl}\delta\rho_{jl}(\omega) = -\frac{1}{\pi}\mathrm{Im}[\tilde{\mathcal{G}}^{\mathrm{corr}}(\omega)]$ $(j \neq l = 1, 2)$ requires the determination of the GF $\tilde{\mathcal{G}}^{\mathrm{corr}}(\omega)$, which is obtained from the time Fourier transform of $\mathcal{G}^{\mathrm{corr}}(t) = -\frac{i}{\hbar}\theta(t) < \{f_{0\sigma}(t), f^{\dagger}_{0\sigma}(0)\} >_{\mathcal{H}}$. Thus, the operator $f_{0\sigma}$ describes a host site from which the molecular binding can be established by connecting the atoms through the TBG system. Particularly, in the helical basis $f_{0\sigma} = \sum_{\xi} \int_{-\infty}^{+\infty} dk \frac{\sqrt{\Omega_\theta |k| \pi}}{2\pi} c_{\sigma\xi}(k)$ according to Eq.(A4) and

$$\sum_{jl} \delta\rho_{jl}(\omega) = \sum_{\xi\xi'\sigma} (\frac{\sqrt{\Omega_\theta \pi}}{2\pi})^2 \int_{-\infty}^{+\infty} \int_{-\infty}^{+\infty} dk dq \sqrt{|k|}\sqrt{|q|} \times (-\frac{1}{\pi}) \mathrm{Im}[\tilde{\mathcal{G}}_{c_{\sigma\xi}(k)|c_{\sigma\xi'}(q)}(\omega)] \tag{C1}$$

expressed by the last GF, which in time domain reads $\mathcal{G}_{c_{\sigma\xi}(k)|c_{\sigma\xi'}(q)}(t) = -\frac{i}{\hbar}\theta(t) < \{c_{\sigma\xi}(k,t), c^{\dagger}_{\sigma\xi'}(q,0)\} >_{\mathcal{H}}$. By applying the EOM to unknown GFs, we find

$$\tilde{\mathcal{G}}_{c_{\sigma\xi}(k)|c_{\sigma\xi'}(q)}(\omega) = \frac{\delta_{\xi\xi'}\delta(k-q)}{(\omega^+ - \varepsilon_k - \xi V)} + \sum_j \frac{v_0 \sqrt{\Omega_\theta |k| \pi}}{2\pi(\omega^+ - \varepsilon_k - \xi V)} \tilde{\mathcal{G}}_{j\sigma|c_{\sigma\xi'}(q)}(\omega), \tag{C2}$$

where $\mathcal{G}_{j\sigma|c_{\sigma\xi'}(q)}(t) = -\frac{i}{\hbar}\theta(t) < \{d_{j\sigma}(t), c^{\dagger}_{\sigma\xi'}(q,0)\} >_{\mathcal{H}}$ and

$$\tilde{\mathcal{G}}_{j\sigma|c_{\sigma\xi'}(q)}(\omega) = \sum_l \frac{v_0 \sqrt{\Omega_\theta |q| \pi}}{2\pi(\omega^+ - \varepsilon_q - \xi' V)} \tilde{\mathcal{G}}_{j\sigma|l\sigma}(\omega). \tag{C3}$$

Therefore, after substituting Eqs.(C2) and (C3) into Eq.(C1), we finally deduce the molecular correlation function given by Eq.(10), which should consider $j \neq l = 1, 2$.

[1] Y. Cao, V. Fatemi, S. Fang, K. Watanabe, T. Taniguchi, E. Kaxiras, and P. Jarillo-Herrero, Unconventional Superconductivity in Magic-Angle Graphene Superlattices, Nature (London) 556, 43 (2018).

[2] Y. Cao, V. Fatemi, A. Demir, S. Fang, S. L. Tomarken, J. Y. Luo, J. D. Sanchez-Yamagishi, K. Watanabe, T. Taniguchi, E. Kaxiras, R. C. Ashoori, and P. Jarillo-Herrero, Correlated Insulator Behaviour at Half-Filling in Magic-Angle Graphene Superlattices, Nature (London) 556, 80 (2018).

[3] M. Fidrysiak, M. Zegrodnik, and J. Spalek, Unconventional topological superconductivity and phase diagram for an effective two-orbital model as applied to twisted bilayer graphene, Phys. Rev. B 98, 085436 (2018).

[4] T. J. Peltonen, R. Ojajärvi, and T. T. Heikkilä, Mean-field theory for superconductivity in twisted bilayer graphene, Phys. Rev. B 98, 220504 (2018).

[5] X. Y. Xu, K. T. Law, and P. A. Lee, Kekulé valence bond order in an extended Hubbard model on the honeycomb lattice with possible applications to twisted bilayer graphene, Phys. Rev.B 98, 121406 (2018).

[6] C.-C. Liu, L.-D. Zhang, W.-Q. Chen, and F. Yang, Chiral Spin Density Wave and d+id Superconductivity in the Magic-Angle-Twisted Bilayer Graphene, Phys. Rev. Lett. 121, 217001 (2018).

[7] S. Ray and T. Das, Wannier pairs in superconducting twisted bilayer graphene and related systems, Phys. Rev. B 99, 134515 (2019).

[8] J. F. Dodaro, S. A. Kivelson, Y. Schattner, X.-Q. Sun, and C. Wang, Phases of a phenomenological model of

twisted bilayer graphene, Phys. Rev. B 98, 075154 (2018).
[9] B. Padhi, C. Setty, and P. W. Phillips, Doped Twisted Bilayer Graphene near Magic Angles: Proximity to Wigner Crystallization not Mott Insulation, Nano Lett. 2018 18 (10) 6175.
[10] H. Guo, X. Zhu, S. Feng, and R. T. Scalettar, Pairing Symmetry of Interacting Fermions on Twisted Bilayer Graphene Superlattice, Phys. Rev. B 97, 235453 (2018).
[11] B. Roy and V. Juricic, Unconventional superconductivity in nearly flat bands in twisted bilayer graphene, Phys. Rev. B 99, 121407 (2019).
[12] H. C. Po, L. Zou, A. Vishwanath, and T. Senthil, Origin of Mott Insulating Behavior and Superconductivity in Twisted Bilayer Graphene, Phys. Rev. X 8, 031089 (2018).
[13] N. F. Q. Yuan and L. Fu, A Model for Metal-Insulator Transition in Graphene Superlattices and Beyond, Phys. Rev. B 98, 045103 (2018).
[14] C. Xu and L. Balents, Topological Superconductivity in Twisted Multilayer Graphene, Phys. Rev. Lett. 121, 087001 (2018).
[15] A. Luican, G. Li, A. Reina, J. Kong, R. R. Nair, K. S. Novoselov, A. K. Geim, and E. Y. Andrei, Single-Layer Behavior and Its Breakdown in Twisted Graphene Layers, Phys. Rev. Lett. 106, 126802 (2011).
[16] D. L. Miller, K. D. Kubista, G. M. Rutter, M. Ruan, W. A. de Heer, P. N. First, and J. A. Stroscio, Structural Analysis of Multilayer Graphene via Atomic Moiré Interferometry, Phys. Rev. B 81, 125427 (2010).
[17] G. Li, A. Luican, J. M. B. Lopes dos Santos, A. H. C. Neto, A. Reina, J. Kong, and E. Y. Andrei, Observation of van Hove Singularities in Twisted Graphene Layers, Nat. Phys. 6, 109 (2010).
[18] P. Moon and M. Koshino, Optical Absorption in Twisted Bilayer Graphene, Phys. Rev. B 87, 205404 (2013).
[19] G. Trambly de Laissardiere, D. Mayou, and L. Magaud, Numerical Studies of Confined States in Rotated Bilayers of Graphene, Phys. Rev. B 86, 125413 (2012).
[20] P. Moon and M. Koshino, Energy Spectrum and Quantum Hall Effect in Twisted Bilayer Graphene, Phys. Rev. B 85, 195458 (2012).
[21] J. M. B. Lopes dos Santos, N. M. R. Peres, and A. H. Castro Neto, Continuum Model of the Twisted Graphene Bilayer, Phys. Rev. B 86, 155449 (2012).
[22] L. Xian, S. Barraza-Lopez, and M. Y. Chou, Effects of Electrostatic Fields and Charge Doping on the Linear Bands in Twisted Graphene Bilayers, Phys. Rev. B 84, 075425 (2011).
[23] M. Kindermann and P. N. First, Local Sublattice-Symmetry Breaking in Rotationally Faulted Multilayer Graphene, Phys. Rev. B 83, 045425 (2011).
[24] R. Bistritzer and A. H. MacDonald, Moiré Bands in Twisted Double-Layer Graphene, Proc. Natl. Acad. Sci. U.S.A. 108, 12233 (2011).
[25] E. S. Morell, J. D. Correa, P. Vargas, M. Pacheco, and Z. Barticevic, Flat Bands in Slightly Twisted Bilayer Graphene: Tight-Binding Calculations, Phys. Rev. B 82, 121407 (2010).
[26] G. Trambly de Laissardière, D. Mayou, and L. Magaud, Localization of Dirac Electrons in Rotated Graphene Bilayers, Nano Lett. 10, 804 (2010).
[27] E. J. Mele, Commensuration and Interlayer Coherence in Twisted Bilayer Graphene, Phys. Rev. B 81, 161405 (2010).
[28] A. V. Rozhkov, A. O. Sboychakov, A. L. Rakhmanov, and F. Nori, Electronic properties of graphene-based bilayer systems, Physics Reports, 648, 1-104 (2016).
[29] J. M. B. Lopes dos Santos, N. M. R. Peres, and A. H. Castro Neto, Graphene Bilayer with a Twist: Electronic Structure, Phys. Rev. Lett. 99, 256802 (2007).
[30] Võ Tiên Phong and E. J. Mele, Obstruction and Interference in Low Energy Models for Twisted Bilayer Graphene, Phys. Rev. Lett. 125, 176404 (2020).
[31] W. N. Mizobata, Y. Marques, M. Penha, J. E. Sanches, L. S. Ricco, M. de Souza, I. A. Shelykh, and A. C. Seridonio, Atomic frustrated impurity states in Weyl metals, Phys. Rev. B 102, 075120 (2020).
[32] Y.Marques, A.E. Obispo, L.S. Ricco, M. de Souza, I.A. Shelykh, and A.C. Seridonio, Antibonding Ground state of Adatom Molecules in Bulk Dirac Semimetals, Phys. Rev. B 96, 041112 (2017).
[33] Y. Marques, W. N. Mizobata, R. S. Oliveira, M. de Souza, M. S. Figueira, I. A. Shelykh, and A. C. Seridonio, Chiral magnetic chemical bonds in molecular states of impurities in Weyl semimetals, Scientific Reports 9, 8452 (2019).
[34] K. Flensberg, F. von Oppen, and A. Stern, Engineered platforms for topological superconductivity and Majorana zero modes, Nat. Rev. Mater. https://doi.org/10.1038/s41578-021-00336-6 (2021).
[35] B. Jäck, Y. Xie, and A. Yazdani, Detecting and distinguishing Majorana zero modes with the scanning tunnelling microscope, Nat. Rev. Phys. 3, 541 (2021).
[36] P. W. Anderson, Localized Magnetic States in Metals, Phys. Rev. 124, 41 (1961).
[37] Y. Wang, D. Wong, A. V. Shytov, V. W. Brar, S. Choi, Q. Wu, H.-Z. Tsai, W. Regan, A. Zettl, R. K. Kawakami, S. G. Louie, L. S. Levitov, and M. F. Crommie, Observing Atomic Collapse Resonances in Artificial Nuclei on Graphene, Science 340, 734 (2013).
[38] I. Brihuega, P. Mallet, H. González-Herrero, G. Trambly de Laissardière, M.M. Ugeda, L. Magaud, J.M. Gómez-Rodríguez, F. Ynduráin, J.-Y. Veuillen, Unraveling the intrinsic and robust nature of van Hove singularities in twisted bilayer graphene by scanning tunneling microscopy and theoretical analysis, Phys. Rev. Lett. 109, 196802 (2012).
[39] E. Cisternas, J. Correa, Theoretical reproduction of superstructures revealed by STM on bilayer graphene, Chem. Phys. 409, 74 (2012).
[40] J. Hubbard, Electron Correlations in Narrow Energy Bands, Proc. R. Soc. A 276, 238 (1963).
[41] A. C. Hewson, The Kondo problem to Heavy Fermions, Cambridge University Press, (1993).
[42] S. Zhang, D. Huang, L. Gu, Y. Wang, and S. Wu, Substrate dopant induced electronic inhomogeneity in epitaxial bilayer graphene, 2D Mater. 8, 035001 (2021).
[43] H. Lee, K. Paeng, and I. S. Kim, A review of doping modulation in graphene, Synthetic Metals 244, 36-47 (2018).
[44] H. Bruus and K. Flensberg, Many-Body Quantum Theory in Condensed Matter Physics, An Introduction, Oxford University Press, (2012).

A.2 Atomic frustrated impurity states in Weyl metals

Atomic frustrated impurity states in Weyl metals

W. N. Mizobata,[1] Y. Marques,[2] M. Penha,[1] J. E. Sanches,[1] L. S. Ricco,[1] M. de Souza,[3] I. A. Shelykh,[2,4] and A. C. Seridonio[1,3,*]

[1] *São Paulo State University (Unesp), School of Engineering, Department of Physics and Chemistry, 15385-000, Ilha Solteira-SP, Brazil*
[2] *Department of Physics, ITMO University, St. Petersburg 197101, Russia*
[3] *São Paulo State University (Unesp), IGCE, Department of Physics, 13506-970, Rio Claro-SP, Brazil*
[4] *Science Institute, University of Iceland, Dunhagi-3, IS-107, Reykjavik, Iceland*

We theoretically analyze the effect of the inversion symmetry breaking on the structure of the impurity molecular states in Weyl metals. We show that for the case of a highly noncentrosymmetric Weyl metallic host, the standard picture of the alternating bonding and antibonding orbitals breaks down, and a qualitatively different frustrated atomic state emerges. This is a consequence of the pseudogap closing and related delicate Fano interplay between intra- and inter-impurity scattering channels.

I. INTRODUCTION

Dirac-Weyl equation [1], which first appears in the context of the relativistic quantum field theory, where it describes massless fermions, such as neutrinos, recently found its application in the domain of condensed matter physics. The existence of Dirac-Weyl fermions, quasi-relativistic quasiparticles, was unambiguously demonstrated for the family of the gapless binary alloys, such as Na_3Bi, Cd_3As_2, TaAs, NbAs and TaP [2–12]. The pair of the Dirac cones, present in these materials, can be split into two Weyl nodes with opposite chirality, if certain symmetry (inversion or time-reversal) is broken [13]. As a result, a topological Weyl material with unusual characteristics, such as Fermi arcs, chiral anomaly and exotic Hall effects [13–19], emerges. The peculiar band structure of Weyl systems has dramatic impact on the electronic structure of impurities [20–27]. In particular, as it was recently shown by some of us, chiral magnetic chemical bounds for a pair of impurities can appear in Weyl semimetals with energy degenerate Weyl nodes shifted in **k** space with respect to each other [27].

In this communication, we consider the structure of impurity molecular states in Weyl metals, where two Weyl nodes are located at the same **k**, but are shifted in energy. We demonstrate that in the geometry corresponding to two Anderson-like impurities [28] shown in Fig. 1, bonding and antibonding molecular states evolve into an atomic frustrated state marked by two Hubbard bands [29], with increase of the energy splitting between the two Weyl nodes. In this regime, the closing of the host pseudogap occurs, which leads to the dominance of the destructive Fano interference [30, 31] in the intra-impurity scattering channel, which is opposite to what happens in the corresponding inter-impurity channel revealing resonant behavior. The reported crossover can be realized by application of external stress [13] and experimentally detected with use of the STM techniques.

* corresponding author: antonio.seridonio@unesp.br

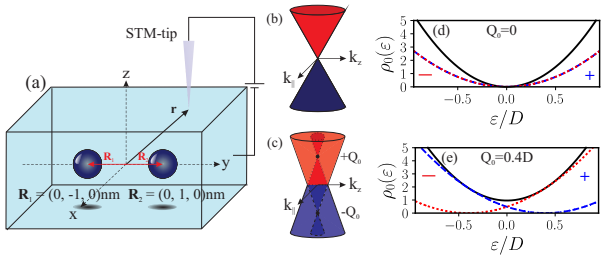

Figure 1. (Color online) Panel (a): Sketch of the considered system, consisting of a pair of impurities placed inside a Weyl metal close to its interface. The positions of the impurities are characterized by the vectors $\mathbf{R}_{1,2}$. The impurity molecular states can be probed on the surface of the host by an STM tip, whose location is characterized by the vector $\mathbf{r}$. Panel (b): Sketch of the dispersion, characteristic for a Dirac semimetal with two degenerated Dirac cones. The pseudogap is formed around the Dirac point, where the host Density of States (DOS) $\rho(\varepsilon) = 0$. Panel (c): Sketch of the dispersion, characteristic for the Weyl metal. The degeneracy of the Dirac cones is lifted due to the breaking of the inversion symmetry, and a pair of Weyl nodes vertically shifted with respect to each other appears. The pseudogap is closed due to the lifting of the degeneracy of the Weyl nodes. Panel (d): DOS $\rho(\varepsilon)$ of a Dirac semimetal. Panel (e): DOS $\rho(\varepsilon)$ of a Weyl metal. The plus and minus signs identify the DOS resolved in opposite chiralities.

II. THE MODEL

The Hamiltonian of the system sketched in Fig. 1 can be represented as:

$$\mathcal{H} = \sum_{\mathbf{k}} \psi^{\dagger}(\mathbf{k})(H_{+} \oplus H_{-})\psi(\mathbf{k}) + \varepsilon_d \sum_{j\sigma} d^{\dagger}_{j\sigma} d_{j\sigma} + U \sum_{j} d^{\dagger}_{j\uparrow} d_{j\uparrow} d^{\dagger}_{j\downarrow} d_{j\downarrow} + \sum_{j\mathbf{k}} \tilde{d}^{\dagger}_{j} \tilde{V}_{j\mathbf{k}} \psi(\mathbf{k}) + \text{H.c.}, \quad (1)$$

where $H_{\chi}(\mathbf{k}) = \chi(v_F \boldsymbol{\sigma} \cdot \mathbf{k} + \sigma_0 Q_0)$ is the Dirac-Weyl Hamiltonian of the host, corresponding to the two Dirac cones shifted vertically in energy (see Fig. 1(c)), $\boldsymbol{\sigma}$ stands

for the vector of Pauli matrices, σ_0 is the unity matrix, $\chi = \pm 1$ corresponds to the Weyl nodes chirality, Q_0 is the characteristic parameter defining the energy splitting between the Weyl nodes ($Q_0 \neq 0$ corresponds to a Weyl metal, $Q_0 = 0$ to a Dirac semimetal), v_F is the Fermi velocity, $\psi(\mathbf{k}) = (c_{\mathbf{k}+\uparrow}, c_{\mathbf{k}+\downarrow}, c_{\mathbf{k}-\uparrow}, c_{\mathbf{k}-\downarrow})^T$ is the four-spinor operator describing the electronic states in the host $c^\dagger_{\mathbf{k}\chi\sigma}, c_{\mathbf{k}\chi\sigma}$ with wave vector $\mathbf{k}$, chirality χ and spin σ. The operators $d^\dagger_{j\sigma}, d_{j\sigma}$ describe the electronic states of individual impurities ($j = 1, 2$) with single-particle energies ε_d and on-site Coulomb correlation energy U. The term, containing the two-spinor $\tilde{d}^\dagger_j = (d^\dagger_{j\uparrow}, d^\dagger_{j\downarrow})$, couples the impurities to the host, via the matrix

$$\tilde{V}_{j\mathbf{k}} = v_0 \begin{pmatrix} e^{i\mathbf{k}\cdot\mathbf{R}_j} & 0 & e^{i\mathbf{k}\cdot\mathbf{R}_j} & 0 \\ 0 & e^{i\mathbf{k}\cdot\mathbf{R}_j} & 0 & e^{i\mathbf{k}\cdot\mathbf{R}_j} \end{pmatrix}, \quad (2)$$

with v_0 being the coupling strength.

The electronic characteristics of the system are determined by its Local Density of States (LDOS) $\rho(\varepsilon, \mathbf{r})$, which can be found from the Green's functions (GF) of the host in the energy domain, $\tilde{\mathcal{G}}_{\chi\chi'\sigma}(\varepsilon, \mathbf{r})$ [32] defined as the time-Fourier transform of $\mathcal{G}_{\chi\chi'\sigma}(t, \mathbf{r}) = -i\theta(t)\left\langle\{\psi_{\chi\sigma}(t, \mathbf{r}), \psi^\dagger_{\chi'\sigma}(0, \mathbf{r})\}\right\rangle_{\mathcal{H}}$, with $\psi_{\chi\sigma}(t, \mathbf{r}) = \sum_{\mathbf{k}} e^{i\mathbf{k}\cdot\mathbf{r}} c_{\mathbf{k}\chi\sigma}(t)$ being the field operator of the host conduction states with spin σ and chirality χ. The LDOS reads [26, 27, 32]:

$$\rho(\varepsilon, \mathbf{r}) = -\frac{1}{\pi}\sum_{\sigma\chi\chi'} \mathrm{Im}\{\tilde{\mathcal{G}}_{\chi\chi'\sigma}(\varepsilon, \mathbf{r})\} = \rho_0 + \sum_{jj'} \delta\rho_{jj'}, \quad (3)$$

where the first term in this expression describes the host DOS $\rho_0 = \sum_\chi \frac{3\varepsilon^2_\chi}{D^3}$, with D as the energy cutoff and $\varepsilon_\chi = \varepsilon - \chi Q_0$, and the second term is the correction to the LDOS induced by the host-impurity coupling:

$$\delta\rho_{jj'}(\varepsilon, \mathbf{r}) = -\frac{1}{\pi v_0^2}\sum_{\chi\chi'\sigma} \mathrm{Im}[\Sigma^+_{\chi\sigma}(\mathbf{r} - \mathbf{R}_j)\tilde{\mathcal{G}}_{j\sigma|j'\sigma}(\varepsilon) \times \Sigma^-_{\chi'\sigma}(\mathbf{r} - \mathbf{R}_{j'})], \quad (4)$$

where $\mathbf{R}_j$ describes the coordinates of the two impurities. The terms with $j' = j$ and $j' \neq j$ correspond to intra- and inter-impurity scattering channels, respectively, and

$$\Sigma^\pm_{\chi\sigma}(\mathbf{r}) = -\frac{3\pi v_F v_0^2}{2D^3}\frac{e^{-i|\mathbf{r}|\frac{\varepsilon_\chi}{v_F}}}{|\mathbf{r}|}\left[\varepsilon_\chi \pm \chi\sigma\left(\varepsilon_\chi + i\frac{v_F}{|\mathbf{r}|}\right)\right] \quad (5)$$

are self-energy terms responsible for the spatial modulation of the LDOS. Following Ref.[25], to obtain Eq.(5), we have evaluated the noninteracting part of the GF $v_0^2\tilde{\mathcal{G}}_{\chi\chi'\sigma}(\varepsilon, \mathbf{r})$ (the corresponding one which solely considers the first term in Eq.(1)), by means of an expansion of the plane wave $e^{i\mathbf{k}\cdot\mathbf{r}}$ within $\tilde{\psi}_{\chi\sigma}(\varepsilon, \mathbf{r})$ (the Fourier transform of $\psi_{\chi\sigma}(t, \mathbf{r})$) into spherical harmonics terms, according to the Rayleigh equation, particularly for $D \gg \varepsilon$ [23, 25].

$\tilde{\mathcal{G}}_{j\sigma|j'\sigma}(\varepsilon)$ is the time-Fourier transform of the impurities GFs, $\mathcal{G}_{j\sigma|j'\sigma}(t) = -i\theta(t)\left\langle\{d_{j\sigma}(t), d^\dagger_{j'\sigma}(0)\}\right\rangle_{\mathcal{H}}$. Away from the Kondo regime [33], Hubbard-I approximation [26, 27, 29, 32] can be applied, which gives:

$$\tilde{\mathcal{G}}_{j\sigma|j\sigma}(\varepsilon) = \frac{\lambda^{\bar{\sigma}}_j}{g^{-1}_{j\sigma|j\sigma}(\varepsilon) - \lambda^{\bar{\sigma}}_j\Sigma^+_\sigma(\mathbf{R}_{12})g_{j'\sigma|j'\sigma}(\varepsilon)\lambda^{\bar{\sigma}}_{j'}\Sigma^-_\sigma(\mathbf{R}_{12})}. \quad (6)$$

Here $\bar{\sigma} = -\sigma$, $j' \neq j$, $\mathbf{R}_{12} = \mathbf{R}_1 - \mathbf{R}_2$, $\Sigma^\pm_\sigma(\mathbf{r}) = \sum_\chi \Sigma^\pm_{\chi\sigma}(\mathbf{r})$,

$$g_{j\sigma|j\sigma}(\varepsilon) = \frac{1}{\varepsilon - \varepsilon_{j\sigma} - \Sigma_0} \quad (7)$$

is the single-impurity noninteracting GF,

$$\Sigma_0 = \frac{3v_0^2}{2D^3}\sum_\chi \varepsilon^2_\chi\left(\ln\left|\frac{D + \varepsilon_\chi}{D - \varepsilon_\chi}\right| - \frac{2D}{\varepsilon_\chi} - i\right) \quad (8)$$

as the local self-energy,

$$\lambda^\sigma_j = 1 + \frac{U}{g^{-1}_{j\bar{\sigma}|j\bar{\sigma}}(\varepsilon) - U}\langle n_{j\sigma}\rangle \quad (9)$$

is the spectral weight and

$$\langle n_{j\sigma}\rangle = -\frac{1}{\pi}\int_{-\infty}^{+\infty} n_F(\varepsilon)\mathrm{Im}[\tilde{\mathcal{G}}_{j\sigma|j\sigma}(\varepsilon)]d\varepsilon \quad (10)$$

is the impurity occupation [34]. The crossed GF reads

$$\tilde{\mathcal{G}}_{j\sigma|j'\sigma}(\varepsilon) = g_{j\sigma|j\sigma}(\varepsilon)\lambda^{\bar{\sigma}}_j\Sigma^\pm_\sigma(\mathbf{R}_{jj'})\tilde{\mathcal{G}}_{j'\sigma|j'\sigma}(\varepsilon), \quad (11)$$

in which the $\pm$ signs correspond to $j = 1, j' = 2$ and $j = 2, j' = 1$, respectively. We emphasize that to close the set of Eqs. (6), (9) and (11) we have followed, as mentioned previously, the Hubbard-I scheme [26, 27, 29, 32]. It truncates the GFs of the Hamiltonian (Eq.(1)) by taking into account the Coulomb blockade regime [29, 32] and neglecting the Kondo correlations, where spin-flip processes dominate [33]. Thus, in applying the equation of motion procedure (EOM) to evaluate such GFs [32], those showing spin-flip scattering should be disregarded. By this manner, the impurity occupation $\langle n_{j\sigma}\rangle$ (Eq.(10)) is then determined off the Kondo limit [34], by performing a self-consistent calculation. The unique regime in which the equations above are exact is for $U = 0$.

In the case of uncorrelated impurities, realized when $|\mathbf{R}_{12}| \gg v_F v_0^2/D^3$, $\Sigma^\pm_\sigma(\mathbf{R}_{jj'}) = 0$ and $\delta\rho_{jj'} = 0$, Eq. (6) has two poles (the so-called Hubbard resonant bands [29]), appearing in $\delta\rho_{jj}$. The host-mediated inter-impurity correlations lead to the splitting of these poles, which corresponds to the formation of the impurity molecular bands even in the absence of the direct hopping term between the impurities [26].

III. RESULTS AND DISCUSSION

In our following consideration, we use model parameters: $|\mathbf{R}_{12}| = 2$ nm, $\varepsilon_d = -0.07D$, $v_0 = -0.14D$, $U = 0.14D$, $v_F \approx 3$ eVÅ and $D \approx 0.2$ eV [26, 27]. We suggest that the impurities are buried at the distance of 1 nm below the top surface of the Dirac-Weyl material, and are placed in the points $\mathbf{R}_1 = (0, -1, 0)$ nm and $\mathbf{R}_2 = (0, 1, 0)$ nm (see Fig. 1).

Fig. 2 illustrates the evolution of the spatial profiles of the LDOS at the surface of the host, given by Eq. (3), which can be probed by an STM tip, with increase of the parameter Q_0, describing the breaking of the inversion symmetry. In panel (a) the case of a Dirac semimetal with degenerated Weyl nodes, corresponding to $Q_0 = 0$, is illustrated. Molecular orbitals of the bonding and antibonding type are formed, and the profile corresponding to the latter one, with maxima of the LDOS centered at the points where the impurities are located, is shown. We stress that due to the peculiarities of the band structure of the Dirac host, the antibonding state has lower energy as compared to the bonding state, as it was demonstrated in Ref. [26]. The increase of the parameter Q_0 leads to the broadening of the LDOS peaks. Still, if values of Q_0 are moderate, the LDOS profiles remain qualitatively the same as for $Q_0 = 0$, and still can be described in terms of the formation of an antibonding molecular state, as it is illustrated in the panel (b). However, if the value of the parameter Q_0 becomes sufficiently large, the profile of the LDOS dramatically changes. It becomes depleted in the broad region around the impurities, and corresponds to a distorted centrosymmetric configuration characteristic to a frustrated atomic state, as it is shown in the panel (c).

To shed more light on the underlying mechanisms of its formation, we have analyzed separately different contributions to the LDOS induced by the impurities, as illustrated by Figs. 3 and 5.

Fig. 3 shows the plots of $\delta\rho_{jl}$ as a function of the energy for one particular tip position $\mathbf{r} = (1, 1, 1)$ nm (the change of this latter does not affect the results qualitatively). Both contributions from intra-impurity ($j = l$) and inter-impurity ($j \neq l$) are shown. In panel (a), corresponding to the case of a Dirac host with $Q_0 = 0$, one clearly sees the presence of the four peaks in $\delta\rho_{jj}$, corresponding to well resolved Hubbard bands and describing the formation of bonding and antibonding molecular orbitals, which stem from single-impurity bands centered around $\varepsilon_d < 0$ and $\varepsilon_d + U > 0$. For the considered parameters, the lowest energy peak corresponds to the antibonding state (pointed by the red arrow) and next peak to the bonding molecular state (pointed by the green arrow) [26]. The crossed term $\delta\rho_{jl}$, with $j \neq l$ exhibits two resolved pairs of peaks and Fano dips instead. The increase of the parameter Q_0 leads to the broadening of the peaks and Fano dips (panel (b), $Q_0 = 0.1D$). At some point, the peaks corresponding to the bonding and antibonding states merge, giving rise to intermediate Fano

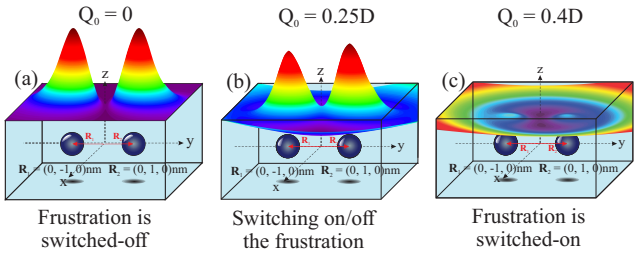

Figure 2. (Color online) Panel (a): Spatial profile of the LDOS, corresponding to the antibonding state of a pair of impurities, placed inside a Dirac semimetal ($Q_0 = 0$). Panel (b): Spatial profile of the LDOS for a pair of impurities, placed inside a Weyl metal with moderate value of $Q_0 = 0.25D$. Panel (c): Spatial profile of the LDOS, corresponding to the frustrated atomic state, for a pair of impurities, placed inside a Weyl metal with large value of $Q_0 = 0.4D$.

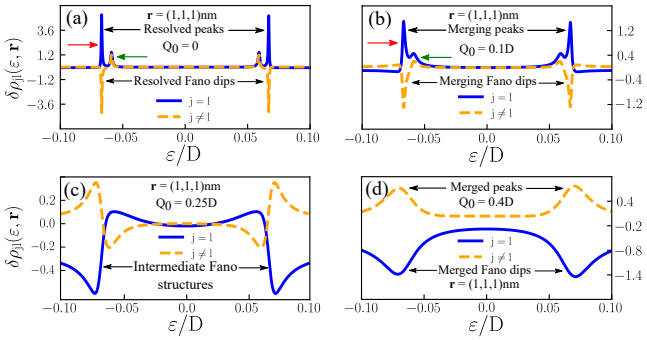

Figure 3. (Color online) Impurity-induced contributions to the density of states $\delta\rho_{jl}$ as a function of energy. Position of the STM tip is fixed at $\mathbf{r} = (1, 1, 1)$ nm. Panel (a): The case of a Dirac semimetal host, $Q_0 = 0$. One clearly sees two well resolved pairs of peaks in $\delta\rho_{jj}$, centered around ε_d and $\varepsilon_d + U$ and corresponding to bonding (indicated by green arrow) and antibonding (indicated by red arrow) molecular orbitals. Panel (b): The case of a Weyl metal host with small value of $Q_0 = 0.1D$. The peaks corresponding to the molecular states become broadened, but are still clearly resolved. Panel (c): The case of a Weyl metal host with moderate value of $Q_0 = 0.25D$. Intermediate Fano structures with merged peaks and dips appear. Panel (d): The case of a Weyl metal host with large value of $Q_0 = 0.4D$. Broad plateau in the density of states flanked by a pair of the merged peaks or dips is formed around $\varepsilon = 0$. Transition to the regime of atomic frustrated state occurs, as seen in Fig. 2(c).

lineshapes, with shallow minimum at $\varepsilon = 0$ (panel (c), $Q_0 = 0.25D$). Further increase of Q_0 leads to the formation of a broad plateau in the density of states around $\varepsilon = 0$, flanked by a pair of merged peaks for $j \neq l$, or merged dips for $j = l$ (panel (d), $Q_0 = 0.4D$). The presence of only two resolved Hubbard bands is typical for a pair of uncorrelated impurities. However, in our case the amplitudes $\delta\rho_{jl} \neq 0$ for $j \neq l$, which means that molecular binding still persists, although in the unusual

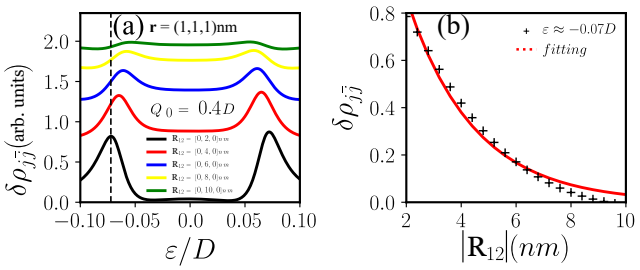

Figure 4. (Color online) Panel (a): Induced LDOS term $\delta\rho_{j\bar{j}}$ ($j = 1, \bar{j} = 2$ and $j = 2, \bar{j} = 1$) for $Q_0 = 0.4D$ with STM tip at $\mathbf{r} = (1, 1, 1)$ nm as a function of energy for several values of $\mathbf{R}_{12}$. For a sake of clarity, we present each case vertically shifted, thus making explicit that the increasing of $\mathbf{R}_{12}$ leads to the LDOS $\delta\rho_{j\bar{j}}$ vanishing. Hence, such a quenching reveals the crossover from the profile with two Hubbard bands, characteristic of the atomic frustrated state, towards that completely flat, for the uncorrelated pair of atoms situation. Panel (b): Amplitude of $\delta\rho_{j\bar{j}}$ evaluated at the black-dashed line cut $\varepsilon \approx -0.07D$ marked in panel (a) as a function of $|\mathbf{R}_{12}|$, which exhibits an exponential-like decay (crossed-points in black). Particularly, it is fitted by $\delta\rho_{j\bar{j}}(\varepsilon \approx -0.07D) = 1.96\exp(-0.41|\mathbf{R}_{12}|)$ (red line).

form of an atomic frustrated state. In this configuration, the role of the constructive and destructive Fano interference channels between $\delta\rho_{jj}$ and $\delta\rho_{jl}$ becomes inverted with respect to those observed in Dirac hosts, as it can be clearly seen from the comparison between panels (d) and (a).

We highlight that Figs. 2 and 3 introduce the concept of the atomic frustrated state, whose origin is genuinely of molecular-type, wherein its signatures resemble simultaneously those from uncorrelated and correlated atoms. Noteworthy, in such a scenario, the collective behavior of a diatomic molecule mimics an uncorrelated pair of atoms. Its characterization consists of electronic depletions (Fano dips) in $\delta\rho_{jj}$ around the Hubbard bands at $\varepsilon_d < 0$ and $\varepsilon_d + U > 0$, exactly as in the corresponding uncorrelated situation. Additionally and counterintuitively, a finite inter-impurities correlation ($\delta\rho_{jl} \neq 0$ with $j \neq l$) emerges as in a molecule, being identified by two Hubbard peaks instead. Hence, as this pair of atoms remains correlated through the host ($\delta\rho_{jl}$ finite, although with just two Hubbard structures), but shows itself seemingly uncorrelated ($\delta\rho_{jj}$ with two Hubbard structures, instead of four as in a molecule), then the state is considered atomically frustrated.

It is worth mentioning that as we focus on the paramagnetic case of impurities ($\langle n_{j\uparrow}\rangle = \langle n_{j\downarrow}\rangle$), the Dzyaloshinskii-Moriya interaction (DMI), which is a type of spin texture within the RKKY interaction [22, 23] for Dirac-Weyl semimetals, indeed does not rule this peculiar molecular binding here reported. The key responsible mechanism for the proposed state relies on the well-known Friedel-like oscillations [35], which according to some of us [26, 27], by working cooperatively with the intra-impurities Coulomb repulsion, is capable of establishing molecular bonds in Dirac-Weyl hosts. Thus, in the frustration regime of the Weyl metal phase, for first ever, novel Friedel-like behavior is revealed. It consists of electronic waves that travel forth and back between the left and right impurities ($\delta\rho_{jl}$), which are entirely phase shifted by π with respect to those scattered locally by the impurities ($\delta\rho_{jj}$). As a result, $\delta\rho_{jj}$ shows two structures dominantly Fano destructive at the two Hubbard bands $\varepsilon_d < 0$ and $\varepsilon_d + U > 0$ (Fig. 3(d)), which then flank a flat metallic-type plateau in the LDOS around the Fermi energy, as we will see later on.

In order to understand the long-range behavior of the frustrated atomic state encoded by $\delta\rho_{jl}$, in Fig.4(a) we analyze such a quantity for $Q_0 = 0.4D$ and STM-tip at $\mathbf{r} = (1, 1, 1)$ nm, as a function of energy upon varying $\mathbf{R}_{12}$. We can clearly perceive that the pair of Hubbard bands of the atomic frustrated state become broader as we increase the inter-impurities separation, in such a way that the $\delta\rho_{jl}$ approaches a profile entirely flat, which corresponds to the case of decoupled atoms. Thus by fixing the energy, for instance at $\varepsilon \approx -0.07D$ (black-dashed line cut), it is possible to estimate how quickly $\delta\rho_{jl}$ vanishes. Fig.4(b) then makes explicit that the decay obeys an exponential-like behavior (crossed-points in black), which is fitted by $\delta\rho_{j\bar{j}}(\varepsilon \approx -0.07D) = 1.96\exp(-0.41|\mathbf{R}_{12}|)$ (red line), where $j = 1, \bar{j} = 2$ and $j = 2, \bar{j} = 1$. Notice that for $|\mathbf{R}_{12}| = 10\,\text{nm}$, the molecular bond of the atomic frustrated state is practically dissociated.

Fig. 5(a) shows that the corresponding total LDOS has very broad maximum at $\varepsilon = 0$ and a pair of the broad minima around ε_d and $\varepsilon_d + U$. We clarify that the emergence of a flat LDOS (broad plateau) in the vicinity of $\varepsilon = 0$ (the Fermi energy) is characteristic of the metallic regime of the host. This is the direct outcome of the pseudogap closing in Weyl materials with large Q_0, for which the host DOS is enhanced at the Fermi energy. In equivalent words, it leads to the enhancement of states in the Fermi surface, exactly when the inversion symmetry is highly broken, which drives the system into the metallic Weyl regime. This comes from the increasing of the Dirac cones separation obeying blue and red shifts in the energy axis (see Fig.1(c) of the system sketch). This causes the formation of two bands. However, distinctly from the spin-orbit coupling, which resolves these bands in the spin channels, in Weyl metals such a separation occurs in the chirality degrees of freedom. The latter, we call particular attention, is defined as the spin projection over the linear momentum, contrasting the spin-orbit coupling, which instead, projects the former on the angular momentum. Thus, by integrating all momentum states split in energy, leads to two branches in the background DOS $\rho_0(\varepsilon)$, which are resolved in the chirality degree. Consequently, the branch with positive chirality shows blue-shift, while the negative presents the corresponding red (see also Fig.1(e)). Such a behavior closes the pseudogap at the Fermi energy, thus increasing the amount of the states in the Fermi surface. Therefore, this

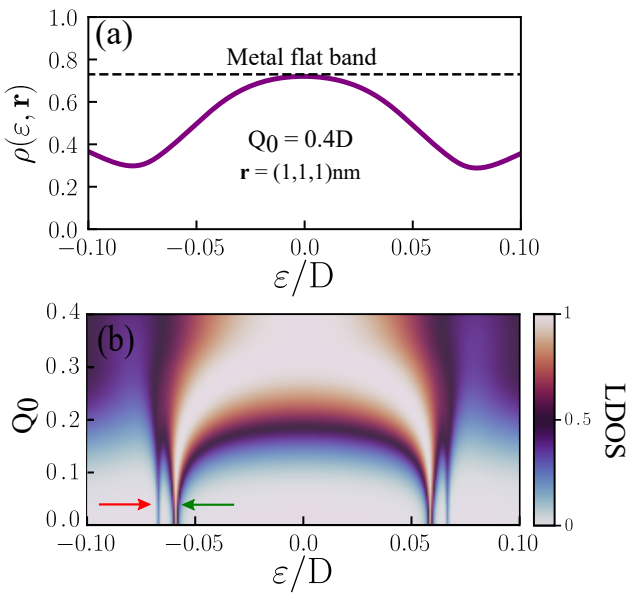

Figure 5. (Color online) Panel (a): The total LDOS of the system consisting of two impurities placed inside a Weyl metal host with $Q_0 = 0.4D$, corresponding to the regime of the formation of an atomic frustrated state. Position of the STM tip is fixed at $\mathbf{r} = (1, 1, 1)$ nm. Panel (b): Phase diagram, showing the total density of sates as function of the energy ε and the parameter Q_0. With increase of Q_0 one clearly observes the crossover from the regime of standard bonding (indicated by green arrow) and antibonding (indicated by red arrow) molecular orbitals, characterized by four well resolved Hubbard bands, to the regime of frustrated atomic state.

gives rise to the flat metallic-type plateau in the LDOS around $\varepsilon = 0$.

The crossover between the cases of the standard molecular bonding and antibonding states, and formation of an atomic frustrated state is illustrated by Fig. 5(b), where a phase diagram, showing the total LDOS as function of the energy ε and the parameter Q_0 is presented. With increase of Q_0 the narrow peaks characteristic to four well resolved Hubbard bands become broadened and finally merge, producing characteristic profile plotted in Fig. 5(a). From the experimental perspective, such transition can be achieved by application of stress, which is expected to break the inversion symmetry [13].

IV. CONCLUSIONS

We have demonstrated that the nature of electronic states of a pair of impurities placed inside a Weyl metal strongly depends on the parameter Q_0, which defines the breaking of the inversion symmetry in the host material. For small values of this parameter one observes the formation of conventional bonding and antibonding molecular orbitals. However, for large values of Q_0 transition to an atomic frustrated state, characterized by a broad bowl-shape distribution of the LDOS in the real space occurs. This transition should take place under the application of external stress, which allows to propose the concept of a molecular switcher, alternating between ordinary molecular and atomic frustrated states.

V. ACKNOWLEDGMENTS

We thank the Brazilian funding agencies CNPq (Grants. 305668/2018-8 and 302498/2017-6), the São Paulo Research Foundation (FAPESP; Grant No. 2018/09413-0) and Coordenação de Aperfeiçoamento de Pessoal de Nível Superior - Brasil (CAPES) – Finance Code 001. YM and IAS acknowledge support the Ministry of Science and Higher Education of Russian Federation, goszadanie no. 2019-1246, and ITMO 5-100 Program.

[1] H. Weyl, Zeitschrift für Physik 56, 330 (1929).
[2] Z. Wang, Y. Sun, X.-Q. Chen, C. Franchini, G. Xu, H. Weng, X. Dai, and Z. Fang, Phys. Rev. B 85, 195320 (2012).
[3] Z. K. Liu, B. Zhou, Y. Zhang, Z. J. Wang, H. M. Weng, D. Prabhakaran, S.-K. Mo, Z. X. Shen, Z. Fang, X. Dai *et al.*, Science 343, 864 (2014).
[4] Z. Wang, H. Weng, Q. Wu, X. Dai, and Z. Fang, Phys. Rev. B 88, 125427 (2013).
[5] Z. K. Liu, J. Jiang, B. Zhou, Z. J. Wang, Y. Zhang, H. M. Weng, D. Prabhakaran, S-K. Mo, H. Peng, P. Dudin *et al.*, Nature Materials 13, 677 EP– (2014).
[6] S.-M. Huang, S.-Y. Xu, I. Belopolski, C.-C. Lee, G. Chang, B. Wang, N. Alidoust, G. Bian, M. Neupane, C. Zhang *et al.*, Nature Communications 6, 7373 EP– (2015).
[7] H. Weng, C. Fang, Z. Fang, B. A. Bernevig, and X. Dai, Phys. Rev. X 5, 011029 (2015).
[8] S.-Y. Xu, I. Belopolski, N. Alidoust, M. Neupane, G. Bian, C. Zhang, R. Sankar, G. Chang, Z. Yuan, C.-C. Lee *et al.*, Science 349, 613 (2015).
[9] B. Q. Lv, H. M. Weng, B. B. Fu, X. P. Wang, H. Miao, J. Ma, P. Richard, X. C. Huang, L. X. Zhao, G. F. Chen *et al.*, Phys. Rev. X 5, 031013 (2015).
[10] B. Q. Lv, N. Xu, H. M. Weng, J. Z. Ma, P. Richard, X. C. Huang, L. X. Zhao, G. F. Chen, C. E. Matt, F. Bisti *et al.*, Nature Physics 11, 724 EP– (2015).
[11] S.-Y. Xu, C. Liu, S. K. Kushwaha, R. Sankar, J. W. Krizan, I. Belopolski, M. Neupane, G. Bian, N. Alidoust, T.-R. Chang *et al.*, Science 347, 294 (2015).
[12] N. Xu, H. M. Weng, B. Q. Lv, C. E. Matt, J. Park, F. Bisti, V. N. Strocov, D. Gawryluk, E. Pomjakushina, K. Conder *et al.*, Nature Communications 7, 11006 EP– (2016).
[13] N. P. Armitage, E. J. Mele, and A. Vishwanath, Rev. Mod. Phys. 90, 015001 (2018).

[14] X. Wan, A. M. Turner, A. Vishwanath, and S. Y. Savrasov, Phys. Rev. B 83, 205101 (2011).
[15] K.-Y. Yang, Y.-M. Lu, and Y. Ran, Phys. Rev. B 84, 075129 (2011).
[16] P. Hosur, S. A. Parameswaran, and A. Vishwanath, Phys. Rev. Lett. 108, 046602 (2012).
[17] P. Kim, J. H. Ryoo, and C.-H. Park, Phys. Rev. Lett. 119, 266401 (2017).
[18] H. Nielsen, and M. Ninomiya, Physics Letters B 130, 389–396 (1983).
[19] G. Xu, , H. Weng, Z. Wang, X. Dai, and Z. Fang, Phys. Rev. Lett. 107, 186806 (2011).
[20] J.-H. Sun, D.-H. Xu, F.-C. Zhang, and Y. Zhou, Phys. Rev. B 92, 195124 (2015).
[21] D. Ma, H. Chen, H. Liu, and X. C. Xie, Phys. Rev. B 97, 045148 (2018).
[22] H.-R. Chang, J. Zhou, S.-X. Wang, W.-Y. Shan, and D. Xiao, Phys. Rev. B 92, 241103 (2015).
[23] M. V. Hosseini and M. Askari Phys. Rev. B 92, 224435 (2015).
[24] A. Principi, G. Vignale, and E. Rossi, Phys. Rev. B 92, 041107 (2015).
[25] S.-H. Zheng, , R.-Q. Wang, M. Zhong, and H.-J. Duan, Scientific Reports 6, 36106 (2016).
[26] Y. Marques, A. E. Obispo, L. S. Ricco, M. de Souza, I. A. Shelykh, and A. C. Seridonio, Phys. Rev. B 96, 041112 (2017).
[27] Y. Marques, W. N. Mizobata, R. S. Oliveira, M. de Souza, M. S. Figueira, I. A. Shelykh, and A. C. Seridonio, Scientific Reports 9, 8452 (2019).
[28] P. W. Anderson, Phys. Rev. 124, 41 (1961).
[29] J. Hubbard, Proc. R. Soc. A 276, 238 (1963).
[30] U. Fano, Phys. Rev. 124, 1866 (1961).
[31] A. E. Miroshnichenko, S. Flach, and Y. S. Kivshar, Rev. Mod. Phys. 82, 2257 (2010).
[32] H. Bruus and K. Flensberg, Many-Body Quantum Theory in Condensed Matter Physics, An Introduction, Oxford University Press, 2012.
[33] A. C. Hewson, The Kondo problem to Heavy Fermions, Cambridge University Press, 1993.
[34] The Hubbard I is applicable for temperatures $T \gg T_K$, being T_K the Kondo temperature. For the evaluation of $\langle n_{j\bar{\sigma}} \rangle$, T should not be very high so that we can safely assume the Heaviside step function for the Fermi-Dirac distribution $n_{_F}(\varepsilon)$.
[35] J. Friedel, Il Nuovo Cimento, 7, 287 (1958).